

MODELLING POWDER COMPACTION AND BREAKAGE OF COMPACTS

Thesis submitted for the degree of
Doctor of Philosophy
at the University of Leicester

by

Chenglong Shang

Department of Engineering,
University of Leicester

2012

Dedications

To my dear parents, Zuke Shang and Guihua Yang

and

To my dear wife, Minhha Nguyen

Abstract

Modelling powder compaction and breakage of compacts

Chenglong Shang, Ph.D.

Experimental and numerical simulation studies were carried out to enhance the understanding of the compaction behaviour of powder materials and to study the breakage behaviour of tablets after compaction.

In order to simulate powder compaction and post compaction behaviour an appropriate constitutive model is required. To calibrate the constitutive model (e.g. a Drucker-Prager Cap model) a series of experiments were carried out including closed die compaction, uniaxial and diametrical compression tests. A newly developed apparatus consisting of a die instrumented with radial stress sensors was used to determine constitutive parameters as well as friction properties between the powder and die wall.

The calibration of constitutive models requires accurate stress-strain curves. During die compaction the deformation of the powder material is determined by considering the elastic deformation (or compliance) of the system. The effect of different compliance correction methods was evaluated with regards to the accuracy of models predicting the pressing forces. A method for accounting for non-homogeneous stress states in instrumented die compaction was also developed. A complete data extraction procedure was presented.

The breakage behaviour of flat and curved faced tablets was investigated and the breakage patterns of tablets were examined by X-Ray computed tomography. An empirical equation that relates the material strength to the break force was proposed. The constitutive model was implemented into the finite element package Abaqus/Standard to simulate powder compaction and breakage. A range of failure criteria have been evaluated for predicting break force of flat and curved faced tablets under diametrical compression.

Acknowledgement

The work presented in this thesis has been carried out at the Mechanics of Materials group, Department of Engineering at the University of Leicester.

First, I would like to express my deepest gratitude to my supervisor, Dr. Csaba Sinka. I really appreciate his understanding, encouragement and favors on every possible manner. I am also deeply impressed by his wide knowledge and inspiration. This work will not have been possible without his continuous guidance and support.

I would like to thank Professor Jingze Pan for his support and persistence that make me believe in myself and complete this degree. I would also like to thank Dr. Simon Gill for his invaluable advice on writing my thesis. I am grateful for Dr. Simon Laws, Simon Millward, Barry Kirkland, Ian Bromley who contribute to my lab work. Special thanks go to Lifeng Ding, Xiaoxiao Han, Fan Li who gave me help in all aspects of my daily life. I would like thank all the faculties and staff for all the supporting which make my study at the University of Leicester a great experience.

Finally, I would like to thank the University of Leicester for a partial PhD studentship as a support of this work.

Table of Contents

List of Tables	v
List of Figures	vi
List of Symbols	xii
Chapter 1. Introduction	1
1.1 Powder compaction in industry	1
1.1.1 Powder metallurgy (PM)	3
1.1.2 Ceramics industry	5
1.1.3 Pharmaceutical industry.....	6
1.2 Compaction methods.....	8
1.3 Compaction mechanisms	10
1.4 Current trends in modelling powder compaction and compact strength ...	11
1.5 Research objectives	13
1.6 Thesis structure	13
Chapter 2. Constitutive laws for powder compaction	16
2.1 Material constitutive laws	16
2.2 Modelling approaches for powder compaction	16
2.2.1 Continuum approach	17
2.2.1.1 Gurson model	19
2.2.1.2 Cam-Clay model.....	20
2.2.1.3 The micromechanical model of Fleck.....	23
2.3 Strength of green powder compact.....	25
Chapter 3. Finite element analysis of powder compaction	27
3.1 The finite element method.....	27
3.2 Finite element method for non-linear material and large deformation	30
3.2.1 Finite element discretisation	30

Table of Contents

3.3	Applications of finite element method in powder engineering	33
3.3.1	Example 1: The density distribution in curved faced tablets.....	34
3.3.2	Example 2: Defects of powder compacts.....	36
3.4	Summary.....	38
Chapter 4.	Characterization methods for compaction and breakage.....	39
4.1	Materials.....	39
4.1.1	Distaloy AE.....	39
4.1.2	Dibasic calcium phosphate.....	40
4.1.3	Microcrystalline cellulose	41
4.2	Specimen manufacturing.....	42
4.3	Drucker-Prager Cap plasticity model	45
4.4	Parameter characterisation of the DPC Model	49
4.4.1	Characterization of the shear failure line	50
4.4.2	Characterization of the cap surface	51
4.4.3	Characterization of elastic properties	53
4.5	Strength measurement.....	56
4.6	Summary.....	59
Chapter 5.	Instrumented die system	61
5.1	Closed die system.....	61
5.2	Instrumented die system.....	63
5.3	Experimental results using the instrumented die.....	66
5.4	Summary	69
Chapter 6.	Instrumented die data extraction method and model calibration	70
6.1	Introduction	70
6.2	Elastic compliance of the testing frame	73
6.3	Non-homogeneous stress state	76

Table of Contents

6.4	Compliance corrections for loading and calibration of model parameters	78
6.5	Compliance corrections for unloading and calibration of elastic parameters	83
6.6	Friction coefficient	90
6.7	Conclusions	92
Chapter 7.	Modelling powder compaction	94
7.1	Validation of constitutive model and compliance correction method	96
7.2	Practical considerations for modelling powder compaction	101
7.2.1	Constitutive data for powder compaction	101
7.2.2	Density distribution in powder compacts	103
7.2.3	Force-displacement response	105
7.3	Conclusions	107
Chapter 8.	Experimental study of tablet breakage.....	109
8.1	Introduction	109
8.2	Curved shaped tablet	112
8.3	Results and discussion	114
8.4	Conclusions	127
Chapter 9.	Numerical analysis of tablet breakage.....	128
9.1	Introduction	128
9.1.1	Stress distribution of diametrical compression test	128
9.1.2	X-ray CT characterisation of tablet structure	132
9.2	Numerical procedure	132
9.2.1	Constitutive model	134
9.2.2	Failure criteria	137
9.3	Results and discussion	138
9.3.1	Flat faced tablet	138

Table of Contents

9.3.2	Curved faced tablet	143
9.3.3	Failure mode	150
9.4	Conclusions	155
Chapter 10.	Conclusions and future work	157
10.1	Conclusions	157
10.2	Recommendations for Future work.....	159
References	161
Appendices	175
Publications	175
Appendix A	176
Appendix B	178

List of Tables

Table 4-1 Calibration of constitutive model parameters	50
Table 4-2 Characteristics of tablets used for diametrical compression tests	57
Table 4-3 Characteristics of tablets used for uniaxial compression tests	58
Table 7-1 Simplified DPC model parameters for A-Tab	102
Table 8-1 Tablet shapes (tablet radius R illustrated in Figure 8-1).....	112
Table 8-2 Experimental design for curved faced tablets. Tick indicates tablet manufactured, Cross indicates that the tablet was not manufactured because the band thickness (W) became too small.....	113
Table 8-3 Coefficients for equation (8-2) for curved faced tablets	117
Table 9-1 Geometry and initial density for simulations	134
Table 9-2. Coefficients using equation (8-6) for experimental data and 3 failure criteria	146

List of Figures

Figure 1-1 Manufacturing process for powder components (from Schneider, 2003)	1
Figure 1-2 The concept flow for powder metallurgy from powder processing to final product (from Randall, 1997)	4
Figure 1-3 PM parts (gear components) made by powder (from Sinotech limited, UK)	4
Figure 1-4 Ceramic components (from Ceramic Substrates and Components Ltd, UK)	6
Figure 1-5 Pharmaceutical tablets (from Wickham Laboratories Ltd, UK)	7
Figure 1-6 Different configuration of closed die system a)Single-action compaction system b)Double-action compaction system c) Floating die system (from Wu, 2005a).....	10
Figure 1-7 Sequence of micro-processes and deformation mechanism during press agglomeration (from Stasiak et al., 2010).....	11
Figure 2-1 Schematic representation of the load paths corresponding to the different test procedures (from Wood, 1990).....	19
Figure 2-2 Yield surfaces for microcrystalline cellulose using various models calibrated on a closed-die compaction experiment: C-C Cam-Clay, D-P Drucker-Prager cap, P-P porous plasticity. The closed-die compaction trajectory is indicated with a dotted line (from Sinka, 2007).	21
Figure 2-3 Fleck’s predicted yield surface is given for both isostatic compaction and close die compaction. Contacts are frictionless and two limits cohesion: full cohesion ($\eta = 1$) and cohesionless ($\eta = 0$) are presented (from Fleck, 1995).....	23
Figure 3-1 Configuration of a deformed material body	28
Figure 3-2 Relative density distribution in curved faced tablets. Experimental data for tablet compressed using a) clean and b) lubricated tooling. Numerical results for c) high and d) low friction coefficient (from Sinka et al., 2003)	35

Figure 3-3 The failure mode of pharmaceutical tablets during diametrical compression test a) unlubricated friction condition, b) lubricated friction condition and c) break force in diametrical compression experiments (from Sinka et al., 2004)	36
Figure 3-4 Crack development in pharmaceutical tablets a) X-ray CT image of crack pattern b) Numerical simulation of shear stress distribution (from Wu et al., 2005)	37
Figure 3-5 Crack development in multilevel parts made of metallic powder (from Coube and Riedel, 2000)	38
Figure 4-1 SEM image of Distaloy AE (From Sinka and Cocks, 2007)	40
Figure 4-2 SEM image of A-Tab powder (from Galen, 2005)	41
Figure 4-3 SEM image of MCC grade Avicel PH102 (from Sinka et al., 2003)	42
Figure 4-4 Closed die system for thin disks production a) Die and punches and b) system set-up	43
Figure 4-5 Closed die system for tall cylinder samples production a) Die and punches and b) system set-up	44
Figure 4-6 Typical force verse displacement curve during loading and unloading	45
Figure 4-7 a) stress state experienced by a cylindrical powder aggregate, b) Drucker-Prager cap model and experimental procedures for determining the shear failure line F_s using (1) uniaxial tension, (2) simple shear, (3) diametrical compression, (4) uniaxial compression; and the compaction surface F_c using (5) triaxial testing: 5A consolidated triaxial test, 5B simulated closed-die compaction, 5C radial loading in stress space, 5D isostatic test; (6) instrumented die compaction.	48
Figure 4-8 A method to determine elastic properties form unloading slope a) axial stress-axial strain curve and b) axial stress-radial stress curve	55
Figure 4-9 Images of a) Diametrical compression test and b) Uniaxial compression test	56
Figure 4-10 Tensile and compressive strength as functions of relative density	58
Figure 4-11 Shear failure line parameters, a) cohesion, b) internal friction angle	59
Figure 5-1 Average relative density as a function of the maximum compaction pressure for Distaloy AE powder using three dies with different diameters.	62

Figure 5-2 Closed die compaction a) stress states, b) die instrumented with radial stress sensors	64
Figure 5-3 Instrumented die set-up (from Shang et al., 2011)	65
Figure 5-4 Stress displacement curve during die compaction.....	67
Figure 5-5 Axial stress at top and bottom punch during unloading stage a) the transition phase when axial stress at top equals to axial stress at bottom. b) the residual axial stress of top and bottom punch after unloading	68
Figure 6-1 Compliance curve of the instrumented die system.....	75
Figure 6-2 Force-displacement behaviour of the powder material together with corrections using linear and non-linear system compliance, a) full curves, b) details of unloading	75
Figure 6-3 Axial stress distribution along the height of the compact determined using the Janssen-Walker method of differential slices	77
Figure 6-4 Hardening laws obtained from raw data (labelled 3) and corrections using linear (2) and non-linear (1) system compliance.....	78
Figure 6-5 Stress-strain curves, 1 average axial stress-axial strain, 2 axial stress at top sensor vs. axial strain at top sensor, 3 axial stress at bottom sensor vs. axial strain at bottom sensor, 4 radial stress at top sensor vs. axial strain at top sensor, 5 radial stress at bottom sensor vs. axial strain at bottom sensor, 6 average radial stress vs. average axial strain.....	80
Figure 6-6 Parameters of the cap surface a) cap shape parameter as a function of relative density and b) hardening law.....	81
Figure 6-7 Drucker-Prager cap surfaces, the labels indicating relative density	82
Figure 6-8 Axial stress- relative density curves during loading and unloading from various relative densities	82
Figure 6-9 Stress-strain data during unloading in a die using experimental data and various correction methods.....	84
Figure 6-10 Elements contributing to total compliance of the system, a) basic system, b) finite element analysis of top punch compliance	85
Figure 6-11 a) Axial stress/axial strain, b) Axial stress/Radial stress curve during loading and unloading, the labels indicating relative density of specimens	86

Figure 6-12 a) Young's modulus E , b) Poisson's ratio ν as a function of density using unloading curve method	88
Figure 6-13 Effective stress against hydrostatic stress curve during loading and unloading for Distaloy AE powder	90
Figure 6-14 Variation of the friction coefficient with radial contact pressure	91
Figure 7-1 Finite element meshes a) before compaction and b) at the end of compaction	95
Figure 7-2 Stress-strain data obtained from force-displacement data and different correction methods for system compliance, 1-axial stress for non-linear correction, 2-axial stress for linear correction, 3-axial stress for uncorrected data, 4-radial stress for non-linear correction, 5-radial stress for linear correction, 6 radial stress for uncorrected strain data. Primes (') indicate the corresponding numerical analysis result, which overlap the experimental data	97
Figure 7-3 Effect of friction on force-displacement response, a) full curve, b) detail. Labels: 0 frictionless, 1 $\mu=0.1$, 2 experimental data, 3 $\mu=0.2$, 4 $\mu=0.3$, 5 $\mu=0.5$ corresponding to the top punch force. Primes (') are used to label data corresponding to the bottom punch force.	98
Figure 7-4 Slope of unloading line from experimental data and different compliance correction methods together with the corresponding numerical modelling results	100
Figure 7-5 a) Yield surfaces for Drucker-Prager cap models. The labels indicate relative density (defined as 1-zero porosity), the dashed line indicates the loading path of closed die compaction, b) Hardening rules for Drucker-Prager cap models	102
Figure 7-6 Verification of the models; a) comparison of experimental stress-strain curves with model prediction for frictionless compaction	103
Figure 7-7 Relative density distributions in vertical cross sections of cylindrical compacts with values of the coefficient of friction between powder and die wall of a) 0.1, b) 0.2 and c) 0.3.....	104
Figure 7-8 Effect of Young's modulus on stress-strain response for Drucker-Prager cap model.....	105
Figure 7-9 Density distribution in a curved faced tablet.....	107

Figure 8-1 Geometry and diagram of diametrical compression test of curved faced tablets (a) side view (b) top view.....	110
Figure 8-2 Experimental space for curved faced tablet geometry	115
Figure 8-3 Tensile strength – relative density behaviour.....	116
Figure 8-4 Normalised break force calculated using equations ((8-1),(8-2) and (8-6))	119
Figure 8-5 Comparison between empirical equations and experimental data : a) Shallow, b) Standard, c) Deep, d) Extra deep concave, e) labelled ‘a’, f) labelled ‘b’. Label 1, 2 and 3 indicates, Pitt’s equation, 2 parameter model and 4 parameter model, respectively	121
Figure 8-6 Tablets fail due to complex failure mechanism. Red solid marker indicates that the tablets totally laminate. Blue solid marker indicates that tablets fails in a way both delimitation and breaking into halves may be observed. Photos (b)-(e), tablets were compacted under maximum pressure: 250, 150, 50 and 25 MPa using powder weight: 400, 400, 450 and 400 mg.	124
Figure 8-7 Normalized break force surface using two-parameter model fit experimental data in limited region ($0.1 < t/D < 0.45$, $0.1 < W/D < 0.35$).	126
Figure 9-1 The diametrical compression test (a) Point loading condition, (b) Hondros distributed loading condition	129
Figure 9-2 Finite element mesh during diametrical compression test simulation a) flat faced and b) curved faced tablets.....	133
Figure 9-3 Elastic properties as function of relative density, a) Young’s modulus, b) Poisson’s ratio	135
Figure 9-4 Drucker-Prager cap surfaces, the labels indicating relative density ...	136
Figure 9-5 Diametrical compression test simulation of flat faced tablet using 3 failure criteria: (a) criterion 1, (b) criterion 2, (c) criterion 3	139
Figure 9-6 Force displacement curve of 3 failure criteria at RD=0.84 of flat faced tablet	140
Figure 9-7 Tensile strength of experimental data and prediction of 3 failure criteria	141
Figure 9-8 a) density at contact point, b) photo.....	142

Figure 9-9 Simulation and experimental data144

Figure 9-10 Normalised force displacement curve of 3 failure criteria at RD=0.84 for curved faced tablet with a geometry ($W=1.575\text{mm}$, $t=2.91\text{mm}$)145

Figure 9-11 Surface fitted to simulation data points using 3 failure criteria (a) Criterion 1, (b) Criterion 2, (c) Criterion 3146

Figure 9-12 Normalized force surfaces in 3D verse the geometry factor t/D , W/D 148

Figure 9-13 Comparison between empirical equations and failure criteria: a) Shallow(labelled 'a'), b) Standard (labelled 'b'), c) Deep (labelled 'c'), d) Extra deep concave (labelled 'd'), e) labelled 'e', f) labelled 'f'149

Figure 9-14 Photos of tablet breakage a) Compaction pressure: 150MPa, Mass: 400mg, geometry: $t/D= 0.464$, $W/D=0.198$ and $D=10.347\text{mm}$ b) Compaction pressure: 75MPa, Mass: 400mg, geometry: $t/D= 0.552$, $W/D=0.151$ and $D=10.387\text{mm}$152

Figure 9-15 Maximum principal stress analysis of $t/D=0.451$, $W/D=0.1$ at RD=0.84 using DPC model152

Figure 9-16 X-ray computed tomographic images of shallow shaped tablet ($t/D=0.3$, $W/D=0.1$, $D=10.322\text{mm}$) at different locations: a) X-Z plane; b) X-Y plane; c) Y-Z plane; d) offset plane (0.69mm from XY)153

Figure 9-17 a) Photos of breakage of ball shaped tablet and X-ray computed tomographic images of ball shaped tablet ($t/D=0.721$, $W/D=0.0538$, $D=10.344\text{mm}$) at different locations: a) X-Z plane; b) X-Y plane; c) Y-Z plane154

List of Symbols

ρ	the hydrostatic pressure
q	Mises equivalent stress
$\sigma_{ij}(i,j=1,2,3)$	the components of stress
Ω	domain of a material body
Γ	surface of a material body
\boldsymbol{x}	position vector of any spatial coordinate system
\boldsymbol{v}	velocity vector
\boldsymbol{u}	displacement vector
$\tilde{\boldsymbol{f}}$	total force applied on a material
ρ	density of material
\boldsymbol{b}	body force acceleration
$\boldsymbol{\tau}$	surface traction
$\tilde{\boldsymbol{p}}(t)$	linear momentum of the material body
$\boldsymbol{\sigma}$	the Cauchy stress tensor
\boldsymbol{n}	unit surface normal vector
$\boldsymbol{\varepsilon}$	strain tensor
\boldsymbol{M}	mass matrix

List of Symbols

\mathbf{f}_u	load vector
$\bar{\mathbf{B}}$	strain matrix
\mathbf{B}_L	linear infinitesimal strain-displacement matrix
\mathbf{B}_{NL}	nonlinear strain-displacement matrix
Ψ	nonlinear function of nodal displacement
\mathbf{D}_T	consistent tangential stiffness matrix
\mathbf{K}_L	small displacement stiffness matrix
\mathbf{K}_{NL}	large displacement matrix
\mathbf{K}_σ	symmetric matrix dependent on the stress level
$\bar{\mathbf{K}}_T$	total tangential stiffness matrix
$\dot{\varepsilon}_{ij}^p$	plastic strain rate
G	flow potential
$\dot{\lambda}$	plastic multiplier
F_S	shear failure surface
F_C	cap surface
d	cohesion
β	friction angle
σ_{ax}	axial stress

List of Symbols

σ_{rad}	radial stress
RD	relative density
ρ_{full}	full density of material
R	cap shape parameter
p_b	hydrostatic compression yield stress
E	Young's modulus
ν	Poisson's ratio
σ_d	tensile strength
F_d	break force from diametrical compression test
F_u	break force from uniaxial compression test
D	specimen diameter
t	specimen thickness
σ_c	compressive strength
ε_v^p	volumetric plastic strain
K	bulk modulus
G	shear modulus
I_1	first stress invariant
δ_{ij}	the Kronecker delta

List of Symbols

ε_{ax}	axial strain
d_T	displacement of top punch
F_T	force at top punch
F_B	force at bottom punch
σ_{r_T}	radial stress at top sensor
σ_{r_B}	radial stress at bottom sensor
σ_T	axial stress at top punch
σ_B	axial stress at bottom punch
A	cross section area of specimen
H	height of the powder
σ_z	axial variation of stress
z	position of the slice from bottom of the powder
$\sigma_{average}$	average axial stress
μ	friction coefficient
W	width of the band area of curved faced tablet
R	radius of curvature
F_{ref}	reference force of curved faced tablet
\bar{F}	normalised force

Chapter 1. Introduction

1.1 Powder compaction in industry

Powder materials are widely used in different industries. One of the most important methods for forming powder materials is the compaction technique, a process which transforms loose powder into a compacted product with a higher density. This powder processing is used in the manufacture of net shaped components for a wide range of applications. For example, it is extensively used in the automotive industry where structural components that are subject to high loads are manufactured. Other applications include ceramic components, detergents, pharmaceutical tablets, etc.

The manufacturing process for powder components can be divided into a number of stages as illustrated in Figure 1-1.

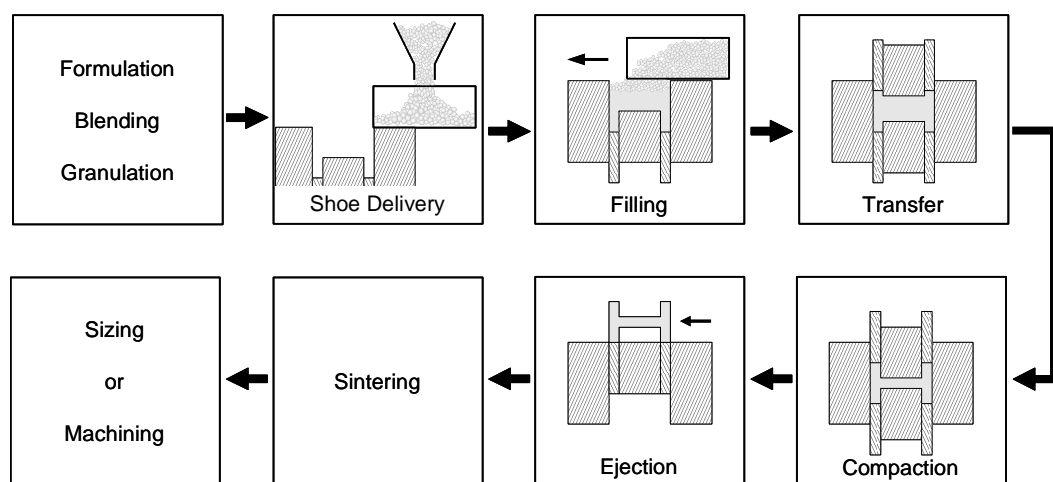


Figure 1-1 Manufacturing process for powder components (from Schneider, 2003)

The die filling process includes the delivery of powder to a feed shoe which moves over a die during the filling process and the flow of powder into the die. After filling,

the powder is transferred within the die through a series of tool motions to form an aggregate which is proportional to the final shape. During this process, the powder is still loose.

The subsequent compaction process itself also involves a number of stages. A rearrangement of particles occurs during the initial stage of compaction. While particles are in loose stage, localised deformation occurs at the contact point between particles. Such a rearrangement results in deformation of a powder compact and the plastic deformation of these particles. As particles slide over each other, the frictional resistance can also contribute to the macroscopic response of the powder compact. The initial stages of compaction are dominated by particle rearrangement, with little or no plastic deformation occurring between the contacting particles. Macroscopic plastic deformation under constrained compressive stress states is dominated by plastic deformation of the particles themselves. The internal structure significantly changes during the compaction process as the powder is transformed from a loose state into a dense compact. As the powder densifies, higher compaction pressure is required to exceed the local flow stress of powder particles. During the compaction process, the friction between the powder and the die wall plays a key role in the final density distribution of the compact. At the unloading and ejection stage, the component is subject to tensile stresses from the die. Therefore, in order to avoid cracking, the sequence of tool motions needs to be carefully controlled to minimise the magnitude of tensile stresses. After compaction, ceramics, hard metals and powder metallurgy components are sintered and further operations can be performed.

1.1.1 Powder metallurgy (PM)

Metal powder with specific attributes of particle size, shape and packing can be converted into a strong, precise, high density near net shape part. Key steps of metal powder forming process include shaping of the powder and the subsequent sintering process. This process has the advantages of relatively low energy consumption, high material utilisation and low capital costs. Moreover, PM is a flexible manufacturing process, capable of delivering a wide range of new materials, microstructures and properties that create unique functionality, such as wear resistant composites. The PM approach can also be used to produce materials which are difficult to process. Presently, the main consumption of PM parts is in the automotive industry. However, the PM process is only economical when production rates are high since the tooling cost is quite appreciable.

The three main steps in the scheme of PM are illustrated in Figure 1-2. The first concern is the nature of powders, such as the microstructure, size and shape of powder particles. The main activities in the processing step are the compaction of powder and the sintering of green compact. Finally, the product is tested for its final properties, such as strength, density and microstructure. An example of the common PM product is given in Figure 1-3.

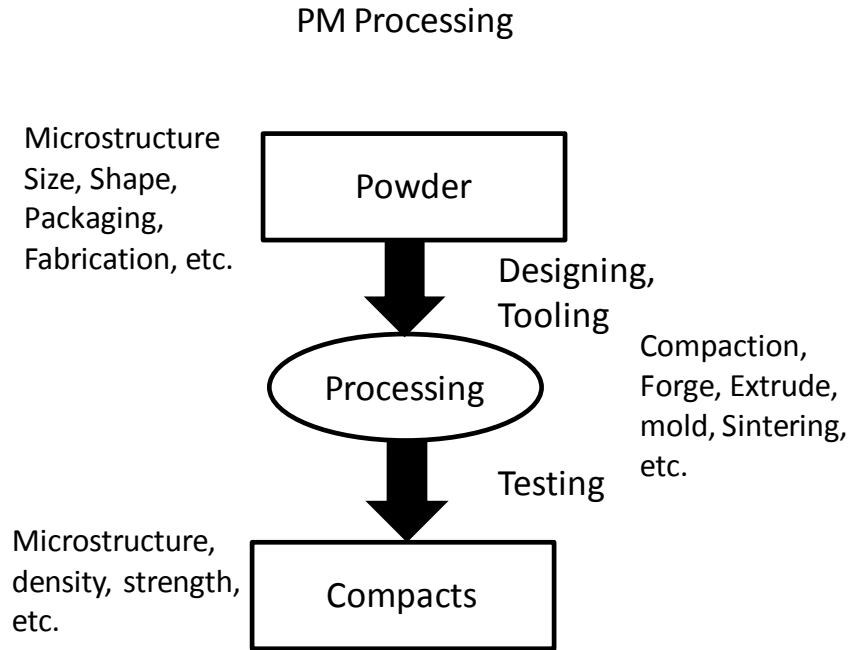


Figure 1-2 The concept flow for powder metallurgy from powder processing to final product (from Randall, 1997)

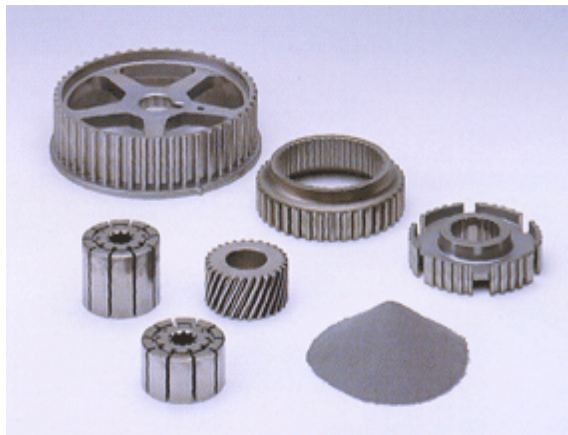


Figure 1-3 PM parts (gear components) made by powder (from Sinotech limited, UK)

The growth in PM will continue in the following aspects: 1) High volume production of precise, high quality parts from ferrous alloys; 2) Consolidation of high performance materials (i.e. full density, reliability); 3) Fabrication of difficult to process materials,

where fully dense high performance alloys can be fabricated with uniform microstructures; 4) Economical consolidation of specialty alloys, typically composites containing mixed phases. 5) Processing of complex parts with unique ingredients. The use of metal powder is growing faster than other metal working technologies. The future of PM will see more challenges on cost saving, reliability, quality, strength, dimensional control and unique shaping capabilities. More diverse applications will also appear in magnetic alloys, new aircraft alloys, improved metal matrix composites, etc. (Randall, 1997).

The analysis of powder compaction is important, because the green compaction influences further densification of the samples during sintering. The variation in density of the green compaction may cause shape distortion after sintering. A material model with the knowledge of material and friction behaviour is necessary to perform the analysis.

1.1.2 Ceramics industry

Ceramic powder is another popular material in the powder industry. Applications of ceramic products can be seen in: a) Aerospace: engines, space shuttle tiles, rocket nozzles, etc.; b) Electronics: capacitors, transducers, isolators, etc.; c) Biomedical: artificial bones, biodegradable splints, etc.; d) Optical: optical fibres, laser amplifiers, etc. Examples of ceramic components used in industry are illustrated in Figure 1-4.



Figure 1-4 Ceramic components (from Ceramic Substrates and Components Ltd, UK)

The processing steps of dry ceramic material generally follow the sequence: Milling, Mixing, Forming and Sintering. First, the raw ceramic material needs to be reduced to smaller size particles. The milling breaks up cemented material by mechanical means, such as attrition, compression or impact. The material is then mixed according to recipes and formed into desired shapes. After the forming process, the green part products are produced. Generally, the green parts are fragile and weak. Like PM process, the sintering process is normally necessary to achieve an industrial standard for ceramic material. In ceramic industry, the powder compact may be required to have such qualities as purity, electric isolation, filter ability, etc.

1.1.3 Pharmaceutical industry

Powder technology is also widely applied in pharmaceutical industry. Pharmaceutical powder is relatively light compared to metal and ceramic powders. The significant difference between a pharmaceutical powder process and a metal or ceramic powder process is that the green compact of the pharmaceutical powder is the final product,

while for a metal or ceramic powder the subsequent sintering procedure is often required. Examples of pharmaceutical tablets made by compaction are illustrated in Figure 1-5.



Figure 1-5 Pharmaceutical tablets (from Wickham Laboratories Ltd, UK)

Approximately 80% of all medication is administered in solid dosage forms and half of these are compressed tablets (Hiestand, 2003). Tablets are complex powder systems containing one or more active ingredients and a range of excipients to achieve both mechanical strength and chemical effect. The simplest formulation and process of pharmaceutical powder involve: powder mixing, die filling and compression. Active pharmaceutical ingredients and excipients are first mixed into a powder form. This powder is then transferred into a die and pressed to form tablets. In industry today, the production of pharmaceutical tablets is usually by the rotary press which has a high volume production (100,000-1,500,000 tablets per hour). Compaction is achieved on a rotary press by compacting the pharmaceutical powder in a die using a controlled sequence of punch motions. Tablets can be made into complex shapes, although most of the tablets are round, oval and capsule shaped due to the requirement of patients

and tableting machines. In pharmaceutical industry, chemical stability and bioavailability (i.e. disintegration and dissolution) as well as the mechanical strength of tablets are the main concerns. The tablets should have sufficient mechanical strength so that they will not fail during post-compaction operations, such as coating, handling, packaging and shipping. However, during and after compaction tablets can develop defects such as crack, delaminating, chipping, capping erosion, etc., which may be induced by insufficient material strength or flaws caused by the porosity and microstructure of the tablets. The internal structure of tablets, such as density distribution and cracks, has been studied by researchers (Sinka et al., 2004 and Wu et al., 2005) using X-ray computerised tomography (CT).

1.2 Compaction methods

The compaction methods are generally classified into two approaches: static compaction method and dynamic compaction method. The static method normally uses a steady loading rate in one or all loading directions until the powder aggregate meets the density or geometry requirement, while the dynamic method employs a dynamic loading condition using a loading hammer or vibration and it is normally used for large scale (Wu, 2005a). In this thesis only the static loading condition is considered. For the static compaction method powder compaction is usually done through isostatic (Govindarajan and Aravas, 1994) and uniaxial compaction techniques.

For isostatic compaction, powder is sealed in a rubber container and placed in an oil filled chamber. When the pressure of the chamber increases, the specimen will be subject to isostatic stress from all directions.

Uniaxial compaction technique is performed with pressure applied along axis using hard tooling. A significant number of uniaxial compaction experiments have been used (Briscoe and Rough, 1998, Turenne et al., 1999; Wikman et al., 2000; Guyoncourt et al., 2001 and Cunningham et al., 2004). Most compaction is performed using both an upper and lower punch. Due to the presence of friction, the uniaxial compaction technique is generally categorized into the followings as shown in Figure 1-6: single-action, double-action and floating die compaction (Wu, 2005a).

- Single-action compaction: Lower punch and die plate are fixed. The upper punch is loaded to generate stress within the powder mass (see Figure 1-6 a).
- The double-action compaction technique: fix the die plate, compaction is carried out from both top and bottom direction simultaneously (see Figure 1-6 b).

Floating die system: fix the bottom punch, die plate is fixed on springs, compaction is carried out from the top direction only. As the compaction continues, the friction will cause the die to move down and it will be balanced by the springs (see Figure 1-6 c).

Friction plays a key role in uniaxial compaction. The factors which influence the coefficient of friction between powder and die wall include: a) powder material; b) density; c) sliding velocity and d) contact pressure, etc.

To minimise friction, lubricants are added to the powder. Commonly used lubricants are: Zinc Stearate, Calcium Stearate, ethylene bis-stearamide etc. The double action and the floating die systems reduce density variation in specimen due to the effect of friction.

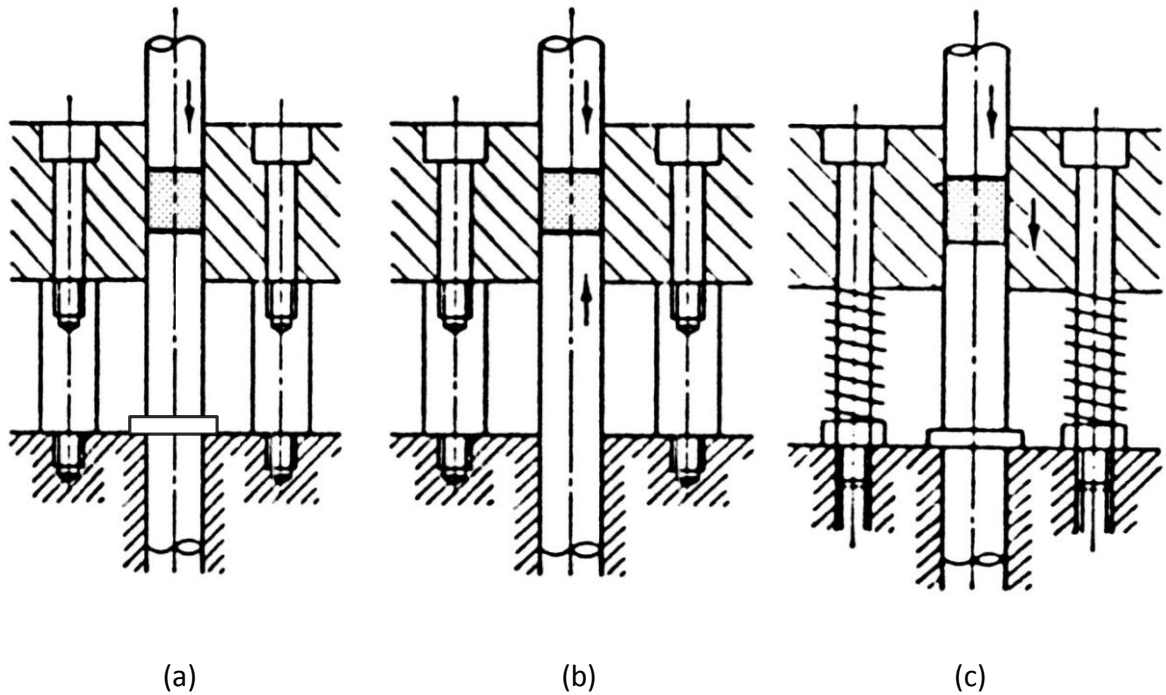


Figure 1-6 Different configuration of closed die system a)Single-action compaction system
b)Double-action compaction system c) Floating die system (from Wu, 2005a)

1.3 Compaction mechanisms

The compaction process of powders presents complex densification mechanisms. The compaction mechanism occurring at various stages are: rearrangement, contact between particles resulting in elastic and plastic deformation, fragmentation of particles, and formation of interparticulate bonds. The compaction stages are illustrated in Figure 1-7.

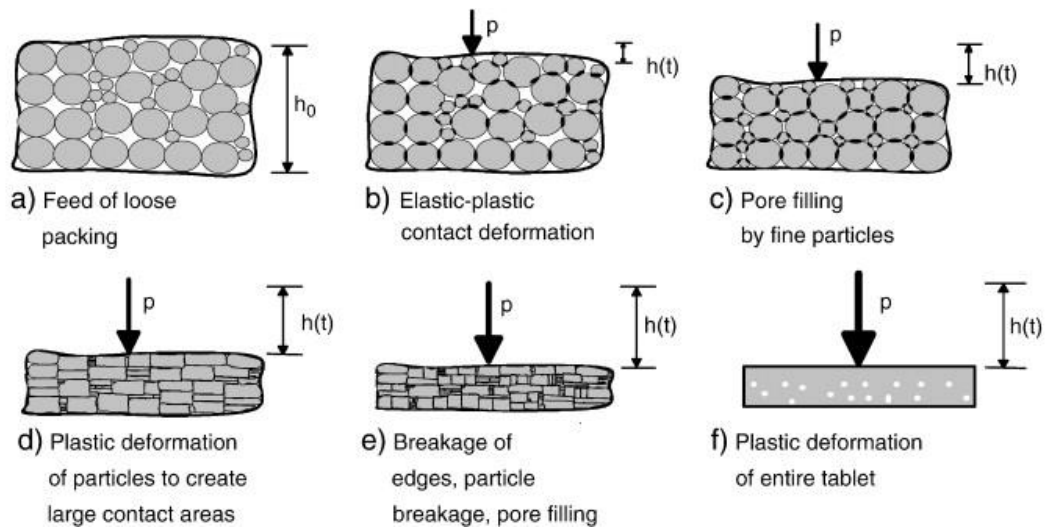


Figure 1-7 Sequence of micro-processes and deformation mechanism during press agglomeration (from Stasiak et al., 2010)

A constitutive law which can describe the mechanical behaviour should capture all of the above mechanisms from loose powder to fully dense material. Mechanical behaviour of powders, coupled with complex geometry and boundary conditions, make it impossible to have an analytical solution for analysing powder compaction. During the late 1980s, the maturing of numerical solutions to finite strain plasticity allowed initial attempts at modelling the powder compaction processes and more and more useful results have been published. Modelling becomes essential to the design of the compaction process.

1.4 Current trends in modelling powder compaction and compact strength

A common requirement across the powder pressing industries discussed above is to achieve a given density or density distribution in the green compact. Finite element

modelling can be used to understand and control density variations in powder compacts (Shang et al., 2011). General purpose finite element codes have been developed over the last 10-20 years which incorporate a wide range of constitutive models. However, it is not clear what complexity is required to model practical powder compaction processes. The capabilities and limitations of the established constitutive models is explored in the thesis.

Constitutive models require careful experimentation to generate material parameters. There are uncertainties related to data processing. For example, experimental errors related to the accuracy of the instruments inevitably exist. Moreover, there are no standard methods for calibrating constitutive models and data extraction procedures. These issues are addressed in the thesis.

Pharmaceutical tablets are required to have sufficient strength to withstand post-compaction operations. There are standard testing methods to measure the break force of the tablets and relate these to the tensile strength of the materials. However, these are limited to flat faced tablets while curved faced tablets are evaluated using an empirical equation (Pitt et al., 1988). A complete set of experiments is provided to examine the validity of this equation and develop new relationships between break force and material strength. Numerical methods for predicting the break force of curved faced tablets currently do not exist. In order to address the issues discussed above the following research objectives are formulated.

1.5 Research objectives

The overall goal of this thesis is to develop, implement and validate a material model for die compaction and to study the breakage behaviour of powder compacts experimentally and numerically. More specifically, the objectives of this thesis are to

- Study the compaction behaviour of different powder materials through experiments
- Determine the experimental inputs (i.e., constitutive and frictional parameters) for modelling die compaction and compact breakage
- Develop a parameter extraction algorithm for the constitutive model and friction
- Implement the material model for compaction and validate by experiments
- Study the breakage behaviour of powder compacts manufactured by the die compaction experimentally and numerically
- Propose a failure criteria to predict the break force of compacts and validate by experimental data

1.6 Thesis structure

The layout of this thesis is as follows

Chapter 2 provides a literature review of the constitutive laws for powder compaction and the research on the strength of green compacts. An established phenomenological model (Drucker-Prager Cap model) is chosen for modelling die compaction and subsequent strength testing.

The Finite Element Method (FEM) is introduced in Chapter 3 to model powder compaction at the length scale of powder compacts. Its successful applications in various powder industries are also illustrated.

Chapter 4 describes the calibration procedures of the material model, the manufacture procedure and the strength testing of the powder compacts.

Chapter 5 describes the instrumented die system for the constitutive model calibration. The detail of experimental setup of instrumented die system is provided, in which the forces of punches and radial stresses on die wall are measured.

Chapter 6 analyses the stress state within the compact during die compaction and proposes a method for parameter extraction of the constitutive model. Correction methods to account for the elastic compliance of the testing system are identified for both loading and unloading stage. The friction coefficient between powder and die wall is also determined and presented.

The fully calibrated model presented in Chapter 6 is validated in Chapter 7. In order to reproduce the forces applied by the top and bottom punches, it is necessary to implement the correct friction coefficient. The numerical prediction of unloading curve is also validated. Practical considerations of modelling die compaction are investigated starting from the simplest possible model that can capture powder behaviour during compaction.

Chapter 8 presents an experimental study of the break force of round pharmaceutical tablets with curved faces. The tablets are manufactured and tested using the

diametrical compression test method. An empirical equation relating the break force to material tensile strength is proposed. The failure patterns of tablets are examined.

Chapter 9 presents a numerical prediction of the break forces under diametrical compression using FEM. A fully calibrated model is implemented in the finite element package ABAQUS and three failure criteria are investigated to predict the break force numerically.

Finally, the overall conclusions and recommendation for future work from this research are drawn in Chapter 10.

Chapter 2. Constitutive laws for powder compaction

2.1 Material constitutive laws

In material engineering a constitutive law or a constitutive equation describes the relationship between a material deformation and external loading. The simplest constitutive law is Hooke's law for linear elastic materials developed by Robert Hooke (Simo and Hughes, 1998). In this case the constitutive law is a linear stress-strain relation valid for elastic loading/unloading. Plastic behaviour is described by yield condition, which identifies the stress states causing plastic flow. More complex constitutive models include the effects of strain, strain rate, microstructure, anisotropy, and time on stress- strain behaviour.

2.2 Modelling approaches for powder compaction

When powder is filled into the die, particles are in a loose state and thus each particle can be treated as a single body. At this stage, the response of the powder is governed by interactions between particles in contact, which leads to a rearrangement and volumetric and shear deformation. One of the well-known methods to address this powder behaviour is the so-called Discrete Element Modelling (DEM) approach developed by Cundall and Strack (1979). The DEM approach solves Newton's equations of motion and requires a contact law between particles. DEM has been used to model particulate flow in a range of processes such as fluidised beds (e.g. Tsuji et al., 1993) to shear cells (e.g. Thornton and Zhang, 2003), die fill (e.g. Wu and Cocks, 2006) and early stage compaction (e.g. Redanz and Fleck, 2001). Although contact laws exist for large deformation (Li et al., 2009), the contact laws in DEM do not consider

eventual interaction between neighbouring contact regions. Instead, the DEM model focuses on inter-particle behaviour where the material is described by many factors, such as the average number of contacts, the volume fraction, the orientation and distribution of contacts, the contact area and the length of links connecting the particle centroids. Since a representative part consists of a large number of particles, simplifications are necessary. For example, most researchers assume that the shape of particles is spherical. However, when simulating realistic problems this approach is impractical for computational reasons.

2.2.1 Continuum approach

As densification progresses, the response of powder aggregate exhibits a macroscopic behaviour like a continuum body. At this stage, the mechanical response is insensitive to the statistical variation presented at particle level. Powder can also be considered as a mechanical continuum on the basis that in practical powder compaction situations, the size of the particles is typically between a few μm and a few hundred μm , while the size of the compact is of the order of 10-100 mm.

Thus, the constitutive law for powder compact can be developed similar to continuous bodies. Yield surfaces can be developed based on experimental data, the concept of yield and plastic behaviour of fully dense material has been established (Hill, 1950). The determination of the yield surface involves the use of a number of different methods.

- Samples are prepared using the same loading condition (for example, hydrostatically compacted to the same relative density). Then each sample is

loaded along a different path in a stress space until it yields. The yield surface is hence formed by connecting all these yield points.

- Different tests can be used to determine the yield surface for powder compact as shown in Figure 2-1, such as simple shear, simple compression, triaxial compression (Koerner, 1971 and Doremus et al., 1995), closed die compaction (Watson and Wert, 1993), hydrostatic compression (Kim et al., 1990). In the figure, p is the hydrostatic pressure defined as

$$p = \frac{1}{3}(\sigma_{11} + \sigma_{22} + \sigma_{33}) \quad (2-1)$$

and is related to volume change. q indicates Mises equivalent stress and is defined as

$$q = \sqrt{\frac{1}{2}[(\sigma_{11} - \sigma_{22})^2 + (\sigma_{11} - \sigma_{33})^2 + (\sigma_{22} - \sigma_{33})^2] + 3\sigma_{12}^2 + 3\sigma_{13}^2 + 3\sigma_{23}^2} \quad (2-2)$$

where σ_{ij} ($i,j=1,2,3$) are the components of stress.

In this representation, the closer a point is to the ordinate (q axis), the more shear experienced in the material; the closer it is to the abscissa (p axis), the more hydrostatic pressure is experienced. It should be noted that results from a particular testing procedure can be used to extract material parameters for different constitutive models.

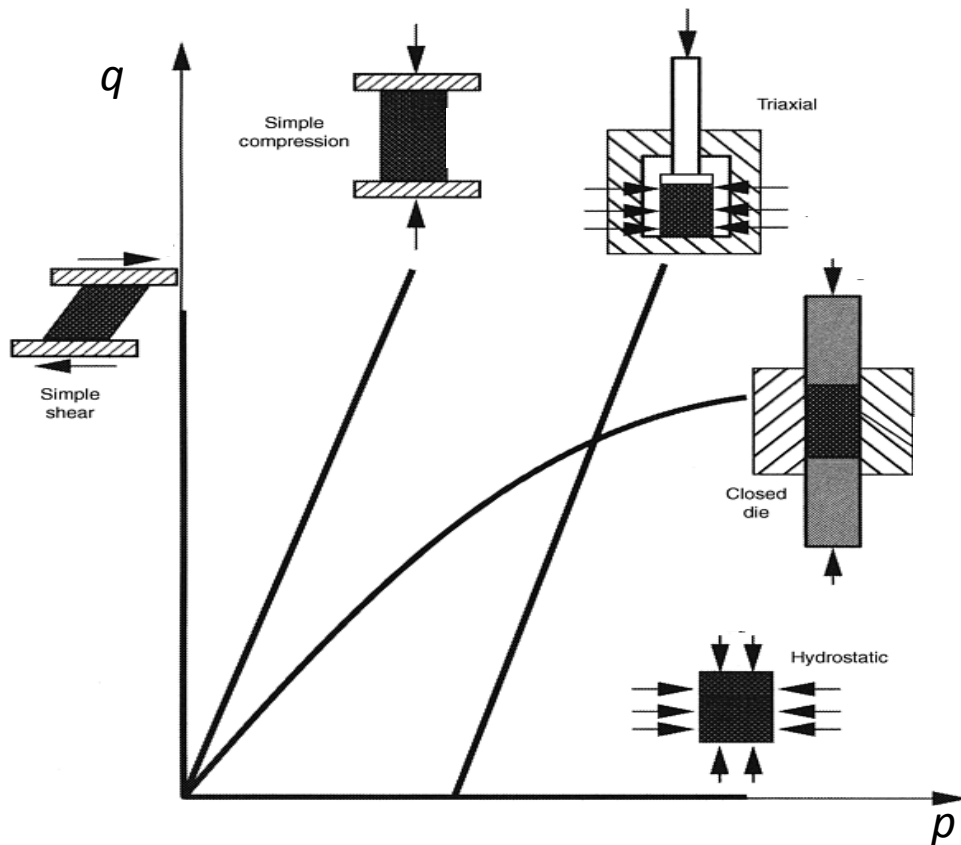


Figure 2-1 Schematic representation of the load paths corresponding to the different test procedures (from Wood, 1990)

The following sections review constitutive models which form the foundation of current models used to predict material response more accurately in the powder industry.

2.2.1.1 Gurson model

Models based on the micromechanical principles that describe void nucleation in fully dense materials (Gurson, 1977) have been modified (Tvergaard, 1981) and extended to model materials with significant porosity. It became known as the porous plasticity model (as shown in Figure 2-2). The yield surface of is expressed as

$$F' = \left(\frac{q}{P_y}\right)^2 + 2f_o \cosh\left(\frac{\sqrt{3} p}{2 P_y}\right) - (1 + f_o^2) = 0 \quad (2-3)$$

where P_y is the hydrostatic yield stress, f_o is the macroscopic porosity

This model assumes the same strength in tension and compression. To address this issue constitutive models developed from the rock and soil mechanics literature such as Cam-Clay (Schofield and Wroth, 1968) and Drucker-Prager (Drucker and Prager, 1952) have been adapted for powder compaction.

2.2.1.2 Cam-Clay model

Cam-Clay model is developed by Schofield and Worth (1968) which predicts a smooth yield surface calibrated by experimental data. Later the model was simplified (Wood, 1990) so that the yield surface is a quadratic expression of the deviatoric and mean stress. The ellipse passes through the origin as shown in Figure 2-2. A consequence of this is that the body cannot support any tensile stresses. The expression for the yield surface is written as

$$F' = \frac{p}{P_y} \left(\frac{p}{P_y} - 1\right) + \left(\frac{q}{MP_y}\right)^2 = 0 \quad (2-4)$$

where M is a constant controlling the shape of the surface and P_y is the hydrostatic yield stress which is required to compact the sample hydrostatically to the same relative density.

Figure 2-2 illustrates yield surfaces calibrated from the same closed die compaction experiment data for 3 types of models (porous plasticity, Cam-Clay and Drucker-Prager cap). The Drucker-Prager model is presented in detail in section 4.3.

In the vicinity of the closed die compaction point, the models are almost identical, therefore the prediction would be similar. However, difference would be obtained for higher shear stress states. Therefore, the selection of the model and the design of calibration experiments become important for high shear stresses (e.g., roller compaction of powder, Cunningham, 2004) or tensile stresses (defect formation, Coube and Riedel, 2000).

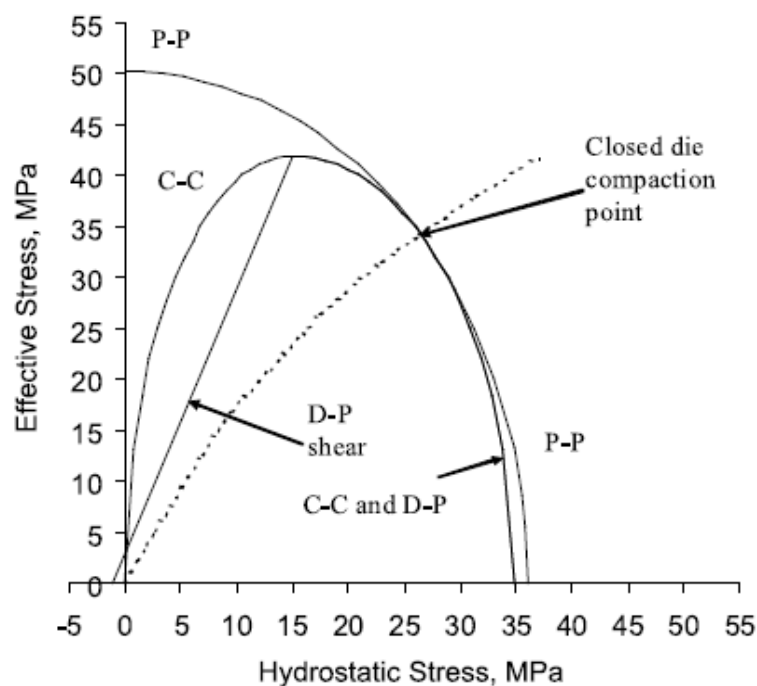


Figure 2-2 Yield surfaces for microcrystalline cellulose using various models calibrated on a closed-die compaction experiment: C-C Cam-Clay, D-P Drucker-Prager cap, P-P porous plasticity. The closed-die compaction trajectory is indicated with a dotted line (from Sinka, 2007).

The use of continuum models for powder compaction has been presented in several review articles (Trasorras et al., 1998; Cocks, 2001; Zavaliangos, 2002; Sinka, 2007). In principle, continuum models can be used over the entire densification range, however,

dilation and localisation events occurring at low density may not always be adequately described. Nevertheless, continuum models are widely used for practical purposes. Constitutive models described above can be expressed using state variables to capture the evolution of constitutive properties as the powder is densified. Often a single state variable (e.g. relative density) is used. In practice, the densifying material undergoes complex stress states and loading conditions (see Figure 1-7). As a result, the material structure is no longer isotropic and therefore it will not be appropriate to describe this structure using a single state variable. For example, consider the case of frictionless closed die compaction. As a cylinder is compacted along its axis, the macroscopic radial strain is zero. The contact patches that develop between the deforming particles are therefore larger normal to the direction of loading than along the axis. Also, the size of these patches is different from those in a compact that has been densified hydrostatically to the same relative density. Thus, the relative density does not uniquely describe either the microstructure or the macroscopic response. The dependence of the behaviour on the loading path has been investigated by others (Koerner et al., 1971, Fleck, 1995, Akisanya et al., 1997, Schneider and Cocks, 2002 and Schneider, 2004). Fleck (1995) and Fleck et al. (1997) demonstrated that the shape of the yield surface depends on the loading history and is not only a function of density. Figure 2-3 shows that the yield surface of closed die compaction is completely different from that of isostatic compaction. This behaviour can be estimated analytically using micromechanical models.

2.2.1.3 The micromechanical model of Fleck

Micromechanical models use contact laws to describe the interaction between particles. Fleck (1995) developed a yield function for the behaviour of an array of spherical particles for an early stage of compaction

$$F' = \left(\frac{\sqrt{5}p}{3P_y} \right)^2 + \left(\frac{5q}{18P_y} + \frac{2}{3} \right)^2 - 1 = 0 \quad (2-5)$$

The model is based on plastic deformation which occurs at the contact of particles. It is valid when the plastic zones are isolated i.e. there is no interaction between the deformation zones.

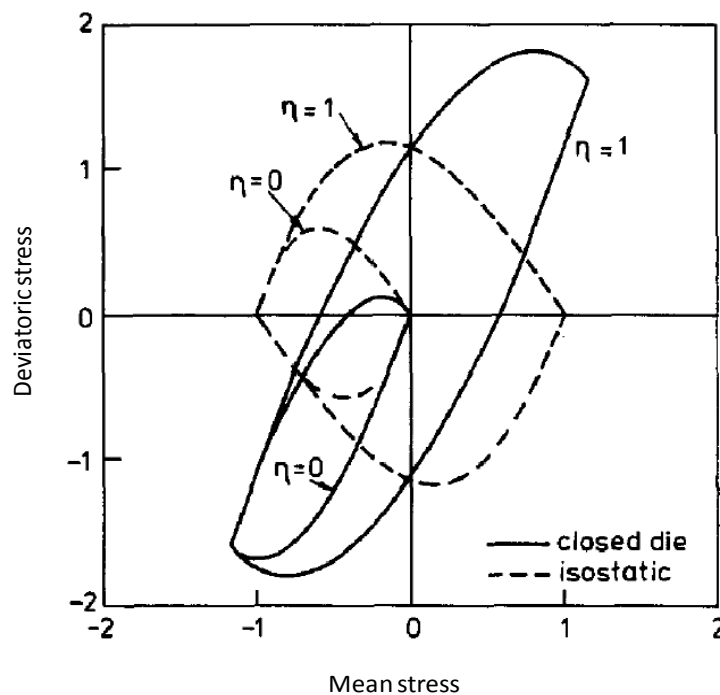


Figure 2-3 Fleck's predicted yield surface is given for both isostatic compaction and close die compaction. Contacts are frictionless and two limits cohesion: full cohesion ($\eta = 1$) and cohesionless ($\eta = 0$) are presented (from Fleck, 1995).

The shape of yield surface shows good agreement with experimental result determined by Akisanya et al. (1997).

Micromechanical models are also important in creating a theoretical basis for the development of incremental and deformation plasticity (Sinka and Cocks, 2007 and Cocks and Sinka, 2007) models for powder compaction.

The specific features of the powder response during compaction can be summarised as

1. Like rocks and other porous materials, the strength of powder compacts in tension is lower than the strength in compression. Models should therefore include the effect of hydrostatic stress.
2. The state of the material changes from loose powder into a dense compact. Although it has been questioned whether or not density is an appropriate state variable (Cocks and Sinka, 2007), density is still widely used for practical purposes. In spite of the shortcomings discussed above single state variable models have become well established in many powder compaction modelling applications (PM Modnet Research Group, 1999 and 2002, Kim et al., 2002, Sinka et al., 2004, Khoei and Azizi, 2004, Khoei and Azami, 2005).
3. The material behaviour is dependent on loading path. For example a compact made by isostatic compaction presents a different yield surface from a compact of the same density made using die compaction.

The discussion above highlights a number of features that must be taken into account when developing constitutive models for powders. For practical purposes, however, it is clear that simplification is required. An empirical model, the Drucker-Prager Cap (DPC) model, has gained wide acceptance and practical use as documented by recent publications from large Europe-wide projects (PM Modnet Research Group, 1999 and 2002; Brewin et al. (eds.), 2008). The DPC has been employed throughout this thesis and the detail of this yield surface is provided in Chapter4.

Density is chosen as state variable because in industrial powder pressing operations, the aim is often to manufacture a compact with a given density or a prescribed density distribution. For example, a structural powder metallurgy component should have high density (to maximise strength) and small internal density variations (to minimise distortions during sintering), the green part should be crack free, etc. A pharmaceutical tablet should have high density (for strength to hold together during handling and post-compaction operations, coating, packaging etc.).

2.3 Strength of green powder compact

The mechanical strength of compacted powder after its ejection from the die is called “green strength”. For ceramic and metal powder, the green strength of the powder compaction is very different from that of sintered powder compacts (Brown and Weber, 1988). Researches on the metal powder suggest that the green strength of powder compact increases with the density (Coube and Riedel, 2000, Doremus et al., 2001).

In recent years, powder compaction technology is widely used in pharmaceutical industry. Unlike ceramic or metal powder industry, pharmaceutical tablets after

compaction are close to the final products. Green compact after ejection from the die can be used to determine several material properties. One of the most important characteristics of powder compact is that the components have sufficient strength to allow transferring and handling. Simply, strength tests determine the limit of material performance to stress. The evaluation of strength is often performed by simple tests, such as uniaxial and diametrical compression test, directly on compacts or parts without any machining and shaping. For many years, the tensile strength of pharmaceutical compacts has been determined by diametrical compression test. The basis of the method is Hertz's contact theory (Timoshenko and Goodier, 1970) which shows that when a thin disk made of a linear elastic material is loaded across the diameter between rigid platens, a uniform tensile state of stress develops through the centre of the specimen. For this reason, the test method is also known as "indirect tensile test" or "Brazilian test" (Carneiro and Barcellos, 1953 and Akazawa, 1953) which was used for measuring the tensile strength of rock from drill cores. Jaeger and Cook (1976) found that measurements are very reproducible and in reasonable agreement with values obtained in uniaxial tension for rock material. Diametrical compression test is widely used to determine tensile strength of rock material (Hudson et al., 1972), ceramics (Shetty et al., 1986), pharmaceutical material (Fell and Newton, 1970) and other brittle materials.

The constitutive models described above have been implemented in finite element programmes to model powder compaction. In the next chapter we review the fundamentals of the finite element method.

Chapter 3. Finite element analysis of powder compaction

Since the powder compaction process involves large deformations, large strain, compressibility, nonlinear material behaviour and friction, the numerical analysis of such process can lead to computational issues. The finite element method (FEM) lends itself for modelling this process.

FEM simulation is used for modelling in powder industry because: 1) the size of the particles is usually more than two orders of magnitude smaller than the dimensions of the die. 2) interaction between particles is combined and included in the parameters of a dependent constitutive model. The FEM is the numerical technique where a solution of a boundary value problem which is a set of partial differential equations is found. These equations represent balance laws (conservation of mass, momentum balance, and energy) and constitutive laws (stress-strain relation and friction laws). The FEM can make a valuable contribution to the design of the compaction process and prediction of powder behaviour. Expensive and time consuming steps, such as manufacturing pressing tools, trial pressing, sintering and strength testing, could be replaced by FEM.

3.1 The finite element method

In powder compaction, irregular geometry and complicated boundary and loading conditions make it impossible to solve the whole process analytically. The FEM enables an approximate solution. Within the finite element method the body under consideration is discretised into a number of elements and nodes. The finite element model representing the body therefore contains a finite number of degrees of freedom and the implication is that the requirement for equilibrium cannot be

satisfied exactly at every point in the continuum. Instead, a weak form can be obtained by considering of the principle of virtual work. The FEM is a numerical technique for getting approximate solutions of partial differential equations which are derived as follows. In Figure 3-1, a material body with the initial domain Ω_0 , initial boundary Γ_0 , initial position \mathbf{x}_0 , initial velocity \mathbf{v}_0 , deforms with the displacement \mathbf{u} . At any time t , the material body occupies a domain Ω with a surface area Γ , velocity \mathbf{v} and position \mathbf{x} .

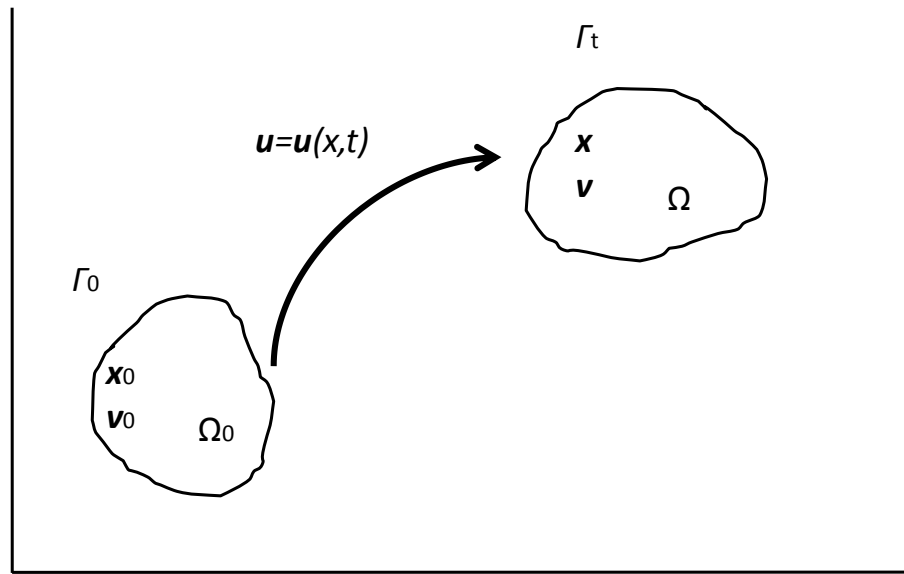


Figure 3-1 Configuration of a deformed material body

The total force applied is given by

$$\tilde{\mathbf{f}}(t) = \int_{\Omega} \rho \mathbf{b}(\mathbf{x}, t) d\Omega + \int_{\Gamma_t} \boldsymbol{\tau}(\mathbf{x}, t) d\Gamma_t \quad (3-1)$$

where $\tilde{\mathbf{f}}$ is the force, ρ is the density, \mathbf{b} is the body force and $\boldsymbol{\tau}$ is the surface traction.

The linear momentum of the material body $\tilde{\mathbf{p}}(t)$ can be expressed by the velocity of

the material body $\mathbf{v}(\mathbf{x}, t)$ as

$$\tilde{\mathbf{p}}(t) = \int_{\Omega} \rho \mathbf{v}(\mathbf{x}, t) d\Omega \quad (3-2)$$

By momentum conservation, we have

$$\frac{d}{dt} \int_{\Omega} \rho \mathbf{v}(\mathbf{x}, t) d\Omega = \int_{\Omega} \rho \mathbf{b}(\mathbf{x}, t) d\Omega + \int_{\Gamma_t} \boldsymbol{\tau}(\mathbf{x}, t) d\Gamma_t \quad (3-3)$$

By using material time derivative (Reynold's theorem), equation (3-3) can be written

as

$$\begin{aligned} \frac{d}{dt} \int_{\Omega} \rho \mathbf{v}(\mathbf{x}, t) d\Omega &= \int_{\Omega} \left(\frac{d(\rho \mathbf{v}(\mathbf{x}, t))}{dt} + \rho \mathbf{v}(\mathbf{x}, t) \nabla \cdot (\mathbf{v}(\mathbf{x}, t)) \right) d\Omega \\ &= \int_{\Omega} \left(\rho \frac{d(\mathbf{v}(\mathbf{x}, t))}{dt} + \mathbf{v}(\mathbf{x}, t) \left(\frac{d\rho}{dt} + \rho \nabla \cdot \mathbf{v}(\mathbf{x}, t) \right) \right) d\Omega \end{aligned} \quad (3-4)$$

in which

$$\frac{d\rho}{dt} + \rho \nabla \cdot (\mathbf{v}(\mathbf{x}, t)) = 0 \quad (3-5)$$

is a statement of mass conservation. From equation (3-3) and (3-4), we have

$$\int_{\Omega} \rho \mathbf{b}(\mathbf{x}, t) d\Omega + \int_{\Gamma_t} \boldsymbol{\tau}(\mathbf{x}, t) d\Gamma_t = \int_{\Omega} \rho \frac{d(\mathbf{v}(\mathbf{x}, t))}{dt} d\Omega \quad (3-6)$$

The divergence theorem gives

$$\int_{\Gamma_t} \boldsymbol{\tau} d\Gamma_t = \int_{\Gamma_t} \mathbf{n} \cdot \boldsymbol{\sigma} d\Gamma_t = \int_{\Omega} \nabla \cdot \boldsymbol{\sigma} d\Omega \quad (3-7)$$

Where $\boldsymbol{\sigma}$ is the Cauchy stress tensor and \boldsymbol{n} is the pointing unit normal to the surface.

Equation (3-6) then becomes

$$\int_{\Omega} \rho \mathbf{b}(\mathbf{x}, t) d\Omega + \int_{\Omega} \nabla \cdot \boldsymbol{\sigma}(\mathbf{x}, t) d\Omega = \int_{\Omega} \rho \frac{d(\mathbf{v}(\mathbf{x}, t))}{dt} d\Omega \quad (3-8)$$

Equation (3-8) is known as the strong form.

3.2 Finite element method for non-linear material and large deformation

3.2.1 Finite element discretisation

The forming process in powder compaction problems is a large deformation process.

The calculation region is mapped using elements. The Lagrangian formulation which describes the material behaviour with respect to either the original domain or the domain at previous step is sufficient for powder forming process (Hibbitt et al., 1970 and Zienkiewicz and Taylor, 1989). The elasto-plastic constitutive law is used most commonly.

Equation (3-8) is in strong form and cannot be conveniently solved numerically since it requires spatial derivative of the stress field. Following the standard procedure of the FEM, the domain Ω is divided into subdomains (elements). By applying virtual work principle, equation (3-8) can be written in a weak form of

$$\int_{\Omega} \delta \boldsymbol{\varepsilon}^T \boldsymbol{\sigma} d\Omega - \int_{\Omega} \delta \mathbf{u}^T \rho \boldsymbol{\sigma} d\Omega + \int_{\Omega} \delta \mathbf{u}^T \rho \dot{\mathbf{u}} d\Omega - \int_{\Gamma_t} \delta \mathbf{u}^T \bar{\mathbf{t}} d\Gamma = 0 \quad (3-9)$$

The weak form in equation (3-9) does not require the continuity of the stress field and can be readily used for the FE discretisation. Applying the standard finite element

Galerkin discretisation process to equation (3-9) with the independent approximations of \mathbf{u} defined as $\mathbf{u} = \mathbf{N}_u^T \bar{\mathbf{u}}$, we have

$$\int_{\Omega} \bar{\mathbf{B}}^T \boldsymbol{\sigma} d\Omega + \mathbf{M} \ddot{\bar{\mathbf{u}}} - \mathbf{f}_u = 0 \quad (3-10)$$

where the mass matrix, \mathbf{M} and the load vector, \mathbf{f}_u are defined as

$$\mathbf{M} = \int_{\Omega} \mathbf{N}_u^T \rho \mathbf{N}_u d\Omega \quad (3-11)$$

$$\mathbf{f}_u = \int_{\Omega} \mathbf{N}_u^T \rho \mathbf{b} d\Omega + \int_{\Gamma_t} \mathbf{N}_u^T \bar{\mathbf{t}} d\Gamma \quad (3-12)$$

and $\bar{\mathbf{B}}$ is strain matrix relating the increments of strain to displacement (i.e. $d\boldsymbol{\varepsilon} = \bar{\mathbf{B}} d\bar{\mathbf{u}}$). The bar suffix is added as, if large displacement, the strains depend non-linearly on displacements and the matrix $\bar{\mathbf{B}}$ is dependent on $\bar{\mathbf{u}}$.

$$\bar{\mathbf{B}} = \mathbf{B}_L + \mathbf{B}_{NL}(\bar{\mathbf{u}}) \quad (3-13)$$

where \mathbf{B}_L is the linear infinitesimal strain- displacement matrix, \mathbf{B}_{NL} is the nonlinear strain-displacement matrix. Thus, we have

$$d\bar{\mathbf{B}} = d\mathbf{B}_{NL} \quad (3-14)$$

In order to obtain the tangential stiffness matrix, equation (3-10) and (3-14) is rewritten as a nonlinear function of nodal displacement $\bar{\mathbf{u}}$.

$$\Psi(\bar{\mathbf{u}}) = \int_{\Omega} \bar{\mathbf{B}}^T(\bar{\mathbf{u}}) \boldsymbol{\sigma} d\Omega + \mathbf{M}\ddot{\mathbf{u}} - \mathbf{f}_u = 0 \quad (3-15)$$

Take variation of equation (3-15) with respect to $d\bar{\mathbf{u}}$, we have

$$d\Psi = \int_{\Omega} d\bar{\mathbf{B}}^T \boldsymbol{\sigma} d\Omega + \mathbf{M}d\ddot{\mathbf{u}} + \int_{\Omega} \bar{\mathbf{B}}^T d\boldsymbol{\sigma} d\Omega \quad (3-16)$$

Substituting the constitutive law definition with respect to the incremental stress, i.e.

$d\boldsymbol{\sigma} = \mathbf{D}_T d\boldsymbol{\varepsilon}$, and relation (3-14) into equation (3-16), we have

$$d\Psi = \int_{\Omega} d\mathbf{B}_{NL}^T \boldsymbol{\sigma} d\Omega + \mathbf{K}_T d\bar{\mathbf{u}} + \mathbf{M}d\ddot{\mathbf{u}} \quad (3-17)$$

where

$$\mathbf{K}_T = \int_{\Omega} \bar{\mathbf{B}}^T \mathbf{D}_T \bar{\mathbf{B}} d\Omega = \mathbf{K}_L + \mathbf{K}_{NL} \quad (3-18)$$

$$\mathbf{K}_L = \int_{\Omega} \mathbf{B}_L^T \mathbf{D}_T \mathbf{B}_L d\Omega \quad (3-19)$$

$$\mathbf{K}_{NL} = \int_{\Omega} (\mathbf{B}_L^T \mathbf{D}_T \mathbf{B}_{NL} + \mathbf{B}_{NL}^T \mathbf{D}_T \mathbf{B}_{NL} + \mathbf{B}_{NL}^T \mathbf{D}_T \mathbf{B}_L) d\Omega \quad (3-20)$$

where \mathbf{D}_T is the consistent tangential stiffness matrix. \mathbf{K}_L and \mathbf{K}_{NL} are the small displacement stiffness matrix and large displacement matrix respectively.

The first term of equation (3-17) can generally be written as

$$\int_{\Omega} d\mathbf{B}_{NL}^T \boldsymbol{\sigma} d\Omega = \mathbf{K}_{\sigma} d\bar{\mathbf{u}} \quad (3-21)$$

where \mathbf{K}_{σ} is a symmetric matrix dependent on the stress level.

Total tangential stiffness matrix is obtained

$$\bar{\mathbf{K}}_T = \mathbf{K}_L + \mathbf{K}_{NL} + \mathbf{K}_{\sigma} \quad (3-22)$$

All the ingredients necessary for computing the large displacement of powder forming problem are now available.

At each time step, the deformation of material can be calculated using equation (3-4) and the equation of motion. The stress calculated from the strain of each element and the constitutive law reflects the property of the material. The final nonlinear equations are solved by a Newton-Raphson iteration method (Zienkiewicz and Taylor, 1989).

3.3 Applications of finite element method in powder engineering

Finite element modelling results can be used to optimise the formulation of powder and the selection of process parameters for a given performance criterion. This approach is general for all classes of powders and can be used in formulation design and process development across the powder forming industries. The FEM has been widely used for simulating the compaction of metal and ceramic powder (Coube, 1998, PM MODENET, 1999 and 2002, Coube and Riedel, 2000) for over 2 decades. In recent years, the FEM has been used in pharmaceutical industry (Sinka et al., 2004a and Wu et al., 2005 and 2006). Technically, the powder aggregate is generally considered to be an elasto-plastic material with appropriate yield surfaces which are originally

developed from soil mechanics (Schofield and Wroth, 1968 and DiMaggio and Sandler, 1971).

In the following sections, examples of numerical simulation by applying FEM are illustrated for powder compaction. Two main aspects in powder compaction are discussed, which are density distribution and crack formation of powder compacts.

3.3.1 Example 1: The density distribution in curved faced tablets

The friction between powder and die wall induces the density variation in pharmaceutical tablets (Macleod and Marshall, 1977). The internal density distribution is important because it affects the local material properties, such as the bioavailability of the drug and mechanical strength of tablets.

This example illustrates the effect of friction between die wall and powder on the density distribution of curved faced tablets (diameter 25 mm, curvature radius 19.82 mm). These tablets are compressed using clean and lubricated tooling, which exhibits high and low friction coefficients respectively.

Figure 3-2 presents the density variations in two tablets which are compressed to the same relative density. The density contours shown in Figure 3-2a and b were determined using indentation hardness mapping by Sinka et al. (2003). The modelling results were obtained by implementing a density dependent DPC model which is facilitated in finite element package ABAQUS/Standard.

For the low friction case (prelubricated die), the variable friction coefficient data was used. For high friction, the friction coefficient was taken as a constant value 0.5. The relative density distribution predicted using high and low friction are presented in

Figure 3-2c and d , which are in good agreement with experimental density map. It can be seen from Figure 3-2 that the two identical tablets in terms of shape, weight and material have a different density distribution only due to the friction condition applied, i.e. for high friction case, the maximum density built up at the contact region between the powder and the die wall, while for low friction condition, the highest density locates in the middle of the tablets. As a result, these two tablets have different microstructures which affect their strength, friability, disintegration and failure behaviour.

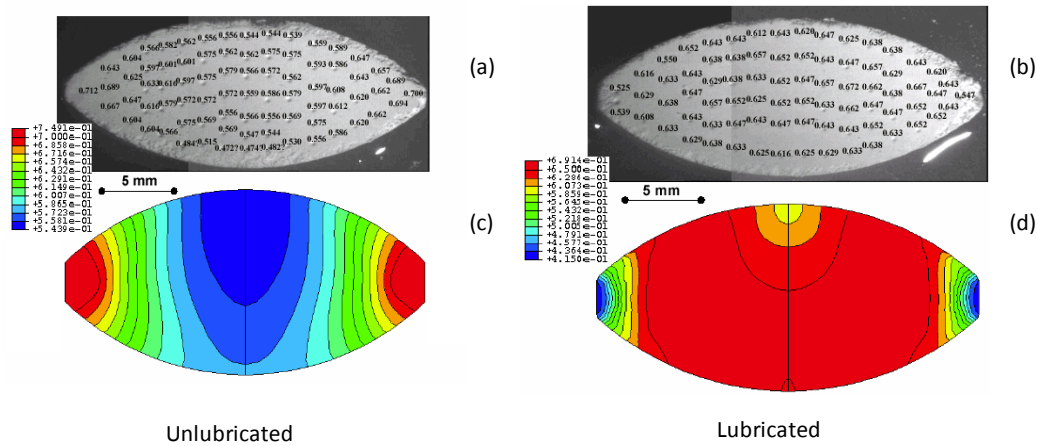


Figure 3-2 Relative density distribution in curved faced tablets. Experimental data for tablet compressed using a) clean and b) lubricated tooling. Numerical results for c) high and d) low friction coefficient (from Sinka et al., 2003)

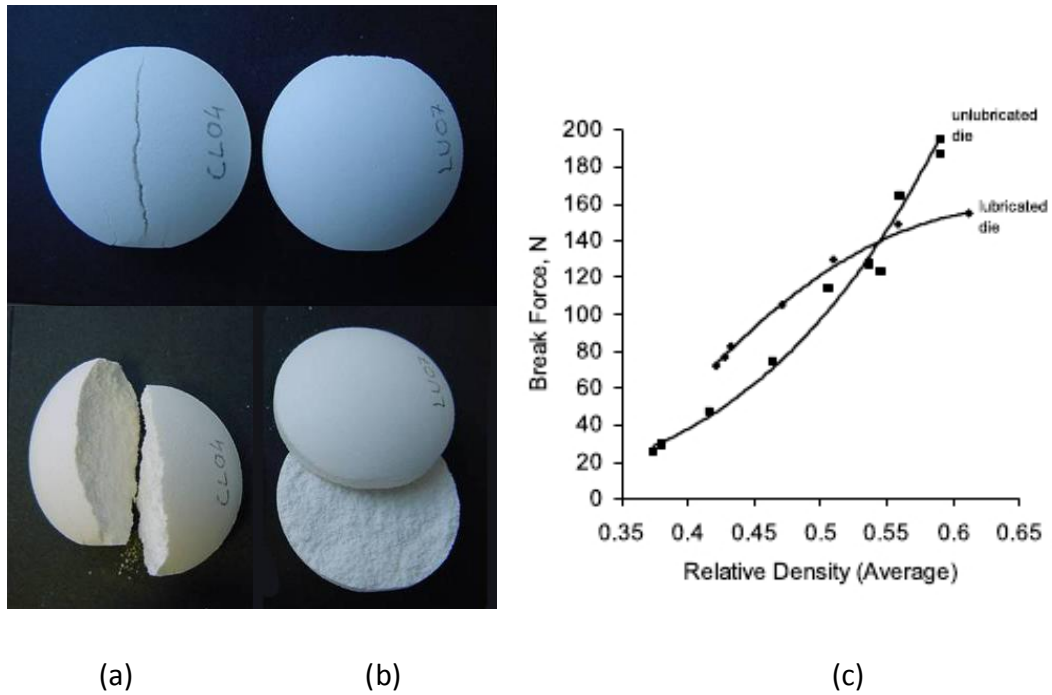


Figure 3-3 The failure mode of pharmaceutical tablets during diametrical compression test a) unlubricated friction condition, b) lubricated friction condition and c) break force in diametrical compression experiments (from Sinka et al., 2004)

3.3.2 Example 2: Defects of powder compacts

Example 2 discusses the important issue of crack formation which is a common defect during powder compaction process. Wu and co-workers (2005) employed X-ray CT to observe crack of round tablets with flat face using lactose powder. It has been illustrated in Figure 3-4 that a cone-shaped failure exists in the tablet. Numerical simulation was performed by Wu et al. (2005) using a DPC model. It is demonstrated in Figure 3-4b that the crack formation is due to the development of intensive shear bands during unloading.

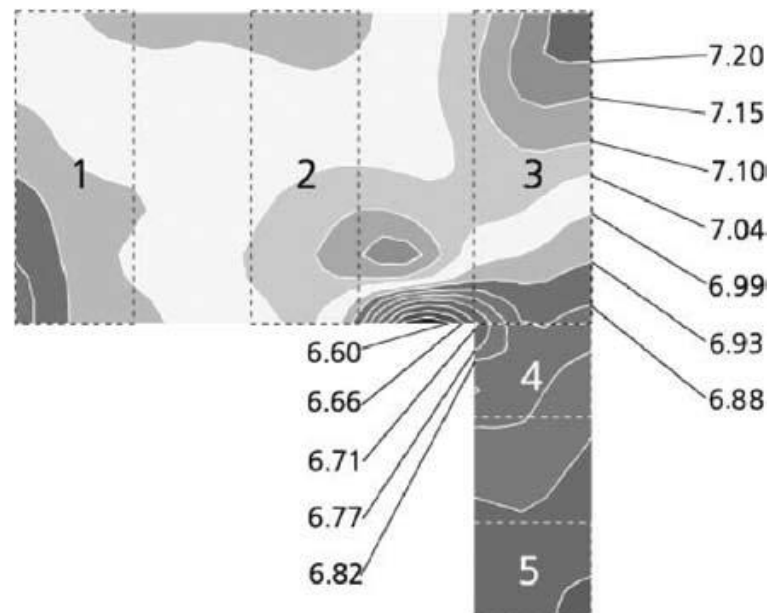


Figure 3-5 Crack development in multilevel parts made of metallic powder (from Coube and Riedel, 2000)

3.4 Summary

In this chapter, the finite element method was introduced. Since powder compaction is a process involving large deformations, large strain, nonlinear material behaviour and friction, the numerical analysis of such a highly nonlinear process is a formidable computational problem. The large deformation analysis of powder during the compaction process is simulated by the FEM. As the compaction process involves large reduction in volume, a large displacement finite element formulation was used.

Two examples which are considered to be successful applications of FEM in powder industry are reviewed. These examples considered density distributions and crack formation in green compacts which are the main concern in powder compaction. Moreover, the examples illustrate that the numerical analysis of tablet compaction can aid formulation design and selection of process parameters in powder compaction.

Chapter 4. Characterization methods for compaction and breakage

Incremental theory of plasticity has been successfully used to describe the deformation of powder-like materials. Several types of constitutive models based on incremental plasticity have been applied in the analysis of compaction of powder materials, such as the Drucker-Prager Cap (DPC) model. The DPC model is popularly used because it contains features that capture the powder behaviour, including densification and shear failure. Throughout this thesis, the DPC model is adopted and used as a basis for simulations. In this chapter, the calibration procedure of constitutive model and breakage of powder compacts are outlined.

4.1 Materials

Three classes of powder materials were selected for their specific compaction behaviour. The different powders used are illustrated below.

4.1.1 Distaloy AE

Distaloy AE (manufactured by Hoeganaes) without added lubricants is composed of iron with pre-diffused elements and mixed with graphite. The image of Distaloy AE powder was taken by Scanning Electron Microscope (SEM) as shown in Figure 4-1. The particle size is in the range of 45 μm and 150 μm . It has good flowability and the beneficial property of self lubrication. The apparent density is 3.04 Mg m^{-3} and the full density is 7.48 Mg m^{-3} according to the manufacturer's specifications. Typical applications using this material are structural high density, high strength automotive parts such as synchroniser hubs or cam belt wheels.

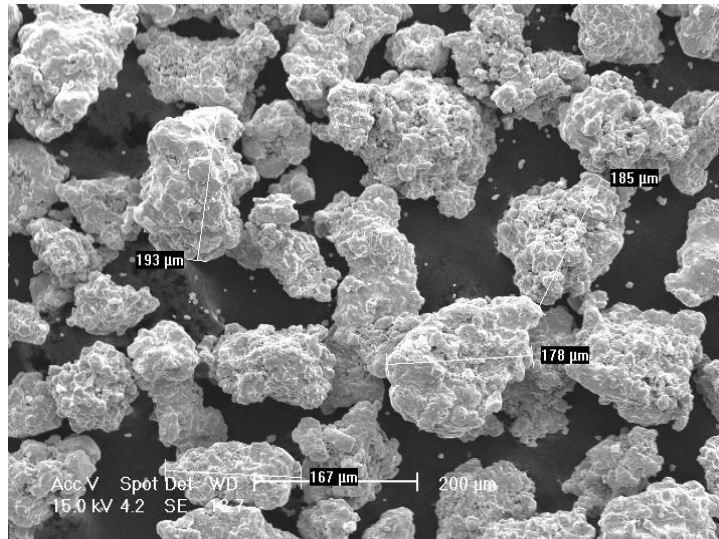


Figure 4-1 SEM image of Distaloy AE (From Sinka and Cocks, 2007)

4.1.2 Dibasic calcium phosphate

Dibasic calcium phosphate (Trade name A-Tab manufactured by Rhodia Pharma Solutions) is a commonly used powder in pharmaceutical tablet production due to its low cost and non-pharmacologically active property. A-Tab is classified as a ceramic powder. The surface of the particles is rough and the average particle diameter is approximately $180\mu\text{m}$. Figure 4-2 illustrates the appearance of the powder particles using SEM.

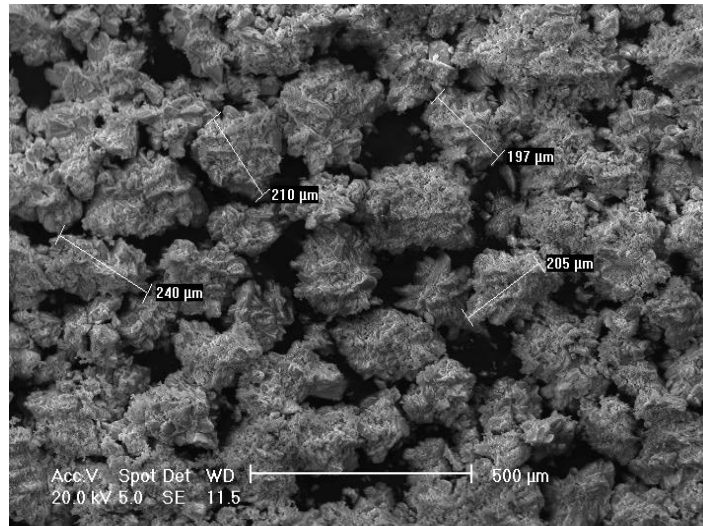


Figure 4-2 SEM image of A-Tab powder (from Galen, 2005)

4.1.3 Microcrystalline cellulose

Microcrystalline cellulose (MCC) grade Avicel PH102 (manufactured by FMC BioPolymer, Belgium) is used in this study. MCC is used widely in pharmaceutical formulations and this particular grade is designed for direct compression formulations. MCC particles are irregular, with a nominal particle size of 100 μm and size distribution between 20-200μm (Figure 4-3). The bulk and full density of the powder is 300 kgm⁻³ and 1590 kgm⁻³ respectively. The material is used in its pure form and as a result the strength of the tablet is significantly higher than when the tablet is made of practical formulations which contain the active pharmaceutical ingredient and other ingredients (particularly lubricants).

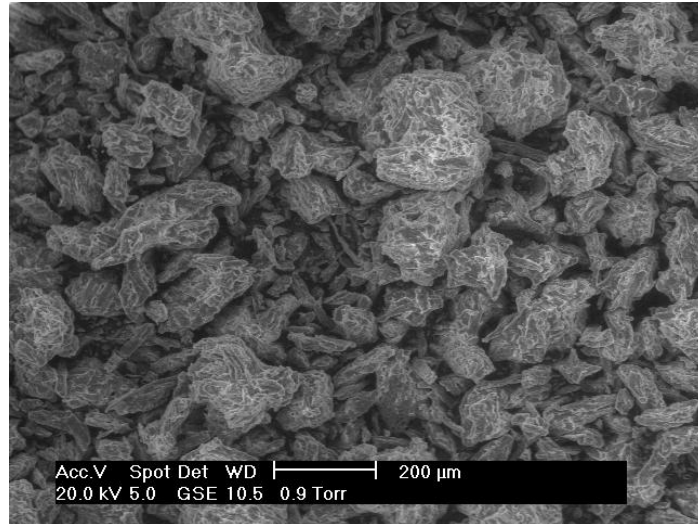


Figure 4-3 SEM image of MCC grade Avicel PH102 (from Sinka et al., 2003)

The powders used in different chapters are summarised as

- Distaloy AE (Chapter 4, 5, 6 and Chapter 7, Section 7.1)
- Dibasic calcium phosphate-A-Tab (Chapter 7, Section 7.2)
- MCC grade Avicel PH102 (Chapter 8 and 9)

4.2 Specimen manufacturing

Three types of specimens are made by powder die compaction to different density levels and subsequently tested, which are

- flat faced thin disks
- long cylindrical specimens
- curved faced tablets

The die is integrated into a MTS 810 materials testing system (manufactured by MTS, USA) as shown in Figure 4-4b and Figure 4-5b.

For diametrical compression tests, a series of thin disks were compressed using standard pharmaceutical tablet pressing tooling as shown Figure 4-4a.

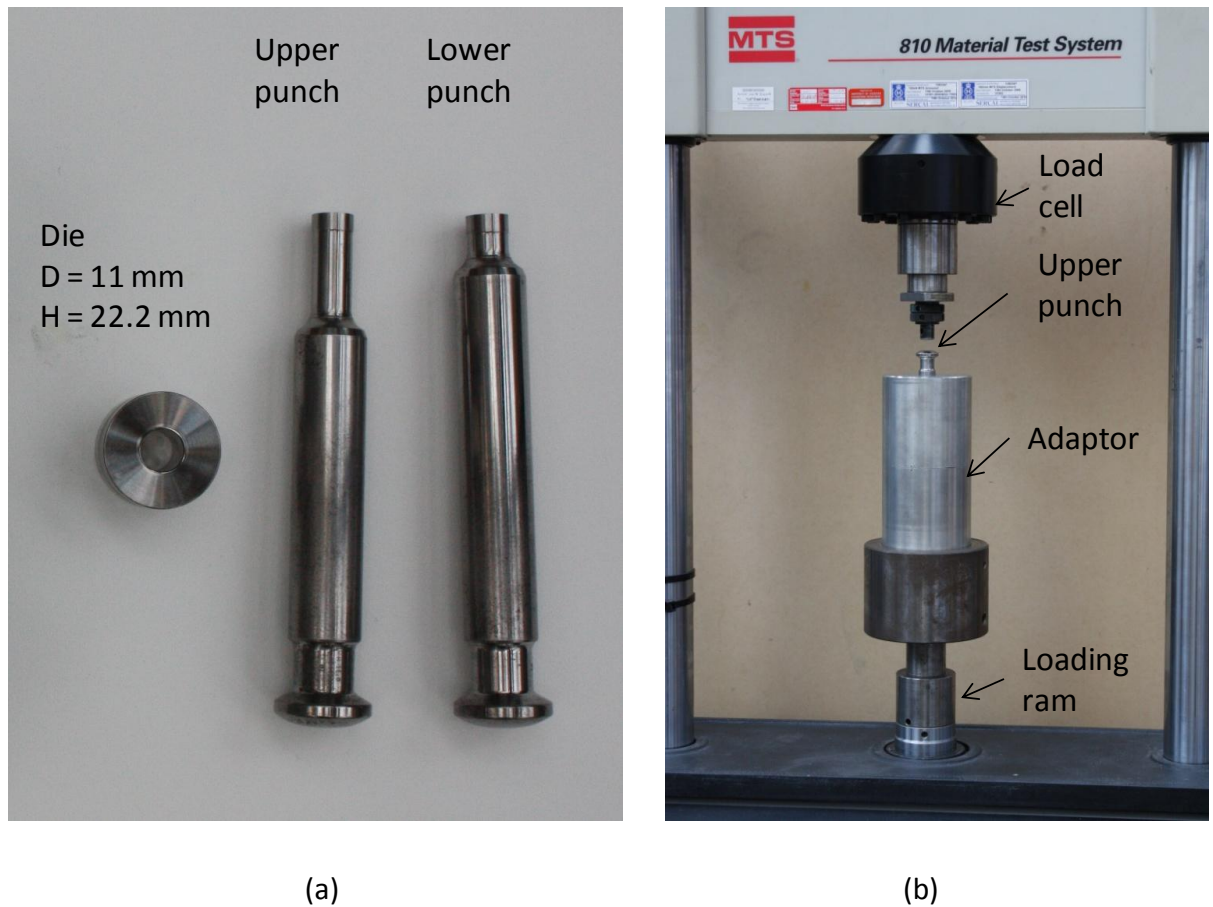


Figure 4-4 Closed die system for thin disks production a) Die and punches and b) system set-up

The influence of the sample diameter D , and the thickness t , on the failure stress was studied by Doremus et al. (2001). From this study, the specimen aspect ratio should maintain $t/D \leq 0.25$. Thus, the thickness of the disks used is less than 2.75 mm in order to ensure that the assumptions of the Hertz theory are maintained (e.g. thin disks made of linear elastic materials subject to point loading across the diameter).

The long cylindrical specimens for uniaxial compression testing were manufactured using a die with a tungsten carbide liner as shown in Figure 4-5a. In order to reduce

the end effects in uniaxial compression tests, the compressed specimen height was at least 25mm to achieve a minimum 2:1 (height to diameter) aspect ratio.

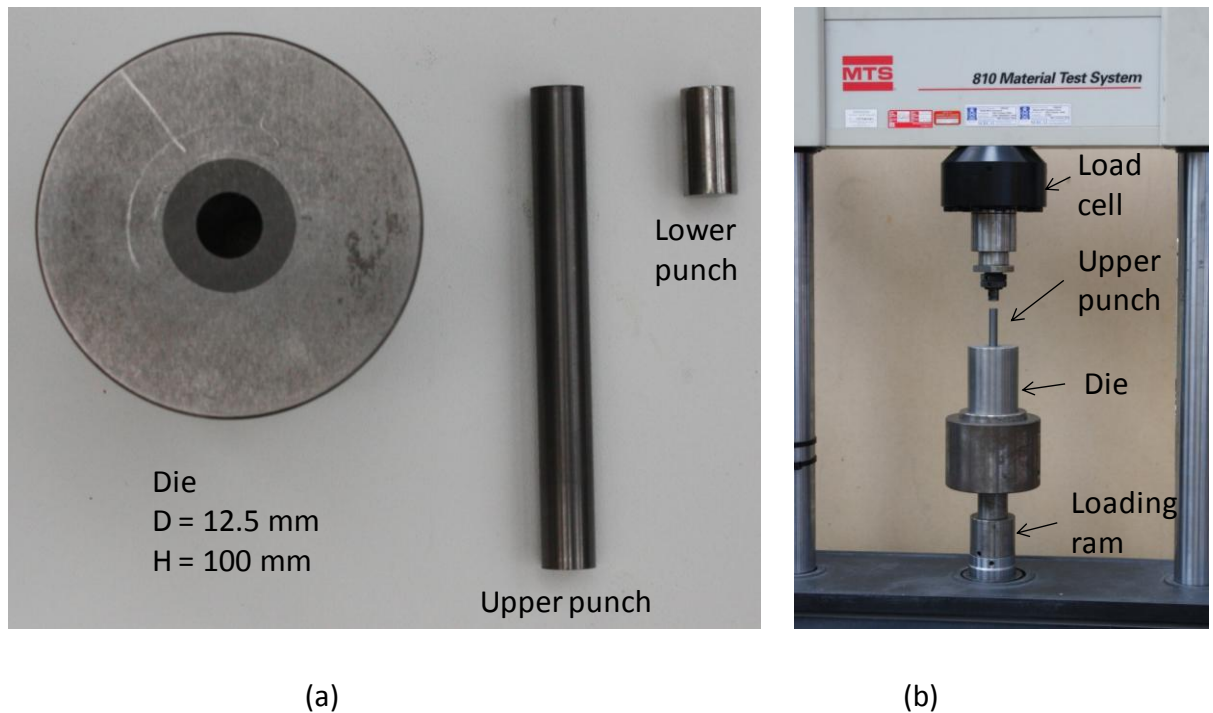


Figure 4-5 Closed die system for tall cylinder samples production a) Die and punches and b) system set-up

To manufacture curve faced tablet, powder was compressed in a closed die using a series of different curvature punches. The details of tablets manufactured are given in Chapter 8.

First, powder was filled into the die manually to achieve uniform packing density. The powder aggregate was then compacted by moving the loading ram up at a rate of 10 mm/min until a prescribed maximum upper punch force was reached while the cross head was fixed in its position. The unloading was controlled by moving the bottom ram at a rate of 1mm/min until complete unloading. Typical force displacement curve is

illustrated in Figure 4-6. Note that during compaction, only the force of the upper punch was measured. Specimens were then ejected from the die by removing the lower punch. In order to minimise the effect of friction between the powder and die wall, the die was pre-lubricated using magnesium stearate (manufactured by Mallinckrodt, UK).

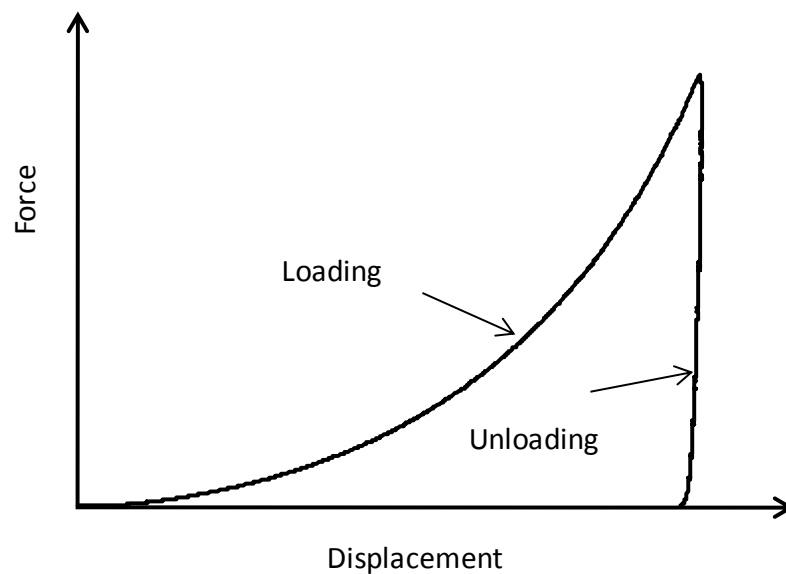


Figure 4-6 Typical force verse displacement curve during loading and unloading

4.3 Drucker-Prager Cap plasticity model

The DPC model is the most widely accepted model in powder metallurgy (Trasorras et al., 1998 and Zavaliangos, 2002 and PM Modnet Research Group, 2002), ceramics industry (Aydin et al., 1996 and Lee and Kim, 2007) and later pharmaceutical industry (Michrafy et al., 2002, Sinka et al., 2003, Wu et al., 2004, Sinha et al., 2010 and Han et al., 2011). It is an incremental plasticity model that is based on the existence of a yield

surface and a flow potential. In general a yield surface F' is a function of the stress invariants, material properties and state variables and is written as

$$F' = 0 \quad (4-1)$$

The direction of the plastic strain rate ($\dot{\varepsilon}_{ij}^p$) is determined by differentiating another function called flow potential G with respect to stress (σ_{ij})

$$\dot{\varepsilon}_{ij}^p = \dot{\lambda} \frac{\partial G}{\partial \sigma_{ij}} \quad (4-2)$$

where $\dot{\lambda}$ is a plastic multiplier.

The model is assumed to be isotropic and its yield surface includes mainly two parts: shear failure surface F_s and cap surface F_c . Shear failure surface provides dominantly shearing flow and reflects the dependence of the strength on the confining pressure. It provides that the strength in tension is smaller than that in compression, a concept that is common in rocks, brittle material and pressed powder compacts. In the simplest form, the shear failure surface (ABAQUS v6.7) can be identified by a straight line by two parameters: cohesion d and internal friction angle β :

$$F_s = q - p \tan\beta - d = 0 \quad (4-3)$$

The cap surface (ABAQUS v6.7) describes densification behaviour and is defined as:

$$F_c = \sqrt{(p - p_a)^2 + \frac{R^2 q^2}{\left(1 + \alpha - \frac{\alpha}{\cos\beta}\right)^2}} - R(d + p_a \tan\beta) = 0 \quad (4-4)$$

The parameters in equations (4-3) and (4-4) are defined as follows: Consider an axisymmetric powder body subject to axial stress σ_{ax} and radial stress σ_{rad} (such as closed

die compaction) as illustrated in Figure 4-7a. For this configuration, the von-Mises effective stress q and the hydrostatic stress p as defined in equation (2-1) and (2-2) becomes

$$p = \frac{1}{3}(\sigma_{ax} + 2\sigma_{rad}) \quad (4-5)$$

$$q = |\sigma_{ax} - \sigma_{rad}| \quad (4-6)$$

R defines the shape of the elliptic cap and p_a is an evolution parameter which is related to the hydrostatic yield stress p_b by the relationship shown in Figure 4-7b. α is a parameter describing a smooth transition region between the shear failure line and the cap surface. Furthermore, α is usually a small number between 0.01~0.05 in order to avoid the situation that $\alpha=0$ for which the interaction of the shear failure line and the cap surface will form a sharp corner, which may consequently lead to a numerical problem (Hibbitt et al., 1998).

The yield surface expands as the material densifies. The evolution of the yield surface is described by a hardening law p_b as a function of volumetric plastic strain ε_v^p . The density of the material ρ is a function of volumetric plastic strain, which enables ρ to be used as a convenient measure of the state of the material.

4.4 Parameter characterisation of the DPC Model

To identify the yield surface of the material, a number of experimental procedures can be used as illustrated in Figure 4-7. The procedures are labelled with numerals in p - q plane and discussed as follows. The failure in equation (4-3) can be obtained using (1) uniaxial tension tests, (2) shear cells, (3) diametrical compression, and (4) uniaxial compression tests. These are standard procedures for general purpose characterisation. In uniaxial compression, $q/p = 3$. Stress states with lower q/p ratio can be achieved using triaxial testing whereby a cylindrical sample (as illustrated in Figure 4-7, label 5) is subject to a radial confining pressure and a superimposed axial stress. The triaxial testing procedure was developed for rock and soil testing and adapted for powder compaction for over the last 4 decades (Koerner, 1971, Pavier and Doremus, 1999, Sinka et al., 2000, Schneider and Cocks, 2002.). In addition, Triaxial tests can also be conducted on cubical samples (Shima and Oyane, 1976). Triaxial testing involves specialist equipment which makes it possible to determine the cap surface in detail using confined triaxial tests (labelled 5A in Figure 4-7), simulated closed die compaction (5B) where the radial strain is maintained at zero, radial loading paths in stress space (5C) or isostatic compression (5D) tests. As described in the Section 2.2, triaxial testing can be used not only to calibrate a given constitutive model but also to probe the yield surface of a powder compacted to a given state along a given loading path (Schneider and Cocks, 2002).

For practical purposes, however, it is important to calibrate a constitutive model in a simple and efficient manner. A practical procedure for calibrating the Drucker-Prager

cap model is presented in Table 4-1 below and described in more detail in the following sections.

Table 4-1 Calibration of constitutive model parameters

Parameter	Description	Testing procedure
Plastic behaviour: Drucker-Prager cap model		
d , MPa	cohesion	uniaxial compression and diametrical compression test
β , degree	internal friction angle	
R	cap shape parameter	instrumented die compaction test, loading
p_b , MPa	hardening rule	
Elastic behaviour: Linear elasticity		
E , GPa	Young's modulus	instrumented die compaction test, unloading
ν ,	Poisson's ratio	

The calibration methods developed in this section are general and can be used for any powder material.

4.4.1 Characterization of the shear failure line

The shear failure line is defined by two points, which can be determined by two simple tests such as diametrical compression (to provide the tensile strength, see Figure 4-7, label 3) and uniaxial compression (see Figure 4-7, label 4).

These tests are carried out by using a series of specimens compacted to different densities in order to describe the strength parameters as functions of relative density.

The diametrical compression test provides the tensile strength which is determined from the break force F_d and specimen size (diameter D and thickness t)

$$\sigma_d = 2F_d/(\pi Dt) \quad (4-8)$$

Equation (4-8) was derived by Hertz (Timoshenko and Goodier, 1970). The stress state in the specimen is

$$p = \sigma_d/3, q = \sqrt{13}\sigma_d \quad (4-9)$$

The uniaxial strength σ_c is calculated from the break force F_u of uniaxial compression test and cross-sectional area of the specimen

$$\sigma_c = \frac{4F_u}{\pi D^2} \quad (4-10)$$

In the p - q plane the state of stress for uniaxial compression is

$$p = \sigma_c/3 \text{ and } q = \sigma_c \quad (4-11)$$

The cohesion d and internal friction angle β are determined from the above tensile and compressive tests as

$$d = \frac{\sigma_c \sigma_d (\sqrt{13} - 2)}{\sigma_c - 2\sigma_d} \text{ and } \tan \beta = \frac{3(\sigma_c - d)}{\sigma_c} \quad (4-12)$$

4.4.2 Characterization of the cap surface

The cap surface is calibrated using the axial and radial stresses that are measured using a die instrumented with radial stress sensors which is described in Chapter 5.

The loading path in effective-hydrostatic stress plane is shown in Figure 4-7. The loading point 'A' locates on the yield surface, for this point the strain increment direction is also known since in the closed die system the radial strain is restricted to

zero. Thus, the size and position of the cap ellipse can be obtained by solving the system equations that describe the yield condition and normality.

The hardening law is given by the hydrostatic compression yield stress p_b , which is a function of volumetric plastic strain ε_v^p

$$p_b = f(\varepsilon_v^p) \quad (4-13)$$

The volumetric strain can be expressed as

$$\varepsilon_v^p = \ln(RD/RD_0) \quad (4-14)$$

where RD is current relative density, RD_0 is the initial relative density of powder. The evolution parameter p_a is given as

$$p_a = \frac{p_b - Rd}{(1 + R \tan \beta)} \quad (4-15)$$

Considering the associated flow rule on the cap, inelastic strain rate can be expressed

$$\dot{\varepsilon}_{ij}^p = \dot{\lambda} \frac{\partial F_c}{\partial \sigma_{ij}} \quad (4-16)$$

where $\dot{\lambda}$ is a positive scalar denoting the magnitude of the plastic deformation, $\frac{\partial F_c}{\partial \sigma_{ij}}$

denotes the direction of the plastic flow.

In instrumented die compaction at point A (Figure 4-7) where the loading path interacts with the cap surface we have

$$F_c(p_A, q_A) = 0 \quad (4-17)$$

Assume that die wall is rigid body, the radial plastic strain rate can be written as

$$\dot{\varepsilon}_{rad}^p = \dot{\lambda} \frac{\partial F_c}{\partial \sigma_{rad}} \Big|_{(p_A, q_A)} = 0 \quad (4-18)$$

Since $\dot{\lambda}$ is positive, then

$$\frac{\partial F_c}{\partial \sigma_{rad}} \Big|_{(p_A, q_A)} = 0 \quad (4-19)$$

Thus, the parameter p_a and cap eccentricity parameter R can be obtained using equation (4-4) and (4-15)

$$R = \frac{1}{3} \sqrt{6} \sqrt{\frac{(1 + \alpha - \frac{\alpha}{\cos(\beta)})^2 (p - p_a)}{q}} \quad (4-20)$$

$$p_a = \frac{-3q - 4d \tan(\beta)(1 + \alpha - \alpha / \cos \beta)^2}{4 \tan(\beta)^2 (1 + \alpha - \alpha / \cos \beta)^2} + \frac{\sqrt{9q^2 + 24dq(1 + \alpha - \alpha / \cos \beta)^2 \tan(\beta) + 8(3pq + 2q^2)(1 + \alpha - \alpha / \cos \beta)^2 \tan(\beta)^2}}{4 \tan(\beta)^2 (1 + \alpha - \alpha / \cos \beta)^2} \quad (4-21)$$

4.4.3 Characterization of elastic properties

In order to understand the unloading and ejection behaviour of the compacted component, the elastic properties (Young's modulus, E and Poisson's ratio, ν) of the compact need to be characterized. These parameters can be obtained using the stress-strain response of the powder during unloading in the die (Gethin et al., 1994; Sinka et al., 2003; Wu et al., 2005; Han et al., 2008). During unloading, the stress and strain are assumed linear elastic. This is considered a reasonable assumption (Oliver, 1992).

The Young's modulus E and Poisson's ratio ν are related to the bulk modulus K and shear modulus G

$$G = \frac{E}{2(1 + \nu)} \quad (4-22)$$

$$K = \frac{E}{3(1 - 2\nu)} \quad (4-23)$$

In elastic range, the behaviour of isotropic material is governed by the incremental Hooke's law

$$d\varepsilon_{ij}^e = \frac{dI_1}{9K} \delta_{ij} + \frac{ds_{ij}}{2G} \quad (4-24)$$

where I_1 is the first stress invariant, $d\varepsilon_{ij}^e$ is the elastic strain increment, $s_{ij} = \sigma_{ij} - \left(\frac{I_1}{3}\right) \delta_{ij}$ is the deviatoric stress tensor, and δ_{ij} is the Kronecker delta.

Thus, we have

$$d\varepsilon_{ax} = \frac{d\sigma_{ax} + 2d\sigma_{rad}}{3K} = \frac{dI_1}{3K} = \frac{dp}{K} \quad (4-25)$$

$$d\varepsilon_{ax} = \frac{d\sigma_{ax} - d\sigma_{rad}}{2G} = \frac{dq}{2G} \quad (4-26)$$

For closed die compaction test, the strain increment and elastic strain increment during unloading stage may be expressed as

$$d\sigma_{ax} = \left(K + \frac{3}{4}G\right)d\varepsilon_{ax} \quad (4-27)$$

and the axial stress increment and radial stress increment relation may be written as

$$d\sigma_{ax} = \frac{3K + 4G}{3K - 2G} d\sigma_{rad} \quad (4-28)$$

From equation (4-27) and (4-28), we can obtain axial stress/axial strain and axial stress/radial stress relationships

$$d\sigma_{ax} = \frac{E(1 - \nu)}{(1 + \nu)(1 - 2\nu)} d\varepsilon_{ax} \quad (4-29)$$

$$d\sigma_{ax} = \frac{(1 - \nu)}{\nu} d\sigma_{rad} \quad (4-30)$$

As shown in Figure 4-8 , by determining the linear unloading slopes of axial stress-axial strain and axial stress-radial stress curves, it is straight-forward to identify the Young's modulus, E and Poisson's ratio, ν for a certain density of powder compact.

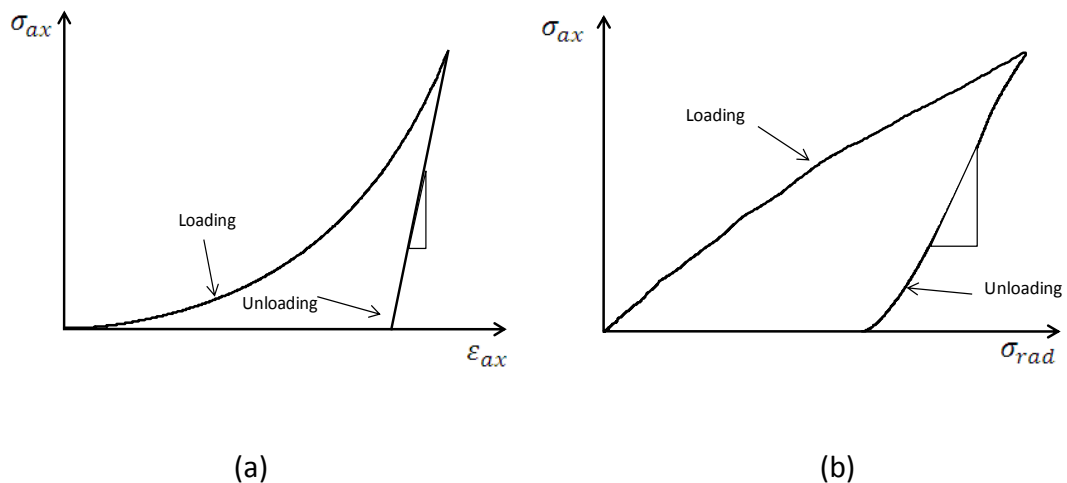


Figure 4-8 A method to determine elastic properties from unloading slope a) axial stress-axial strain curve and b) axial stress-radial stress curve

4.5 Strength measurement

Specimens were tested using diametrical (thin disks and curved faced tablets) and uniaxial compression (long cylinders) testing. Specimens were placed in between two platens mounted to testing machine. The top platen remained stationary, while the bottom ram moved upwards at a loading rate of 1mm/min (diametrical compression test) and 10mm/min (uniaxial compression test) until specimen failed (see Figure 4-9). The maximum loading force was taken as the break force of the specimen. Note that in Figure 4-9, photos of the failure of the specimens were taken after the break forces were reached, and they are only for the purpose of illustrating the tests. More precise implementation (i.e. high speed video camera) is required to identify the images of the specimens at the moment when the break force is reached (Procopio et al., 2003, Jonsen et al., 2007 and Mates et al., 2008).

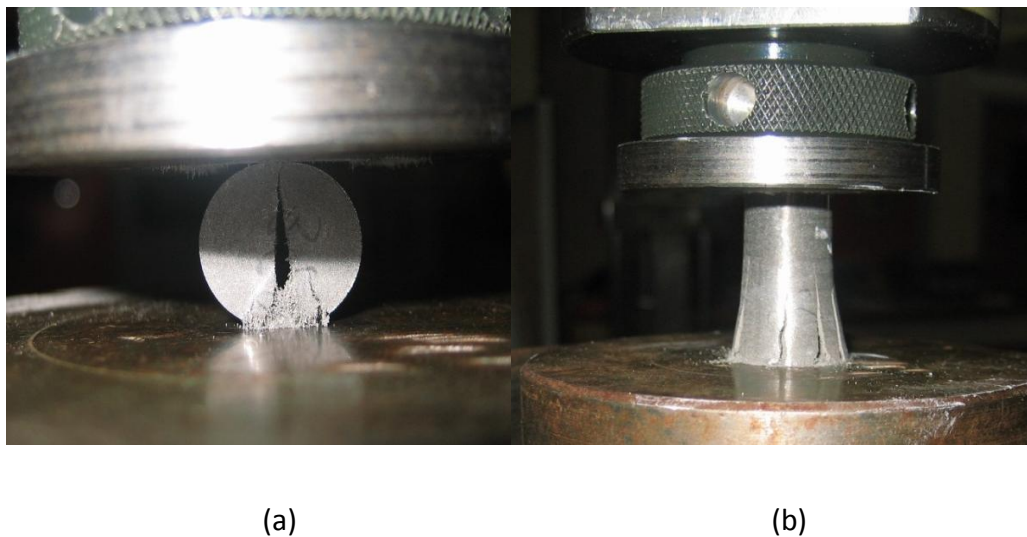


Figure 4-9 Images of a) Diametrical compression test and b) Uniaxial compression test

The details of the specimens tested for diametrical and uniaxial compression test are illustrated in Table 4-2 and Table 4-3 respectively. Repeats for both tests are provided

in Appendix A (Table A.1 and A.2) which suggest that the results can be replicated. The tensile and compressive strength of the specimen are obtained according to equation (4-8) and equation (4-10), respectively. The relative density range of the samples used in the two types of tests is from 0.56 to 0.9.

The tensile strength and compressive strength of the material as functions of relative density are presented in Figure 4-10. It can be observed that the compressive strength is always larger than tensile strength for all levels of relative densities. This is consistent with the fact that the shear failure line of the DPC model has a positive slope.

Table 4-2 Characteristics of tablets used for diametrical compression tests

Weight, g	Thickness, mm	Diameter, mm	Relative density	Break force, N	Tensile strength, MPa
1.457	3.167	11.003	0.647	44	0.80
1.394	2.923	11.002	0.671	72	1.43
1.223	2.337	11	0.736	118	2.92
1.343	2.409	11.004	0.784	240	5.77
1.268	2.159	11.002	0.826	294	7.88
1.411	2.327	11	0.853	415	10.32
1.258	2.027	11.004	0.873	448	12.79
1.254	1.969	11.004	0.896	529	15.55

Table 4-3 Characteristics of tablets used for uniaxial compression tests

Weight, g	Height, mm	Diameter, mm	Relative density	Break force, N	Compressive strength, MPa
18.001	33.9	12.541	0.578	1393	11.35
18.017	31.84	12.544	0.616	2816	22.95
17.857	29.88	12.544	0.651	4705	38.34
18.253	28.2	12.541	0.705	8031	65.44
18.055	26.32	12.543	0.747	11193	91.21
18.031	25.1	12.541	0.783	14924	121.61
18.942	25.8	12.54	0.800	15998	130.36
18.996	25.14	12.546	0.823	18395	149.90
19.003	24.46	12.546	0.846	21493	175.14

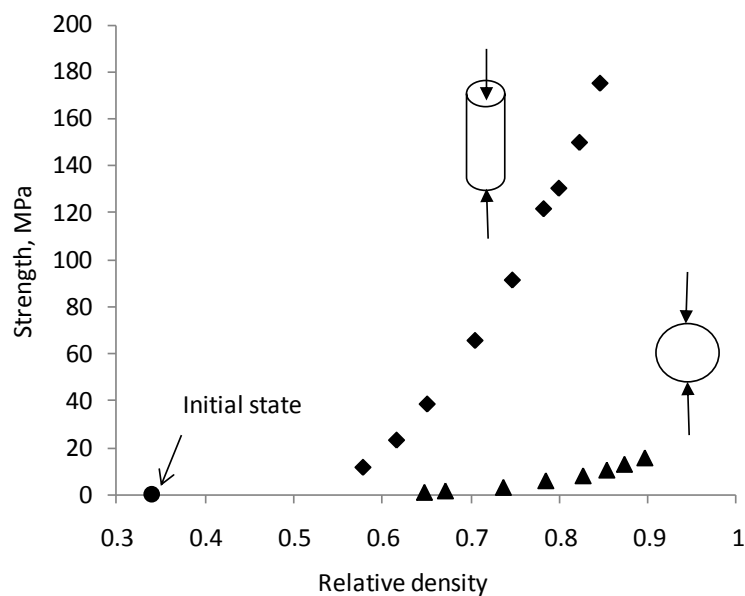


Figure 4-10 Tensile and compressive strength as functions of relative density

The cohesion d and internal friction angle β as functions of relative density are illustrated in Figure 4-11. It can be observed that the cohesion increases as the

material densifies, while the internal friction angle decreases linearly and has an approximate value of 70 degree.

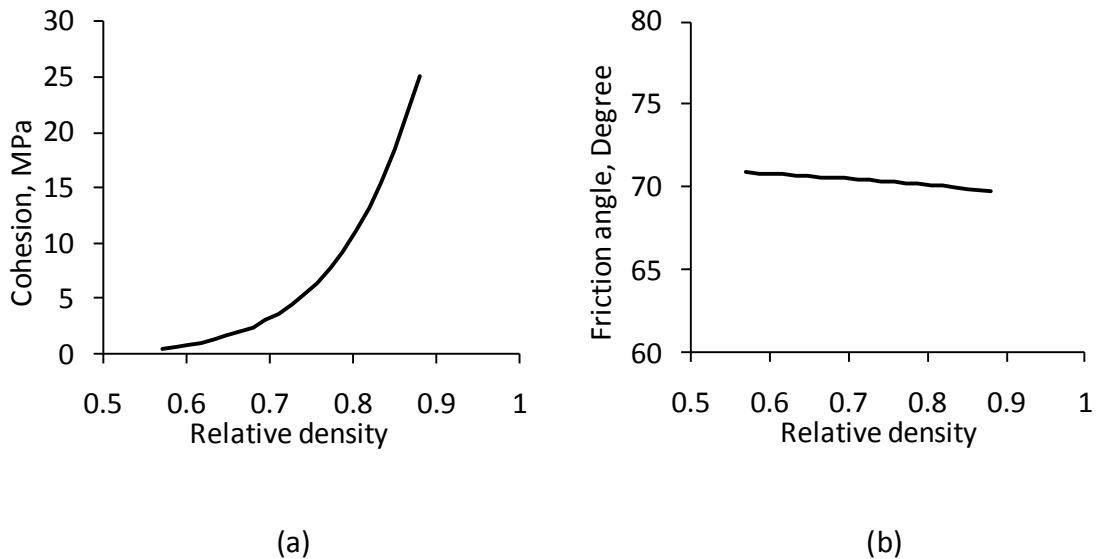


Figure 4-11 Shear failure line parameters, a) cohesion, b) internal friction angle

4.6 Summary

The calibration procedure of DPC model for exterminating the elastic and plastic material parameters, E , ν , d , β , R and p_b are established through a series of mechanical tests, such as diametrical compression, uniaxial compression and closed die compaction experiments. Material parameters can be described as a function of a state variable, RD , which evolves as the powder is densifying from loose state to solid state. Each yield surface is composed of a shear failure and elliptical cap surface of DPC model. Fully calibrated DPC model, in which the material parameters evolve with density, is considered more appropriate than that of constant material parameters which is often applied, especially to simulate the unloading behaviour of powder compact and to predict the material strength at different densities. The experiments

and model calibration are based on Distaloy AE powder, however, those experiment and calibration procedures can be applied to any powder in general.

The experimental details of manufacturing and testing the samples are provided for diametrical and uniaxial compression tests. The result of calibrated shear failure which is independent of the cap surface is presented and can be readily used to calibrate the cap surface.

In the following chapter, the instrumented die system and the experiment procedure are introduced in detail.

Chapter 5. Instrumented die system

Die compaction is a key procedure that can be used to characterise the compaction behaviour of powders and to manufacture powder compacts for subsequent testing, e.g. mechanical strength testing, characterisation of density distributions etc. In this chapter the closed die system is studied and the necessary instrumentation is described in order to develop a suitable material characterization procedure for powder compaction. The aim of this part of the research is to generate experimental inputs (e.g. stress-strain relation) for modelling (e.g. the constitutive model and die friction).

5.1 Closed die system

Closed die compaction is the most representative test for studying powder densification phenomena or compressibility (Heckel, 1961). In general, the axial stress is determined by measuring the axial force, while the density or porosity is determined by measuring the tablet volume and mass. The advantages of a closed die system is that it has simple structure, the top force and/or bottom force and displacement are measured and powder densification is achieved in a similar manner as in industrial production. However, die compaction also has the following disadvantages for various closed die system configurations

If the system consists of only one force (top or bottom force) measurement device then the stress strain relation that is derived incorporates the effect of friction. Thus, if one force is measured, the friction effect should be minimized. Three closed die systems are used In order to illustrate the drawbacks of a closed die system that has only the possibility to measure the force and displacement of top punch. The

diameters of the three dies are: 10.5mm, 11mm, and 12.5mm. Figure 5-1 shows relative density versus the maximum compaction pressure for the die systems.

Because of friction between the powder and die wall for each maximum compaction pressure the average density of the specimen varies. Thus, the influence of the friction effect on the stress-strain relationship cannot be identified. The three dies may present different surface finishes which affect friction.

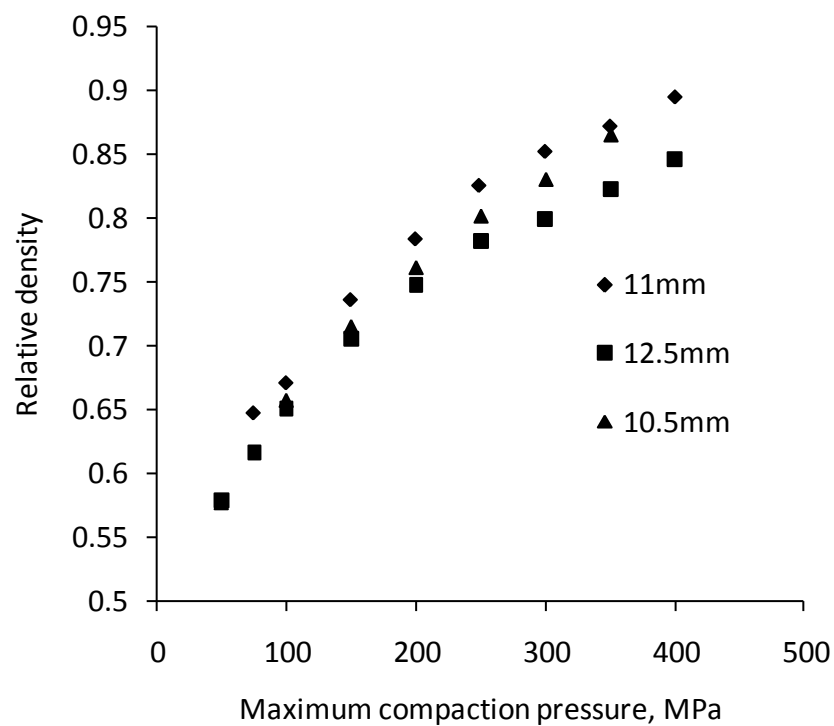


Figure 5-1 Average relative density as a function of the maximum compaction pressure for Distaloy AE powder using three dies with different diameters.

For a given die the height to diameter aspect ratio of the specimen will also play a role and the taller the specimen the larger the density variations induced along the height of the compact.

If both top and bottom forces are measured then friction effect can be taken into account and the compaction pressure estimation is more accurate. However, this approach ignores the radial stress transmission so it is incapable of characterising 3D stress states. This issue has been recognized in industry (Trasorras et al., 1998). In addition, the friction between powder and die wall introduces density inhomogeneity which have not been accounted for so far.

Thus there is a need for radial stress measurements. The radial stress can be determined in a number of ways. For example, strain gauges can be mounted on the external surface of the die and the radial stress can be determined from hoop strain measurements (Mauricio and Sanchez, 2008 and Hong et al., 2008). The radial stress can also be measured directly using pressure sensors placed in the die in contact with the powder; this is referred to as instrumented die system. This system allows the measurement of stress state under both loading and unloading stages. Not only the stress-strain relation is obtained, but also the elastic properties of the green compact can be determined from unloading stage of the experiment. In addition the coefficient of friction between powder and die wall can be calculated.

5.2 Instrumented die system

A number of publications using instrumented die systems can be found in the literature (Ernst et al., 1991, Gethin et al., 1994 and Guyoncourt et al., 2001). The instrumented die set-up is illustrated in Figure 5-2. During compaction, the radial strain is zero if the elastic deformation of the die is neglected. The axial strain is determined by measuring the displacement of the top and bottom punches. The axial stress is determined by measuring the forces applied by the punches.

The die instrumented with radial stress sensors is presented in Figure 5-2b). The diameter of the die is 10.5 mm and two pressure sensors (manufactured by Kistler Instruments) are placed at 10 and 12 mm from the top of the die. The sensors are round with a diameter of 1 mm. The material of the die, the tolerances, and the surface finish correspond to dies used on high speed pharmaceutical tablet presses.

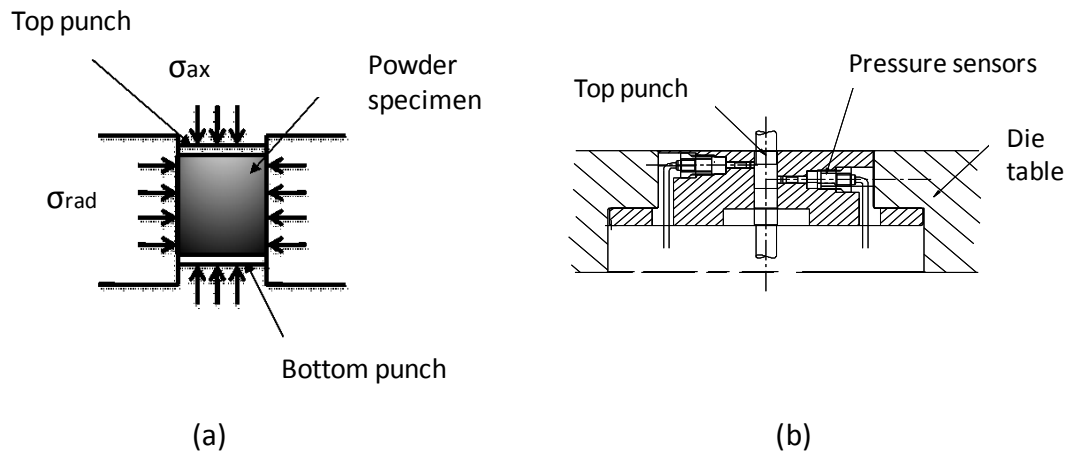


Figure 5-2 Closed die compaction a) stress states, b) die instrumented with radial stress sensors

The instrumented die is integrated into a MTS 810 materials testing system as illustrated in Figure 5-3. The maximum radial stress measured by the sensors is 200 MPa. The maximum axial load that can be applied by the system is 100 kN. Therefore in a typical experiment the axial load is limited so that the capacity of the radial stress sensors is not exceeded.

In this configuration the die is fixed, the bottom punch is stationary and compaction is applied using the top punch. Due to the effect of the friction, the force applied by the

top punch is always higher than the force transmitted to the bottom punch. The two punch forces are measured using load cells as illustrated in Figure 5-3.

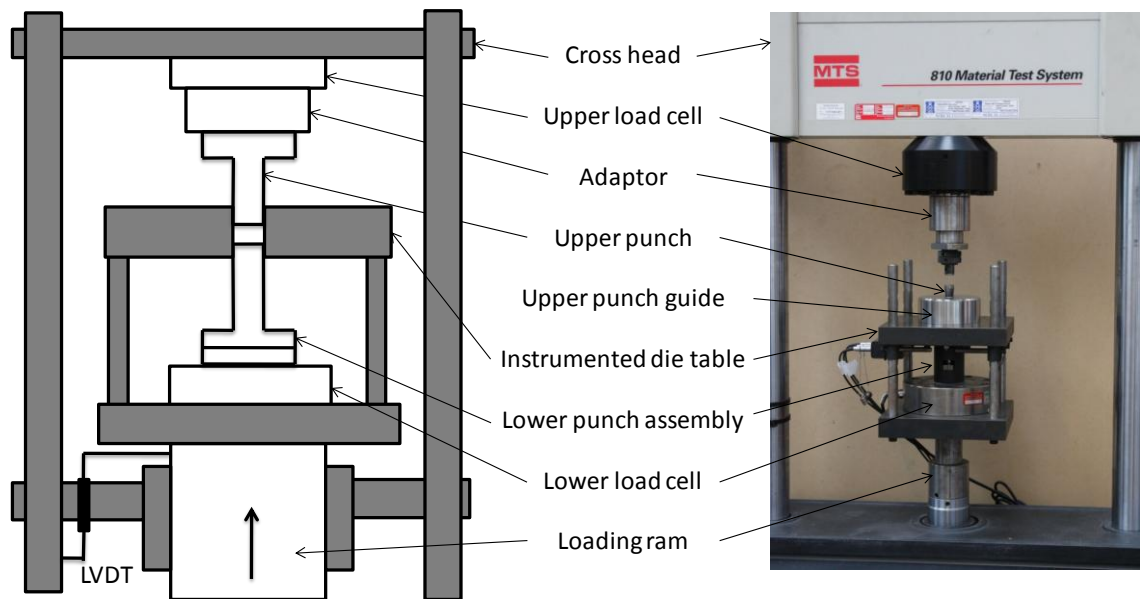


Figure 5-3 Instrumented die set-up (from Shang et al., 2011)

The initial fill height of the powder in the die is 13.5 mm. The powder is filled into the die carefully by hand to achieve a uniform packing. The top surface of the powder is made level with the die using a scraper. Compression and unloading are carried out by controlling the movement of the top punch. To eject the tablet, the lower punch is removed and the tablet is ejected through the bottom opening of the die using the top punch. The compression and ejection rates are set at 10 mm/min and unloading rate is at 1 mm/min.

Before the experiment, a zero position of the system is set up when the top punch is precisely at the top of the die. This is set after a small load is applied to a calibrated spacer placed over the die table. In order to reduce the effect of friction, the die is pre-

lubricated with magnesium stearate. The displacement of the top punch is determined from measuring the displacement of the cross-head using a linear variable differential transformer (LVDT) which is part of the MTS testing machine. The axial strain is determined from displacement using the logarithmic definition of strain. The compression forces in N and displacement in mm of the moving platen are recorded during the test.

The following parameters are measured during loading and unloading

- Displacement d_T of top punch
- Forces at top F_T and bottom F_B punch
- Radial stress at top sensor σ_{r_T} and bottom sensor σ_{r_B}

The stress at top and bottom are calculated: $\sigma_T = \frac{F_T}{A}$, $\sigma_B = \frac{F_B}{A}$ where $A = \pi D^2/4$ is the cross sectional area of the die.

5.3 Experimental results using the instrumented die

The direct measurement of forces or stresses of the instrumented die is presented as follows using Distaloy AE (see Section 4.1.1) as example powder material. The axial and radial stress at the loading stage are plotted against top punch displacement as shown in Figure 5-4. The maximum compaction pressure reaches 350MPa at top punch. As can be seen, the axial stress at top punch σ_T (moving punch) is always higher than that at bottom punch σ_B . Similarly, the radial stress at top sensor σ_{r_T} is always larger than radial stress at bottom sensor σ_{r_B} . This suggests that there exist a stress gradient from top to bottom punch. The bottom pressure follows the same trend as the top pressure but its magnitude is about 10% less than the latter in the

present experiment. This is because of the friction between the powder and die wall which can be reduced by pre-lubrication of the die, although it cannot be completely eliminated. However, the powder compacts are assumed homogeneous along the axis, especially when the die is lubricated (Doelker and Massuelle, 2004). The result provided in Figure 5-4 is the direct measurement of the pressure and displacement of the top punch which will be further processed to generate the constitutive law of material.

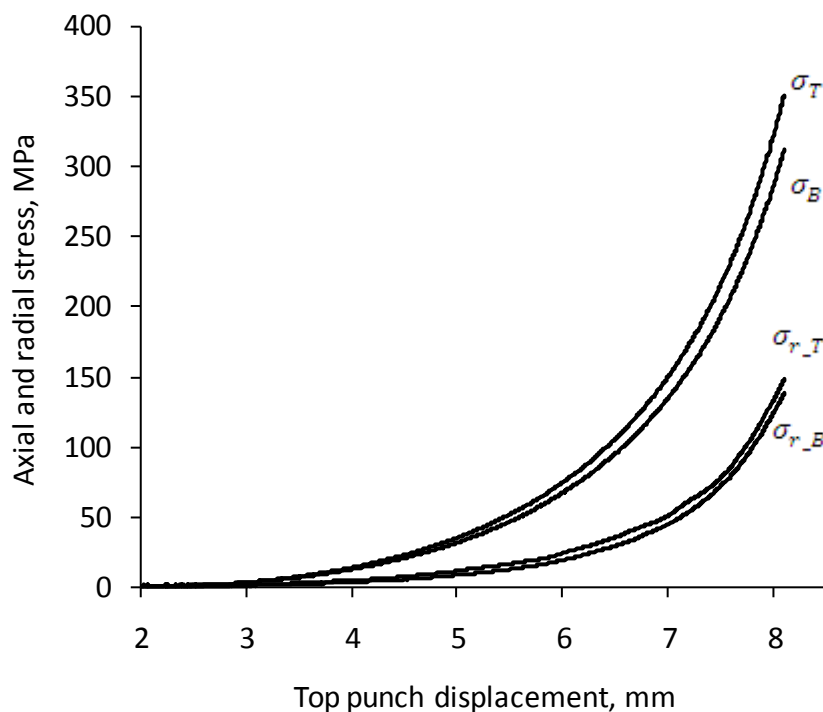


Figure 5-4 Stress displacement curve during die compaction

At unloading stage, the axial stress is plotted against displacement in Figure 5-5. Figure 5-5(a) shows that σ_T is still larger than σ_B at the beginning of the unloading stage until the moment (displacement=8.43mm) when $\sigma_T = \sigma_B$. After that, σ_T is smaller than σ_B

until the end of the unloading. Figure 5-5(b) shows that at the end of unloading (displacement=8.06mm) σ_T decreases to zero, while σ_B remains at around 2MPa. This is because of the residual radial stress and friction along the die wall which restricts the relaxation of the specimen in the die.

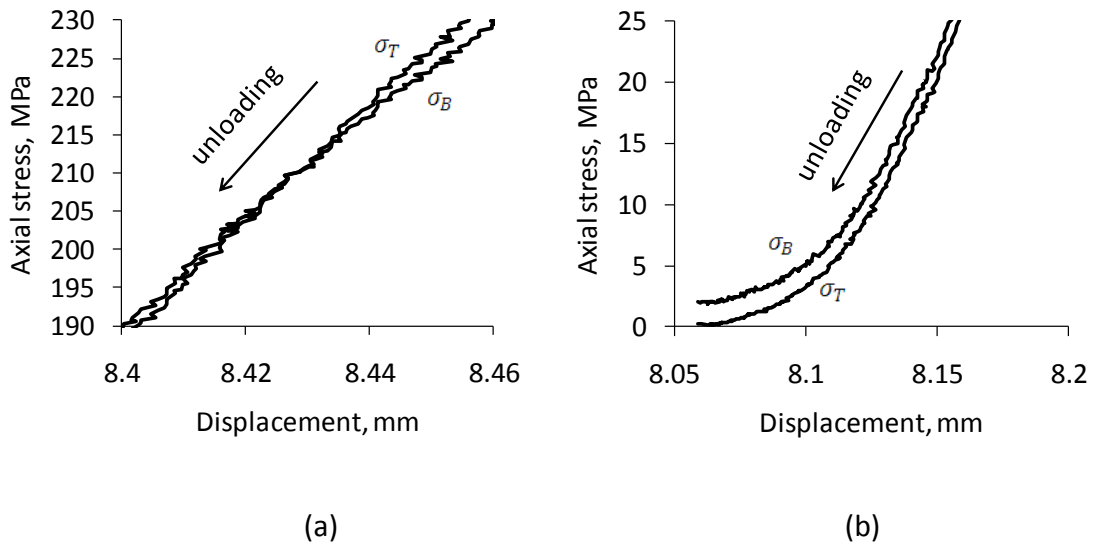


Figure 5-5 Axial stress at top and bottom punch during unloading stage a) the transition phase when axial stress at top equals to axial stress at bottom. b) the residual axial stress of top and bottom punch after unloading

Friction between die wall and powder compact depends on the characteristics of the powder, die material and the surface finish of the die. Coulomb's law is used to describe friction behaviour

$$\tau = \mu\sigma \quad (5-1)$$

The friction at the die wall is calculated indirectly by measuring the top punch force and bottom force $f = F_T - F_B$. Brisco (1998) defines transmission ratio as

$$TR = \frac{\sigma_B}{\sigma_T} = \frac{F_B}{F_T} \quad (5-2)$$

The transmission ratio is used to account for the friction effect on the compaction during compaction. Ideally, if no friction exists, $TR=1$. Under such condition, specimen is perfectly homogenous. However, in practice, the friction can only be minimized but not eliminated. Thus, if TR is too low (e.g. $TR=0.6$), the friction effect will induce a significant stress gradient within the specimen. Subsequently, the specimen exhibits a non-homogenous material. In the present case of Distaloy AE powder using instrumented die, $TR=0.9$.

5.4 Summary

We have discussed three closed die system configurations and proposed the use of instrumented die system. The primary outputs using instrument die are presented. The reason of using this system is to be able to obtain the necessary information to generate a stress-strain relation. The displacement measurement includes the elastic deformation of the testing system. The details for correcting for the elastic compliance of the system are presented in Chapter 6.

Chapter 6. Instrumented die data extraction method and model calibration

6.1 Introduction

The data processing and constitutive model parameter extraction procedures are essential for accurate modelling as even slight deviations in these measurements can induce significant errors. Many factors, including friction and system compliance influence model calibration. Among them, friction effect on the powder material is a key consideration for a closed die compaction. In this chapter the data extraction method for model calibration is presented in detail.

The pharmaceutical research and development powder compressibility is measured using specialist systems called compaction simulators. These instruments consist of two high speed servo-hydraulic systems to generate programmable top and bottom punch motions. The instrumentation includes force and displacement measurements for both top and bottom punches and dies instrumented with radial stress sensors. Because of the instrumentation the compaction simulator is well suited to generate material property data for material models (Cunningham, 2004). Sinka and co-workers (2003) have demonstrated that a compaction simulator can be used to characterize constitutive model parameters for powder compaction. For example, in DPC model, material parameters, such cohesion, friction angle, cap eccentricity parameter, and hydrostatic yield stress can be expressed as a function of volumetric plastic strain. Young's modulus, Poisson's ratio can also be expressed as functions of relative density.

These parameters can be input into finite element modelling software to simulate different compression conditions.

One of the challenging aspects of using an instrumented die system is its proper calibration. The calibration procedure mainly includes the calibration of radial stress sensors, displacement transducer and system compliance. In theory, a perfectly hydrostatic media applies equal stress to both the punches and the die wall during compaction. In order to achieve a similar behaviour an incompressible elastic material (e.g., rubber plugs) is used to calibrate the instrumented die as they generally transmit equal pressure to the punch and the die wall. As long as the stress sensors are not overloaded their calibration is robust. In order to cover a wide range of powder material, the use of multiple radial sensors are essential (Cocolas and Lordi, 1993). The displacement traducers (LVDTs) must also be calibrated carefully. Typically, the calibration for load cell and LVDTs are conducted once or twice annually.

Proper correction for machine and punch deformation is vital for measuring the volume change of the powder compact. The punch and die system is not rigid.

Neglecting the deformation of the system will create an error in punch displacement measurement. The system compliance depends on several factors, such as machine rigidity, punch type, connections of screw thread to cross-head, alignment, etc. The details of the system compliance influence on the determination of material model are discussed in this chapter.

Due to the existence of friction, the uneven stress distribution within the compact is inevitable. When the compaction pressure reaches a certain level defects (e.g. crack, lamination) will occur and the material can no longer be described as homogeneous.

However, if powder compacts can be treated as isotropic during loading, the friction effect can be minimized.

A number of papers have presented results obtained using instrumented dies of various designs (Guyoncourt et al., 2001; Wu et al., 2005; Bier et al., 2007 and Han et al., 2008). However, the literature does not discuss correction methods for the elastic compliance of the testing systems.

The calibration of the cap surface requires an accurate stress-strain curve, which is generated using the instrumented die. So far the axial strain was calculated from the specimen height as

$$\varepsilon_{ax} = -\ln (H/H_0) \quad (6-1)$$

where H is the current height of the specimen determined from the displacement of the top punch and various compliance correction methods; and H_0 is the fill height. Compression is considered positive.

As any mechanical testing system, measurements errors inevitably exist. The forces applied by the top and bottom punches are measured with the accuracy of the load cells, which for the present set-up is 0.01% full scale. The measurement of strain involves a number of difficulties including

1. elastic compliance of the loading frame
2. non-homogeneous stress and strain states in the specimen

In the following, the importance of the system compliance for generating an accurate stress-strain curve for compression is discussed. The system compliance becomes

more significant during unloading stage at which the elastic properties are determined. A compliance correction method is then introduced following a detailed analysis of the forces and deformations of different parts of the loading frame.

The discussion in this chapter is made using Distaloy AE (see Section 4.1.1) powder material as example.

6.2 Elastic compliance of the testing frame

A typical mechanical testing machine is made of steel. The strain is typically determined by a displacement measurement. In many applications it is possible to clip an extensometer to the test section of the specimen or to use non-contact devices that measure only the deformation of the specimen. In the instrumented die, however, the specimen cannot be accessed directly. The punch displacement includes the deformation of the specimen and the elastic compliance of various elements of the testing frame, such as punches, load cells, etc. While it is possible to mount the displacement transducers more optimally (e.g. attached to the punches) thus eliminating the contribution to elastic compliance from some of the components, it will be shown below that the punch deformation is still significant even if the so-called “stiff” testing frames are used. Therefore corrections for elastic compliance are necessary to generate an accurate stress strain curve.

The stiffness of a material testing machine, measured in (kN/mm), is usually supplied in the technical specifications of the machine. For example, the MTS system used in this work has a quoted stiffness of 260 kN/mm which corresponds to a compliance of 0.00384 mm/kN. The quoted values, however, usually exclude fixings, additional load cells etc. In practice, the force-displacement response of the testing frame shows an

initial non-linear part which is due to the elastic follow up of the loading train (Dean et al., 1995). Testing standards (e.g. ASTM E111) specify pre-loading to eliminate the initial setting and non-linearity. For these situations, it is possible to apply linear correction for the elastic deformation of the testing machine. The non-linear response of testing machines is also well documented. Kalidindi et al., (1997) presented a method accounting for non-linear system compliance for compression testing. This approach is followed for the instrumented die set-up presented in Figure 4-1. In addition, a specific compliance correction procedure unloading in the instrumented die is developed.

The loading system comprises of a number of mechanical components. The compliance of the system is determined by pressing together the top and bottom punches (see Figure 5-4) without any powder. The force-displacement relationship for the system during loading and unloading is presented in Figure 6-1. It can be observed that the curve is non-linear during early stages and becomes linear at higher loads. There is a small difference between the loading and unloading curve, which is assumed due to the initial settling of the components which may result from the imperfect connection between components.

When a powder specimen is compressed the deformation that is measured includes the deformation of the powder and the elastic deformation of the system. Figure 6-2 shows a typical force-displacement curve for Distaloy AE powder. The deformation of the powder is obtained by subtracting the elastic deformation of the system from this curve. This correction for the system compliance can be done using two correction methods

- linear, based on the final part of the curve in Figure 6-1
- non-linear, based on the complete curve in Figure 6-1

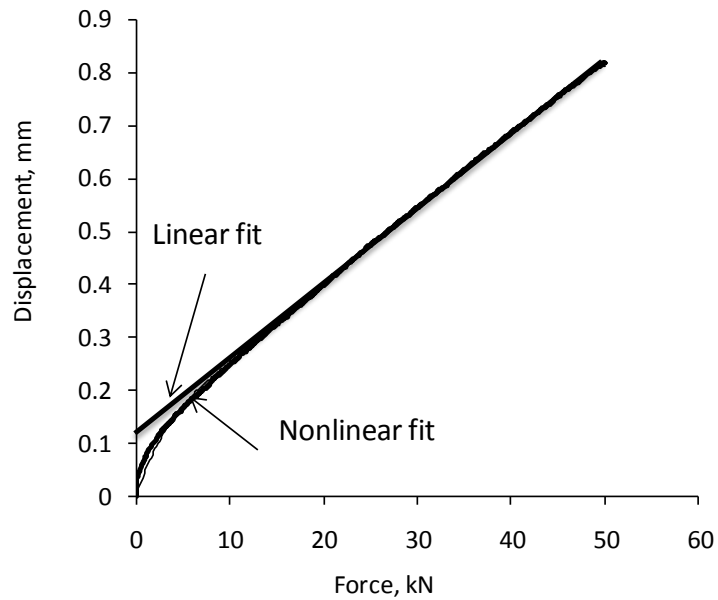


Figure 6-1 Compliance curve of the instrumented die system

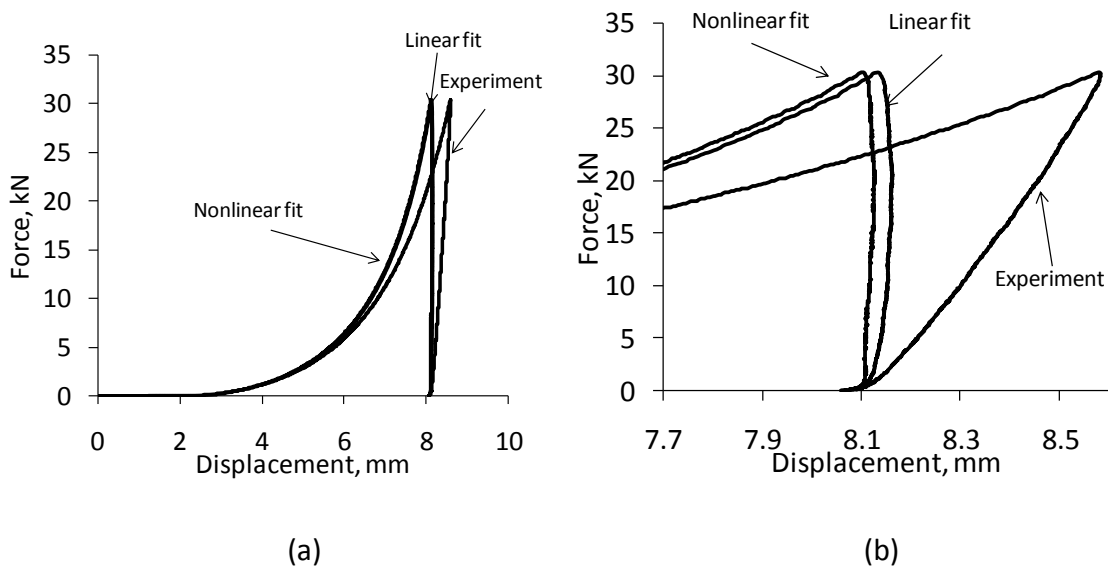


Figure 6-2 Force-displacement behaviour of the powder material together with corrections using linear and non-linear system compliance, a) full curves, b) details of unloading

Figure 6-2 refers to the force measured by the top punch and displacement of the top punch. The bottom force follows the same trend as the top force but the magnitude of the bottom force is about 10% less than the top one. This is because of the friction between the powder and the die wall, which can be reduced by pre-lubrication of the die, but not to be completely eliminated.

It can be seen in Figure 6-2 that the linear and nonlinear corrections give almost the same corrected curve for loading. Figure 6-2 also indicates that the difference between an uncorrected curve and a correct one is significant. Therefore, in order to measure the deformation of the powder, the correction method to eliminate the system compliance is essential.

6.3 Non-homogeneous stress state

The Janssen-Walker method of differential slices (Neddermann, 1992) makes it possible to estimate the axial stress distribution in a specimen in a die subject to different top and bottom forces. Figure 6-3 illustrates the diagram used in the force balance equation to express the axial variation of stress which is

$$\sigma_z = (\sigma_T)^{\frac{z}{H}}(\sigma_B)^{1-\frac{z}{H}} \quad (6-2)$$

where z is the position of the slice from bottom of the powder, H is the height of the powder

σ_T and σ_B are the axial stresses at top punch and bottom punches, respectively.

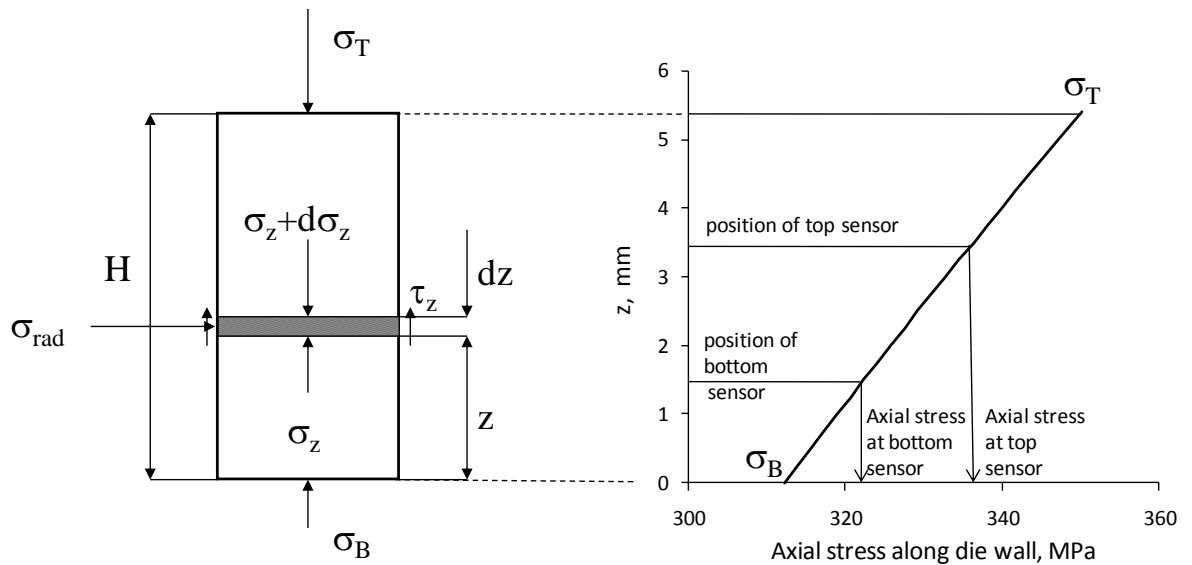


Figure 6-3 Axial stress distribution along the height of the compact determined using the Janssen-Walker method of differential slices

Using equation (6-2), it is possible to calculate the axial stress corresponding to the positions of the radial stress sensor ($z=1.5$ and $z=3.5$ mm) from the bottom of the specimen as illustrated in Figure 6-3. In this figure the stress magnitudes correspond to a top axial stress of 350 MPa when the specimen height is 5.4 mm.

The axial and radial stress components corresponding to one or the other of the radial stress sensors can then be used to calibrate the Drucker-Prager cap model. Figure 6-4 illustrates three hardening laws that have been determined from the force-displacement curves presented in Figure 6-2. In this calibration procedure the axial and radial stress corresponding to the position of the top sensor were used. The three situations were based on specimen height are considered as follows

- raw force-displacement data (no correction for system compliance)

- force-displacement data using linear system compliance
- force-displacement data using non-linear system compliance.

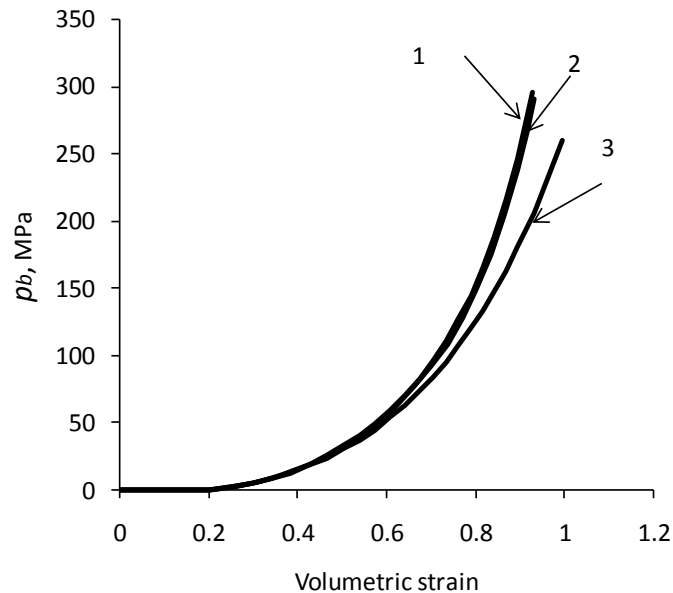


Figure 6-4 Hardening laws obtained from raw data (labelled 3) and corrections using linear (2) and non-linear (1) system compliance.

Based on the observation that the non-linear compliance correction curve reflects the physical process more accurately, we use the non-linear compliance correction method to generate the constitutive relation of the material.

6.4 Compliance corrections for loading and calibration of model parameters

The accuracy of the initial stress-strain (or force-displacement) graph with further attention to the stress states in the compact is examined in detail below. It was indicated that the hardening laws presented in Figure 6-4 correspond to the axial stress and radial stress at the top radial stress sensor. If the bottom radial sensor

measurement and the corresponding axial stress were used, then a different hardening law is obtained. It would appear that the hardening law is dependent on the location of the radial stress sensor. This is because not only the axial stress varies in the compact (see Figure 6-3) but so does the axial strain.

The strain calculated using equation (6-1) is an average axial strain. Similar to the stress variation, the axial strain is decreasing from the top to the bottom of the specimen. The axial strain corresponding to the sensor position can be established using the following procedure.

The average axial stress determined by using the Janssen-Walker method is

$$\sigma_{average} = \frac{\sigma_T - \sigma_B}{\ln \frac{\sigma_T}{\sigma_B}} \quad (6-3)$$

The average axial stress-average axial strain response of the sample can therefore be determined as illustrated in Figure 6-5 curve 1. Knowing the axial stress at the position of a sensor makes it possible to estimate the corresponding axial strain using Figure 6-5.

Thus it is possible to establish a consistent set of axial strain, axial stress and radial stress at any position z along the height of the specimen. The radial stress is measured by 2 sensors. The consistent set of stress-strain curves are also presented in Figure 6-5, overlapping the average stress-strain curve. Thus the stress strain curves are now independent on the axial position. The method above gives identical axial stresses for identical strains at height of the two radial stress sensors. The radial stress – axial strain curves, where the axial strain is now taken at the heights of the two sensors

include some experimental scatter as illustrated in Figure 6-5. The average is used for calibration purposes.

As described in section 4-2 of Chapter 4, the evolution of the shape of the cap surface R and the hardening law p_b are calibrated and presented in Figure 6-6 a,b respectively.

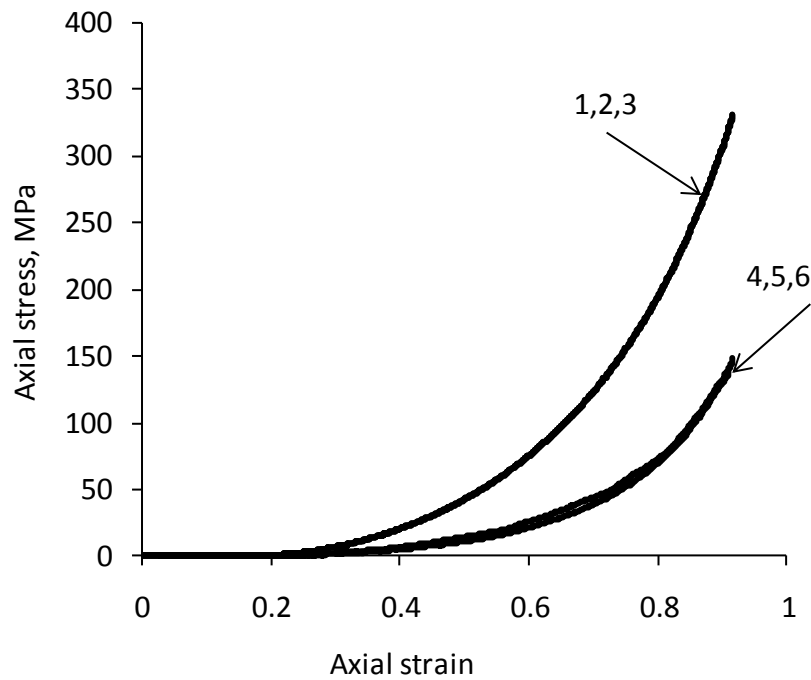


Figure 6-5 Stress-strain curves, 1 average axial stress-axial strain, 2 axial stress at top sensor vs. axial strain at top sensor, 3 axial stress at bottom sensor vs. axial strain at bottom sensor, 4 radial stress at top sensor vs. axial strain at top sensor, 5 radial stress at bottom sensor vs. axial strain at bottom sensor, 6 average radial stress vs. average axial strain

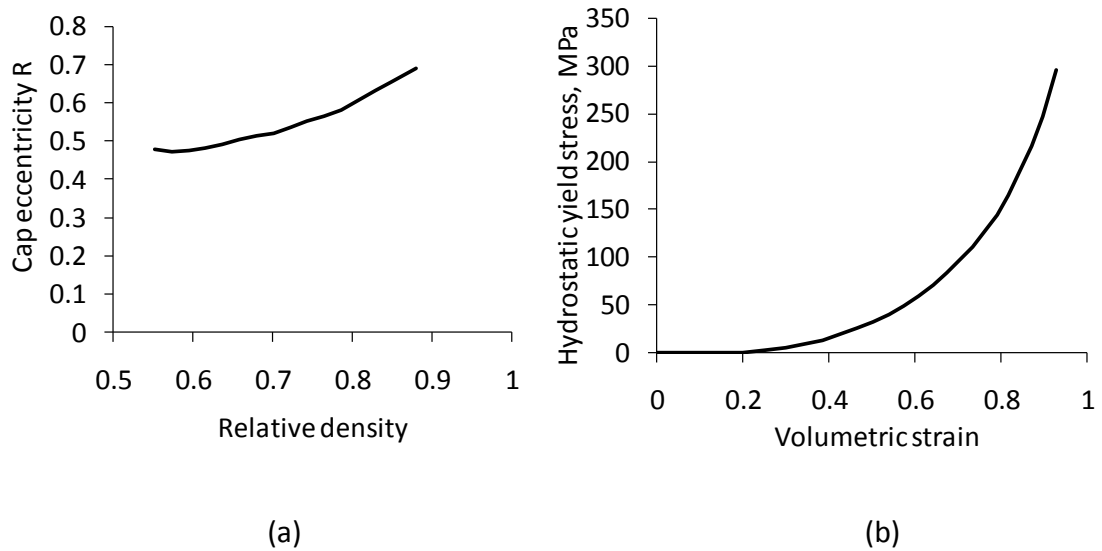


Figure 6-6 Parameters of the cap surface a) cap shape parameter as a function of relative density and b) hardening law

Figure 6-7 presents a family of Drucker-Prager cap surfaces corresponding to different levels of densification. This figure summarises the calibration of the Drucker-Prager cap model for a particular powder and can readily be implemented in finite element analysis. The families of DPC surfaces are not self similar, as the cohesion, internal friction angle vary during compaction and there is also an evolution of the shape and size of the ellipse. Note that the cohesion d and friction angle β does not play major role in compression stage for simple geometry. However, the failure line becomes important at unloading stage (Wu et al., 2008, Sinha et al., 2009).

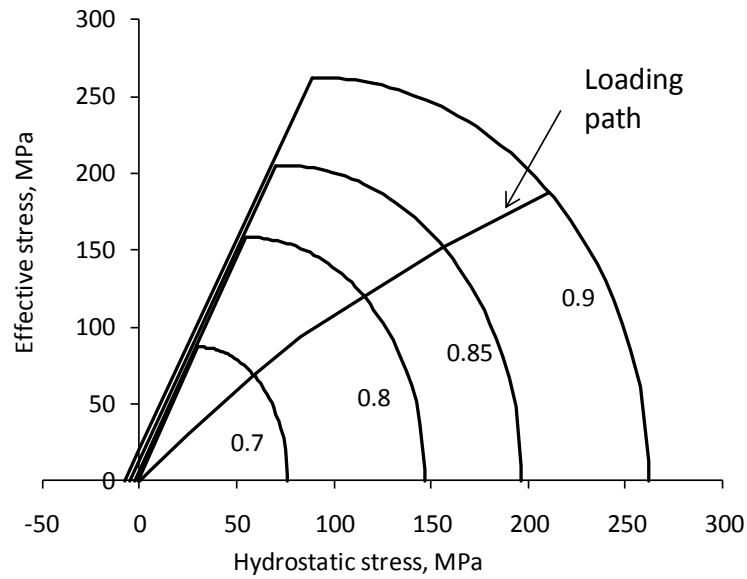


Figure 6-7 Drucker-Prager cap surfaces, the labels indicating relative density

A series of axial stress-relative density curves are plotted in Figure 6-8. Specimens were compressed to different densities with respect to the maximum top pressures. Figure 6-8 suggests that the repeatability of the tests is high.

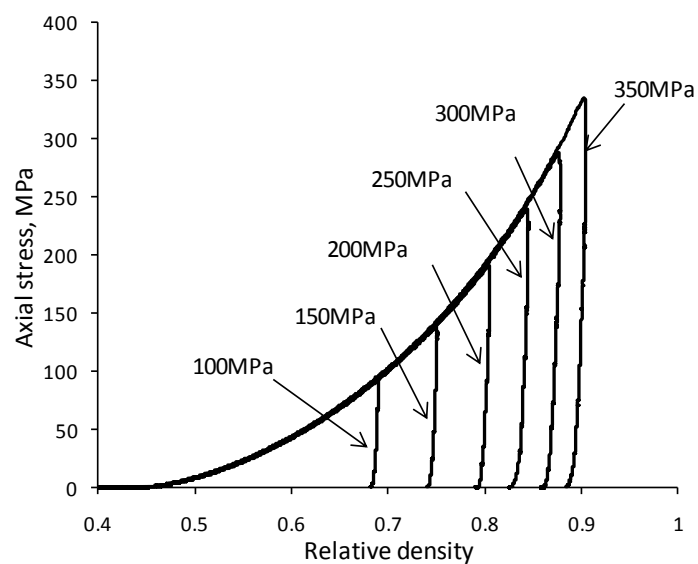


Figure 6-8 Axial stress- relative density curves during loading and unloading from various relative densities

6.5 Compliance corrections for unloading and calibration of elastic parameters

To fully describe the elasto-plastic behaviour, the elastic properties (Young's modulus and Poisson's ratio) must also be determined as functions of relative density. The elastic response of powder compacts may or may not be linear in practice, however, the literature indicates that unloading in the die is usually non-linear. This raises questions about the choice of stress range to fit straight lines for the determination of the elastic parameters. Different methods that account for the elastic compliance of the testing system can affect the calculated elastic properties as shown below.

Figure 6-9 presents a typical unloading curve following die compaction. The experimental data are corrected for non-linear and linear compliance. Figure 6-9 shows that the elastic compliance of the system is one order of magnitude larger than the elastic deformation of the material during unloading. The slopes of the unloading curves in Figure 6-9 are parallel and curved in the higher force range.

A more detailed examination of the loading frame suggests that different parts of the system are subject to different loads, as measured by the top and bottom load cells.

Based on this observation, the system can be divided into 3 parts, connected in series

- basic system (when the die table is removed), illustrated in Figure 6-10a.
- top punch (Figure 6-10b)
- bottom punch assembly

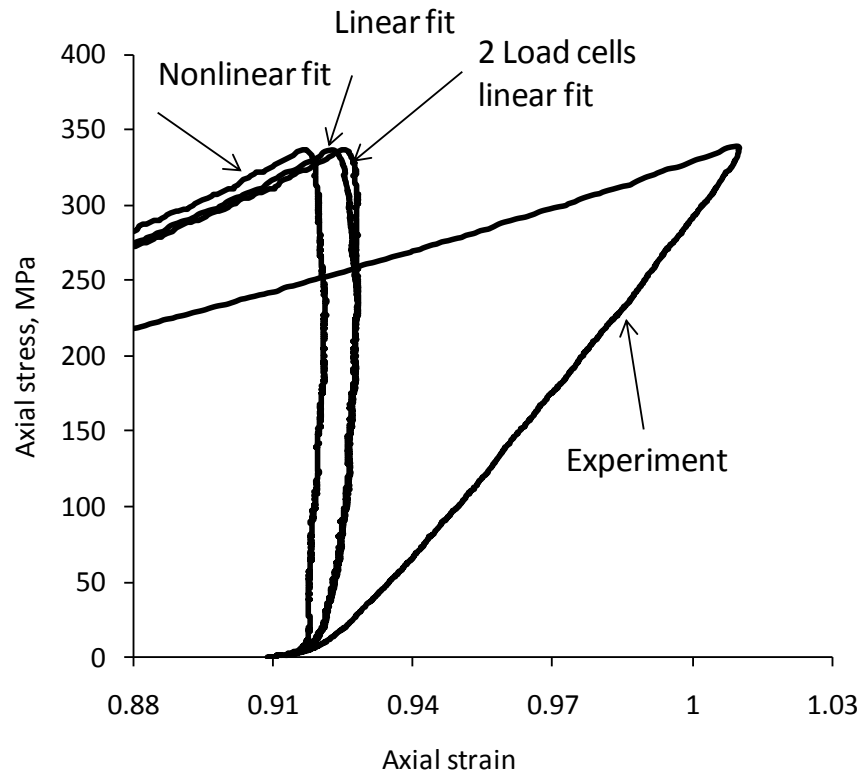


Figure 6-9 Stress-strain data during unloading in a die using experimental data and various correction methods

The elastic compliance response of the complete system (Figure 5-3) presented in Figure 6-1 is 0.0148 mm/kN for the linear section. The elastic compliance of the basic system was measured as 0.00730 mm/kN; this is about twice as large as the value that indicated in the specifications of the testing machine, because the basic system (Figure 6-10a) includes load cells and other fixtures. The compliance of the top punch is calculated using finite element analysis: 0.00267 mm/kN. The material property used in this simulation is: Young's modulus, 200GPa and Poisson's ratio, 0.3.

The compliance of the bottom punch assembly, which is 0.00483mm/kN, can be calculated by subtracting the basic system and the top punch compliance from the compliance of the total system. This also suggests that different connectors of the

system have different stiffness, which should be identified in order to calibrate unloading curve correctly because the spring back of the material is very sensitive to the displacement measurement.

The three parts of the system identified above are subject to different loads: the basic system and the top punch are subject to the force measured by the top load cell. The bottom punch assembly is subject to a force which is measured by the bottom punch. Meanwhile, the die table assembly is subject to a force which is the difference between the top and bottom forces; however, the compliance of the die table does not influence the determination of the height of the compact.

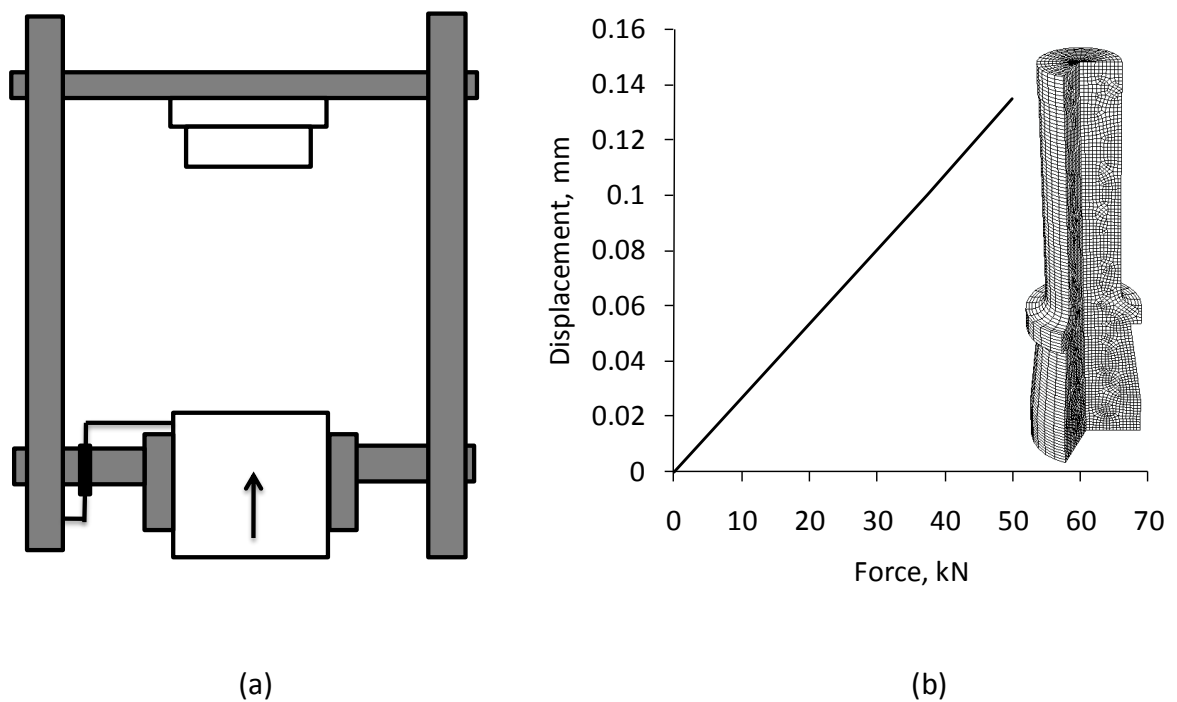
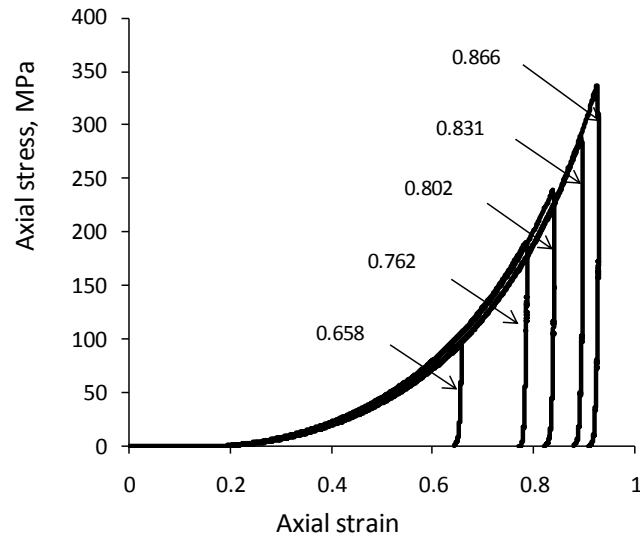


Figure 6-10 Elements contributing to total compliance of the system, a) basic system, b) finite element analysis of top punch compliance

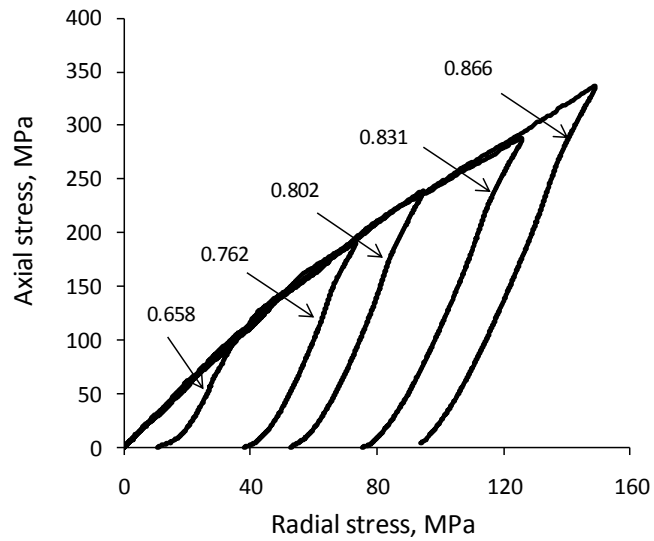
Based on the above considerations the system compliance was obtained using the actual force that deforms various components. The linear correction using two load cells is illustrated in Figure 6-9 (curve labelled “2 load cell linear fit”). The unloading curve becomes relatively straight and it is now straightforward to estimate its slope in order to determine Young’s modulus and Poisson’s ratio. These parameters are obtained by applying Hooke’s law for axisymmetric unloading with zero radial strain. By pressing specimens to different densities the evolution of the elastic parameters as functions of relative density is determined.

The axial stress/ axial strain and axial stress/radial stress curves of which the compacts were compressed up to different densities are illustrated in Figure 6-11 a) and b), respectively.



(a)

Figure 6-11 a) Axial stress/axial strain, b) Axial stress/Radial stress curve during loading and unloading, the labels indicating relative density of specimens



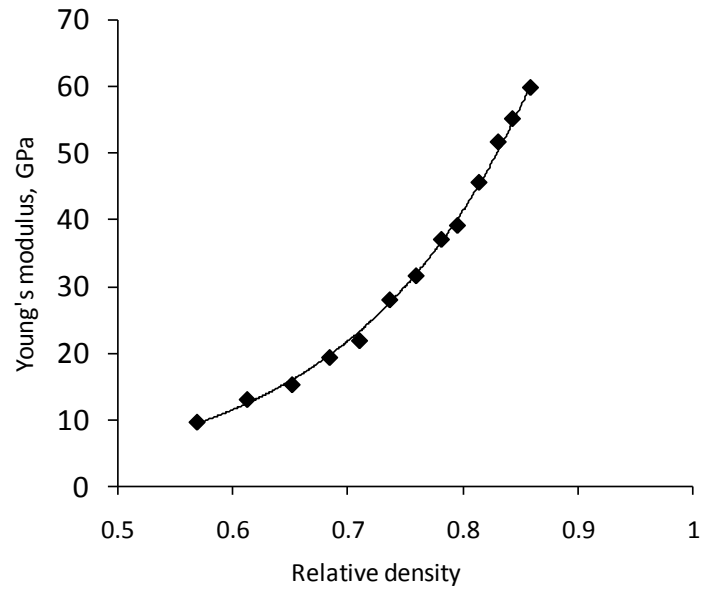
(b)

Figure 6-11 (Continued)

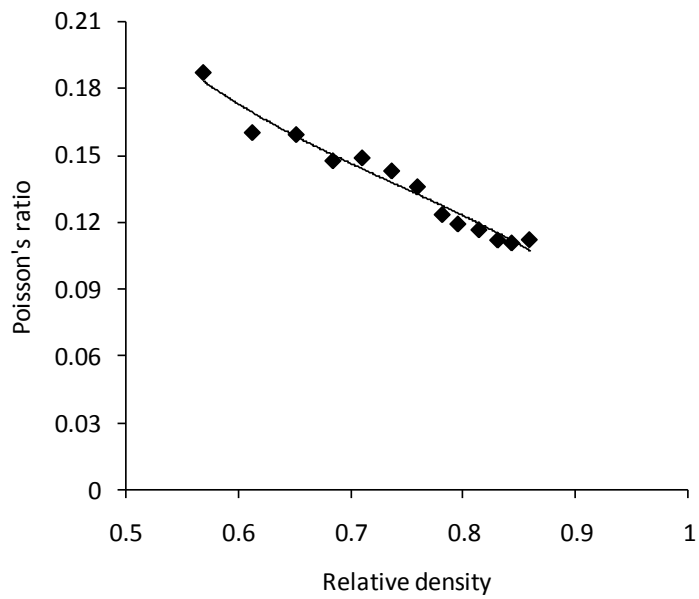
From unloading curve of axial stress/radial stress as shown in Figure 6-11b, according to equation (4-30), we can obtain Poisson's ratio for a range of different densities.

Accordingly, the Young's modulus can be obtained using equation (4-29).

As shown in Figure 6-12 a and b, the Young's modulus and Poisson's ratio are plotted as a function of relative density



(a)



(b)

Figure 6-12 a) Young's modulus E , b) Poisson's ratio ν as a function of density using unloading curve method

The evolution of Poisson's ratio ν suggests that in the lower density range (4~6.5g/cc) Poisson's ratio is not affected by solid phase material properties. Research indicates that Poisson's ratio has a concave dependence on density (Oliver et al., 1992): at low density range, as the density of the powder compact increases, the Poisson's ratio decreases before it approaches the solid phase value as porosity approaches zero. Restricted by the experimental conditions a higher density sample is not available, thus the increasing trend of the Poisson's ratio as density increase cannot be observed here. Meanwhile, the Young's modulus is seen to increase monotonically as density increases which is consistent with an expected increase in stiffness as the compact is densified.

In Figure 6-13, the stress state in effective stress-hydrostatic stress plane is presented. This curve demonstrates the loading path of the instrumented die system under compression and unloading. It becomes clear that there is shear failure occurring during unloading stage by using Figure 6-13. If the unloading curve interacts with the shear failure line, it means that the powder body yields and experiences dilation as defined by flow potential. Defects, such as cracks, may appear within the specimen. For Distaloy AE powder, such phenomenon was not observed. However, for other powders this curve can show if shear failure existed (Wu et al., 2008, Sinha et al., 2009).

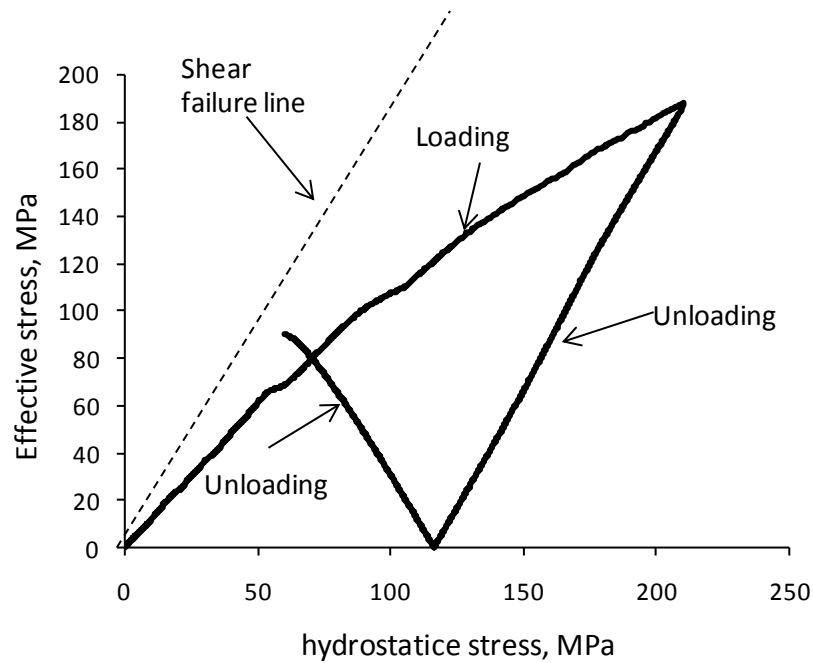


Figure 6-13 Effective stress against hydrostatic stress curve during loading and unloading for Distaloy AE powder

6.6 Friction coefficient

In order to measure the friction coefficient, Janssen-Walker (Neddermann, 1992)

method can be used and the friction coefficient can be estimated by

$$\mu = \frac{D}{4H} \frac{\sigma_B}{\sigma_{rad}} \left(\frac{\sigma_T}{\sigma_B} \right)^{\frac{z}{H}} \ln \frac{\sigma_T}{\sigma_B} \quad (6-4)$$

where σ_T , σ_B , σ_{rad} , z , H , and D are the stress at the top and bottom punches, the radial stress, the distance of the sensor from the top punch, height and diameter of the specimen.

The derivation of equation (6-4) was presented elsewhere (Sinka et al., 2001, Sinka et al., 2004).

The friction coefficient variation with contact pressure is presented in Figure 6-14.

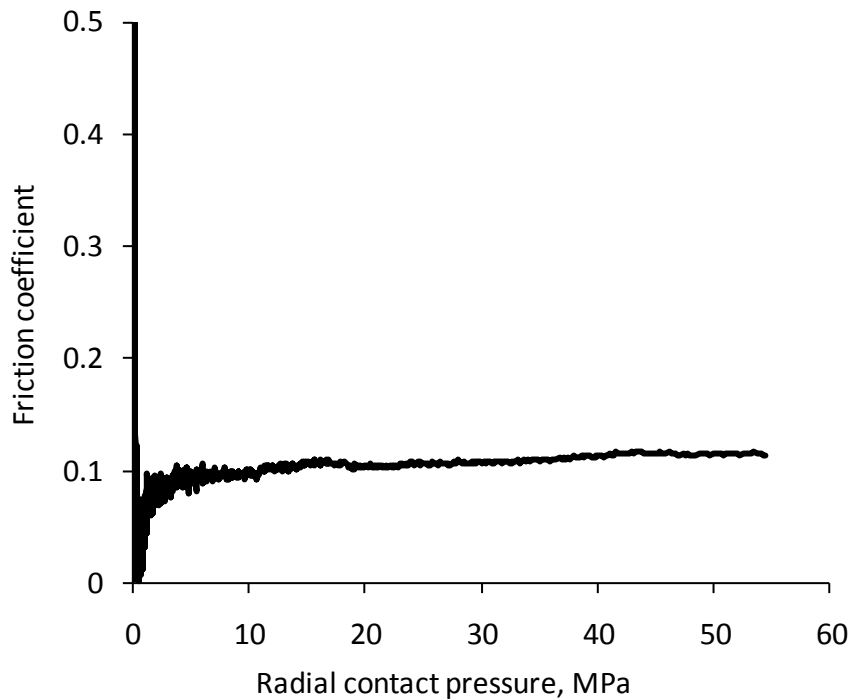


Figure 6-14 Variation of the friction coefficient with radial contact pressure

As shown in Figure 6-14, Friction coefficient depends on contact pressure. Such phenomenon has also been observed in other literature (Sinka et al., 2001). Other factors, such as sliding velocity, (PM Modnet group, 1999) also affect the friction and a sophisticated friction model was proposed (Wikman et al., 1997)

For the case of Figure 6-14 constant value (e.g. approximately 0.1) which dominates in the whole compaction process will give a reliable accuracy without introducing complicated model for friction which will at the same time simplify the simulation.

6.7 Conclusions

Sources of error in material calibration were examined in detail. The focus is on determining an accurate stress-strain curve when 1) the stress and strain are not homogeneous in the specimen and 2) the specimen is inaccessible for direct measurement for its deformation.

The stress distribution in the cylindrical compact was analysed using the Janssen-Walker method of differential slices. Despite that the method involves a number of assumptions, a data extraction algorithm was proposed that accounts for inhomogeneity induced by friction between powder and die wall. Detailed data extracting procedures were presented for both elastic and plastic parameters.

The specimen displacement is determined by measuring the displacement of the loading system. This involves considerable elastic deformation of the elements of the testing frame. The elastic compliance of various elements was measured or calculated using finite element stress analysis. It was shown that the deformation of the two punches is significant compared with the compliance of the other elements, requiring correction for compliance, even if stiffer frames or more appropriately positioned displacement transducers were employed.

Linear and non-linear compliance curves were employed for correction. Loading involves large strain of the order on unity; therefore the choice of correction method (linear or non-linear) is not significant, nevertheless it influences the hardening law and thus the accuracy of predicting the compaction force. However, during unloading, the deformation of the specimen was one order of magnitude smaller than that of the loading frame used. This situation was investigated in further detail and a correction

method was developed whereby the elastic displacements of various elements of the testing frame were determined based on the actual load they experienced. This resulted in relatively smooth and linear unloading curves, removing some ambiguity in terms of the selection of the range for slope estimation.

Detailed data extraction procedures were presented and the parameters of a Drucker-Prager cap model were determined using relative density as state variable. The elastic-plastic constitutive model and the friction between powder and die are two experimental inputs in order to model powder compaction. The DPC model presented in effective stress- hydrostatic pressure stress plane is a family of yield surfaces and plastic flow surfaces. Friction is determined using instrumented die by measuring the radial stress and axial stress. The results of Young's modulus and Poisson's ratio as function of relative density were also presented.

Chapter 7. Modelling powder compaction

The fully calibrated model in Chapter 6 is implemented and validated as follows. Firstly, the prediction of top and bottom punch forces are studied and compared with experimental data for loading. Secondly, the correction method for unloading is examined and validated. Finally a simplified DPC model is considered for practical purpose and its applicability is also explored.

To summarise the fully calibrated model, the material parameters provided in previous chapters are

- d -Cohesion and β -internal friction angle (see Figure 4-9)
- R -cap shape parameter and p_b -hardening rule (see Figure 6-6)
- E -Young's modulus and ν -Poisson's ratio (see Figure 6-12)

The powder compact is modelled by 4-node linear axisymmetrical elements (ABAQUS v6.7, CAX4). The finite element mesh of the shape of powder before compaction is shown Figure 7-1, which consists of 240 elements. The initial height (mm), diameter (mm) and relative density of the metal powder (Distaloy AE) are: 13.5, 10.5 and 0.346, respectively. The die and punches are modelled as rigid surfaces. The friction interaction between powder and die wall and punches is described using Coulomb's law of friction. Simulation is carried out by moving the top punch down by a specific distance statically.

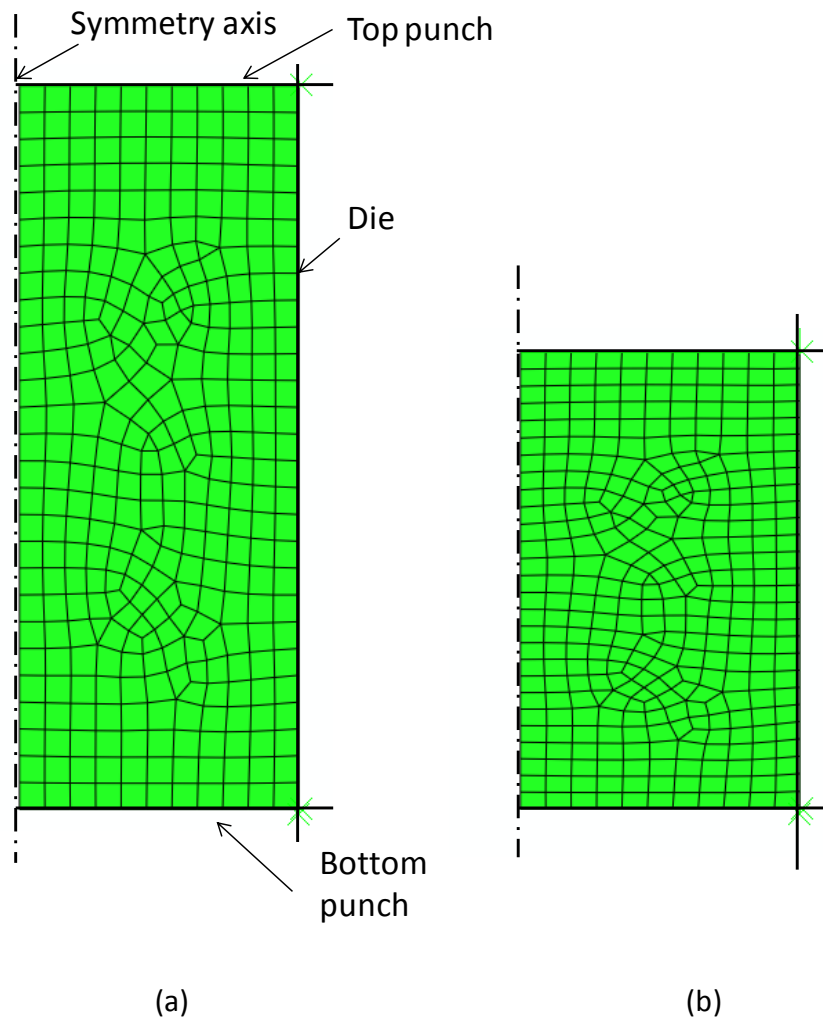


Figure 7-1 Finite element meshes a) before compaction and b) at the end of compaction

When using the finite element package ABAQUS, the material parameters of DPC model are expressed using relative density as solution dependent variable. To define relative density as a state variable a user subroutine USDFLD is created. Thus the elastic and plastic material properties are updated at each time step.

7.1 Validation of constitutive model and compliance correction

method

The material hardening law is validated first by compressing a single element under frictionless condition in a closed die. Figure 7-2 presents the stress-strain data determined from Figure 6-2 for the three situations. Overlapping the experimental data there are three curves which were generated by implementing the hardening laws in Figure 6-4 into the finite element package Abaqus. Figure 7-2 is provided in order to highlight that given a set of stress-strain data, it is possible to calibrate a constitutive model, implement it into a finite element package, and reproduce the original set of data as model prediction. This kind of argument is often shown as proof that model calibration and validation procedures were correct without examining the validity of the original stress-strain curve. As shown in Figure 7-2, the output stress-strain curves overlap perfectly with the input data obtained by the two correction methods and the non-corrected one. Therefore, the correction method needs to be validated so that the constitutive law of the material can be correctly obtained.

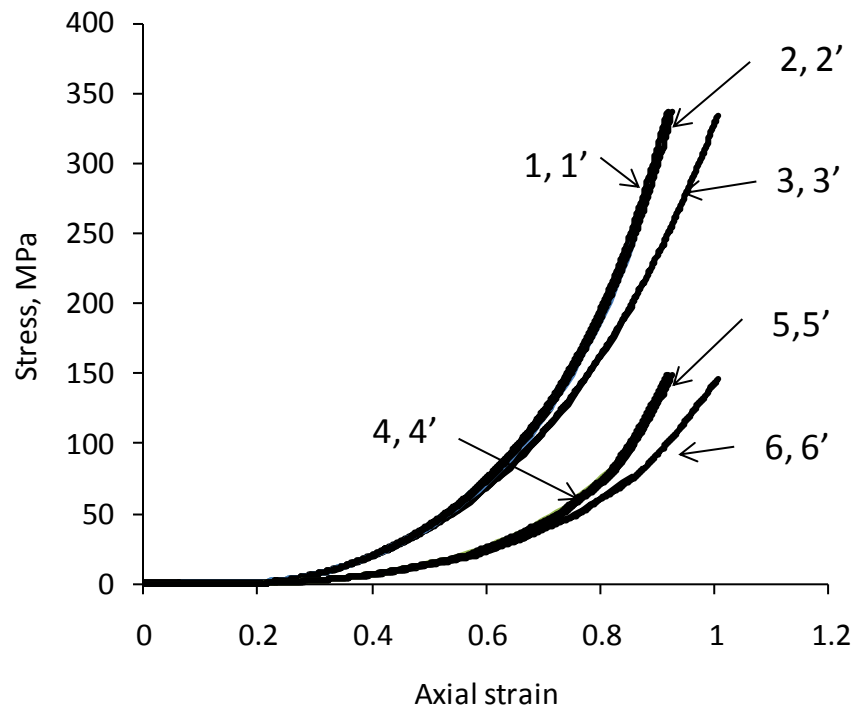
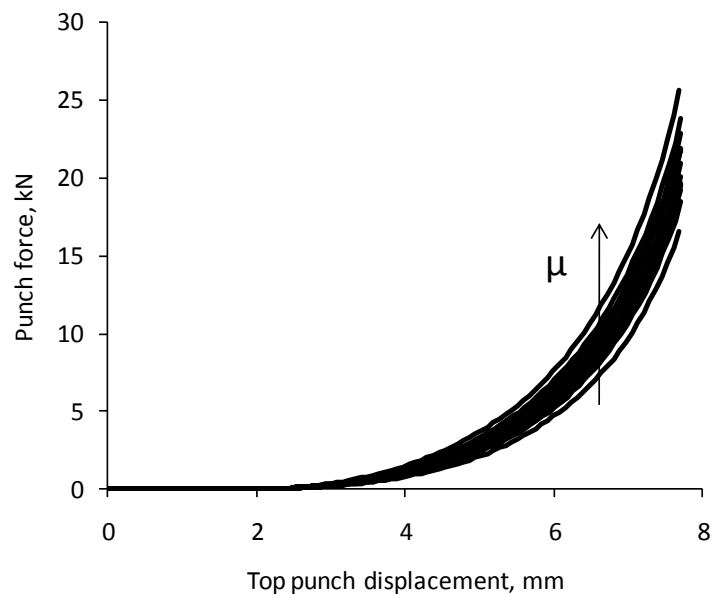


Figure 7-2 Stress-strain data obtained from force-displacement data and different correction methods for system compliance, 1-axial stress for non-linear correction, 2-axial stress for linear correction, 3-axial stress for uncorrected data, 4-radial stress for non-linear correction, 5-radial stress for linear correction, 6 radial stress for uncorrected strain data. Primes (') indicate the corresponding numerical analysis result, which overlap the experimental data

In the following section the calibrated model is compared with experiments for both loading and unloading of the die compaction.

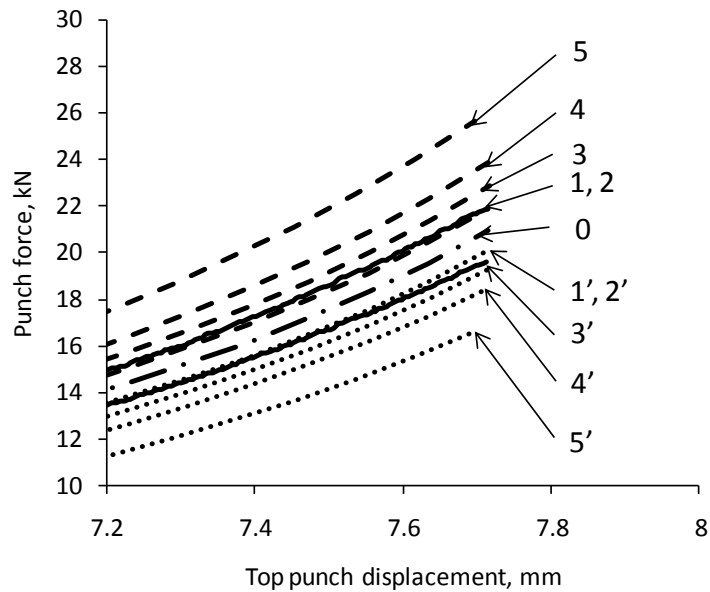
The material parameters of DPC model and the friction properties are given in Chapter 6. The closed die compaction was simulated. In effect, the calibration procedure presented accounts for the effect of friction between powder and die wall during compression. In the numerical simulation, friction must be considered.

Using Equation (6-4) the friction coefficient was determined having a constant value of around 0.1. In Figure 7-3 we present a study of the force-displacement curves obtained using numerical modelling for a range of values for the coefficient of friction. It can be seen that as the friction coefficient increases, the difference in force between the top and bottom punches enlarges. It is observed that $\mu = 0.1$ overlaps the experimental data (Figure 7-3b) for both top and bottom punches. For $\mu = 0$ (frictionless) the stress-strain response from which the model was calibrated (Figure 6-5) is recovered. Figure 7-3 further illustrates that for accurate force-displacement predictions, the friction coefficient must also be measured accurately.



(a)

Figure 7-3 Effect of friction on force-displacement response, a) full curve, b) detail. Labels: 0 frictionless, 1 $\mu=0.1$, 2 experimental data, 3 $\mu=0.2$, 4 $\mu=0.3$, 5 $\mu=0.5$ corresponding to the top punch force. Primes (') are used to label data corresponding to the bottom punch force.



(b)

Figure 7-3 (continued)

During the unloading stage, the correction method described in Chapter 6 is applied. The simulated result of unloading force-displacement curve is presented in Figure 7-4. Figure 7-4 illustrates force-displacement curves during unloading after applying to non-linear correction, linear correction and linear correction using two load cells, respectively. In addition, numerical modelling results with the three correction methods are also shown. The numerical results agree well with the experimental data even at this level of detail. More importantly, it can be seen that

- the unloading curves obtained from linear and non-linear corrections are parallel; this is expected because Figure 7-4 is prepared using the higher range of the applied force, where the non-linear curve becomes linear

- the unloading curves from the 2 load cell correction and the experimental data are parallel, which validate the approach.

The above statements are quantified by the slope values indicated in Figure 7-4.

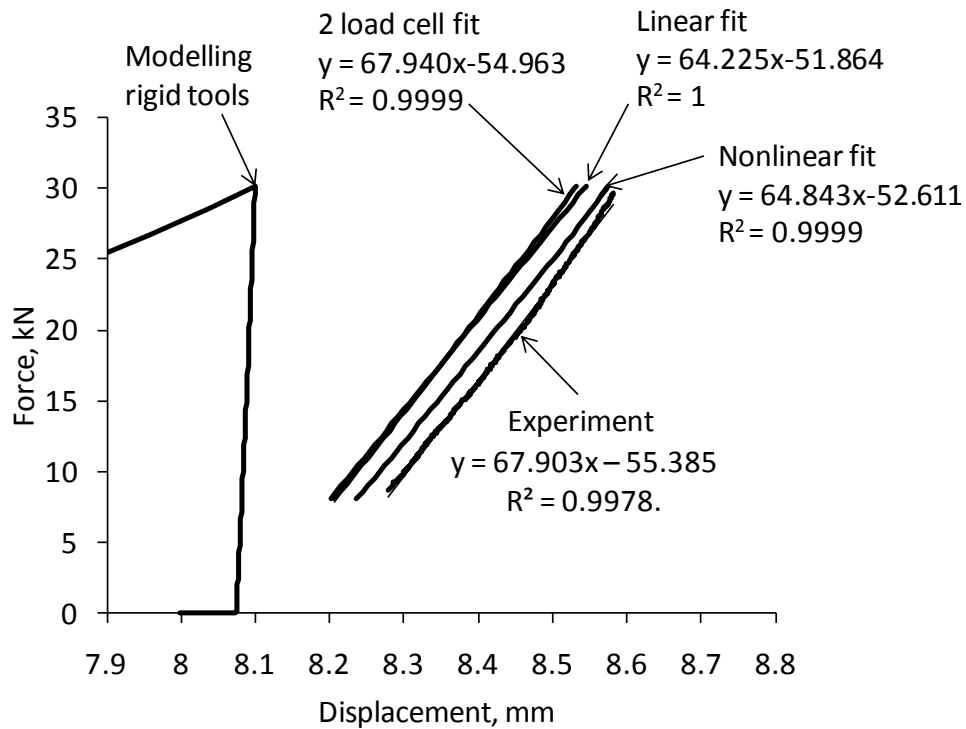


Figure 7-4 Slope of unloading line from experimental data and different compliance correction methods together with the corresponding numerical modelling results

Using the correction method based on two load cells the elastic properties were determined for a range of samples of different densities and the results are presented as shown in Figure 6-12. Thus, correction methods used during loading and unloading stage of die compaction are validated.

So far, the fully calibrated DPC model has been used. Next, some considerations of using simplified models are presented.

7.2 Practical considerations for modelling powder compaction

The fully calibrated model (Chapter 6) involves a large amount of experiments. In practice, some of the experiments, such as uniaxial and diametrical compression tests, may not be available for calibrating the material model. Therefore, for finite element analysis purpose, material parameters are often treated as constant (Michrafy et al., 2002, Coube and Riedel, 2000, and Cunningham et al., 2004).

In this section simplified constitutive models that can be used for powder compaction are examined. Given the development of general purpose commercial finite element packages over the last decade, the aim is to explore whether or not standard packages could be readily used to model the process. The complexity of the models is increased progressively highlighting their applicability and limitations.

As a basis for discussion, Calcium phosphate (see Section 4.1.2) was selected to calibrate simplified constitutive models for powder compaction

7.2.1 Constitutive data for powder compaction

At first, a model consisting of self similar compaction surfaces is used. The cohesion and internal friction angle in the Drucker-Prager model are assumed constant. The parameters of simplified DPC model are provided in Table 7-1.

Families of yield surfaces for different stages of compaction are presented in Figure 7-5a. The ellipses are calibrated using the constitutive data in Table 7-1. Thus the shapes of the compaction surfaces are dictated by the closed die compaction test. The size of the yield surfaces during compaction are determined using hardening rules, e.g. the change of hydrostatic yield stress as indicated in Figure 7-5b.

Table 7-1 Simplified DPC model parameters for A-Tab

Parameters	values
d -cohesion	0.01MPa
β -internal friction angle	55 degree
R -cap shape parameter	0.261
E -Young's modulus	210GPa
ν -Poisson's ratio	0.3
p_b -hardening rule	See Figure 7-5b

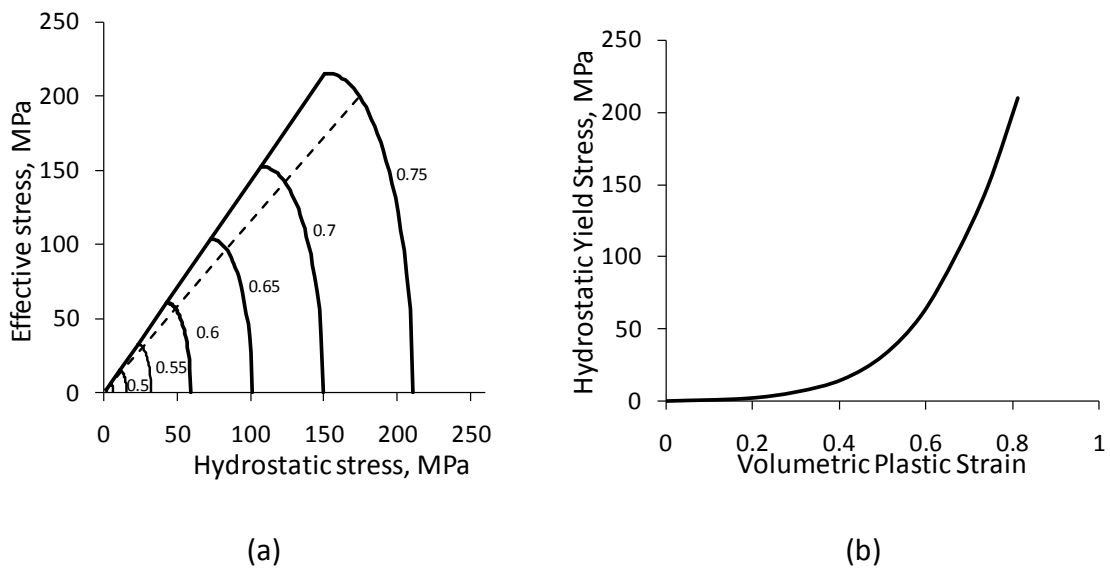


Figure 7-5 a) Yield surfaces for Drucker-Prager cap models. The labels indicate relative density (defined as 1-zero porosity), the dashed line indicates the loading path of closed die compaction, b) Hardening rules for Drucker-Prager cap models

Figure 7-6 illustrates the verification of the models for frictionless closed die compaction. It can be observed that the radial and axial stress match the experimental data for both constitutive models examined. This is not surprising as the models were calibrated using closed die compaction data in the first place.

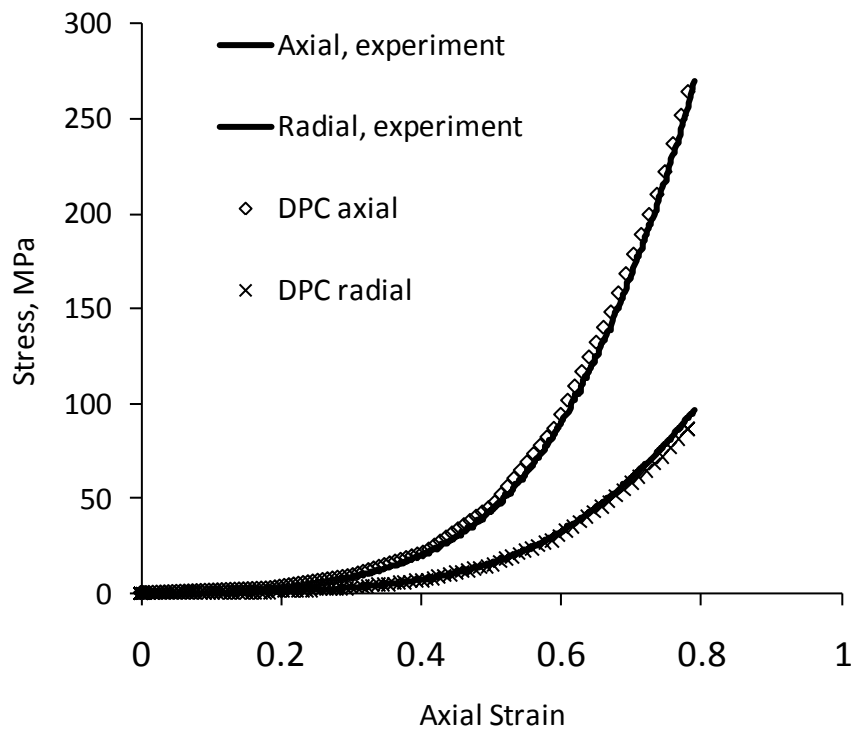


Figure 7-6 Verification of the models; a) comparison of experimental stress-strain curves with model prediction for frictionless compaction

7.2.2 Density distribution in powder compacts

Numerical analysis of the compaction of cylindrical specimens was carried out. The initial height of the cylinder was considered 13.5 mm and the initial density was 0.333 (uniform initially). In these simulations the bottom punch is maintained stationary and compaction was executed with the top punch only. Density distributions in flat faced

cylinders come about from the friction interaction between powder and die wall. In the absence of friction the density would remain uniform throughout the specimen during compaction. Figure 7-7 illustrates density distributions for different values of the friction coefficient between powder and die wall. The density contours are qualitatively similar and differ in magnitude with larger variations for higher friction. During compression, a high density zone is developed around the top circumference of the powder, while a low density zone is located around the bottom. The simulated density distribution is consistent with the experimental results obtained by others (Kim et al., 2002, Eiliazadeh et al., 2004 and Wu et al., 2005).

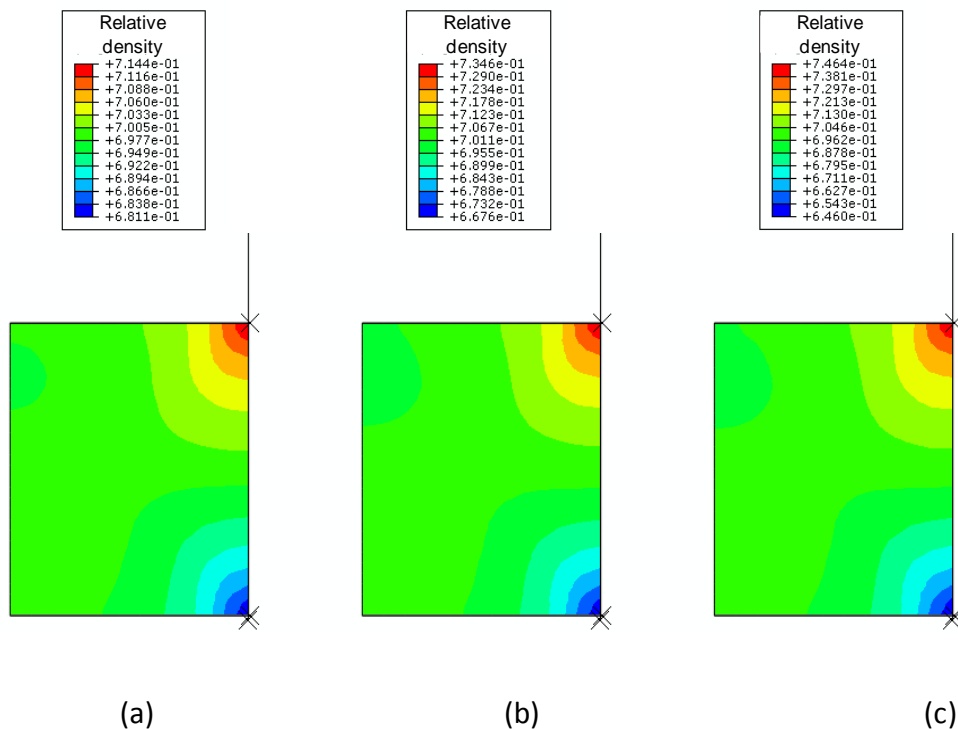


Figure 7-7 Relative density distributions in vertical cross sections of cylindrical compacts with values of the coefficient of friction between powder and die wall of a) 0.1, b) 0.2 and c) 0.3.

7.2.3 Force-displacement response

To this stage only plastic deformation was discussed. In reality, the material response is elasto-plastic. In the numerical simulations above a high elastic modulus ($E=210\text{GPa}$) was used so that plastic deformation dominated.

The effect of elastic parameters is illustrated in the parametric study illustrated in Figure 7-8, where different elastic moduli were employed. It is observed that if Young's modulus is sufficiently large (e.g. above 10 GPa) then plastic deformation dominates and the choice of elastic modulus does not considerably influence the stress-strain response.

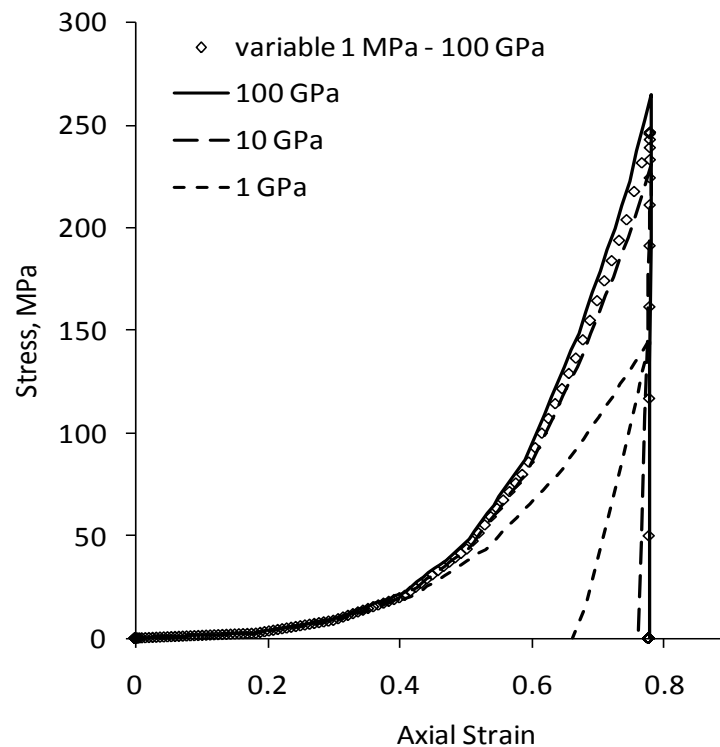


Figure 7-8 Effect of Young's modulus on stress-strain response for Drucker-Prager cap model.

The use of a single value (e.g. above 10 GPa) is convenient for numerical implementation and gives acceptable stress-strain response for flat faced cylinders.

However, as in Figure 7-8 it can be seen that if Young's modulus is chosen to be at a relatively lower value (e.g. 1GPa), then the stress output is significantly lower than the stress which the Young's modulus is chosen as an evolution of density. For example, if the variable Young's modulus is chosen as a reference, we can find that the output stress (when $E=100\text{GPa}$) is 8% higher than reference value. Similarly, a 6% lower value compared to reference value is obtained (when $E=10\text{GPa}$). This suggests that for single value of Young's modulus, there is always a stress difference between single value and true experiment Young's modulus evolution during compaction. Therefore, the evolution of Young's modulus during compaction should be obtained in order to get a correct simulation result, especially when Young's modulus is not easy to estimate for powder compact.

In practice, the elastic and plastic model parameters evolve together during densification and it is important that they are calibrated appropriately using experimental data. Moreover, numerical convergence is difficult for complex geometries (e.g. curved punches, which make progressive contact with the powder during compression) when fixed values are used for Young's modulus. The simulation of the density distribution in a curved faced tablet presented in Figure 7-9 is possible only by implementing a variable Young's modulus that increases during compaction. The stress-strain response of the flat faced configuration with variable modulus is presented in Figure 7-8; as before, the elastic modulus does not significantly influence

the stress-strain response (provided the values are high enough compared with the yield strength).

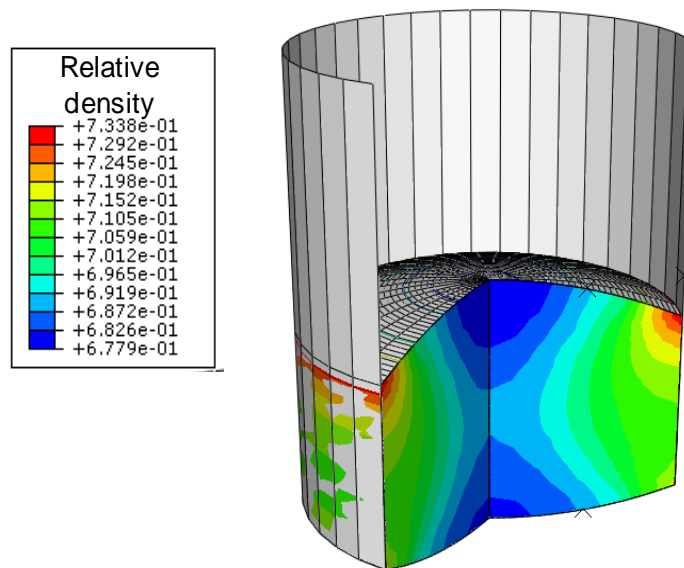


Figure 7-9 Density distribution in a curved faced tablet

7.3 Conclusions

The essential role of the correction method for model calibration is examined. At the loading stage, the friction coefficient must be measured accurately in order to reintroduce friction correctly in the numerical analysis. At the unloading stage, the two-load cell linear fit is proved to be suitable for correction by considering the friction effect on the system compliance of which different parts having different stiffness under different load.

For practical purposes, simplified DPC models are examined. A study of the influence of elastic response is presented, demonstrating that the choice of elastic parameters does not influence the stress-strain response significantly provided the values are high

enough and plastic deformation dominates. However, when a low E is chosen, the plastic dominated deformation cannot be ensured. As a result the force displacement response will be significantly different from that of high E . Density distributions in cylindrical parts with flat and curved faces are generated using Drucker-Prager cap model. It is demonstrated that for complicated geometries and in the presence of friction, it is important for numerical convergence that Young's modulus is correlated with the evolution of the yield surfaces. For such situations, only models with variable elastic parameters could be employed. The variable parameter model is physically more realistic as it captures the elastic response as the material evolves from the powder state into a dense compact: Young's modulus increases simultaneously as the yield surface expands during densification.

Chapter 8. Experimental study of tablet breakage

8.1 Introduction

Tablet strength is an important quality attribute that is tested continuously during tablet manufacturing. The industry standard method of testing tablet strength is the diametrical compression test which is described in Chapter 4 (Section 4.5). The material tensile strength of flat faced tablet can be related to the break force using an analytical expression (equation 4-8).

The diametrical compression test is also widely used in design and manufacturing quality control of curved faced tablets and more complex tablet shapes in general. Because of the geometry, however, the relationship between the break force in diametrical compression and the tensile strength of the material is not known. This problem was addressed by Pitt and co-workers (Pitt et al., 1988, 1989a) who established the following empirical relationship between the break force of convex shaped gypsum specimens and the tensile strength of the material

$$\sigma_d = \frac{10F}{\pi D^2} \left(2.84 \frac{t}{D} - 0.126 \frac{t}{W} + 3.15 \frac{W}{D} + 0.01 \right)^{-1} \quad (8-1)$$

where D is the diameter, t is the total thickness, W is the width of the band area.

The geometry of the tablet is defined in Figure 8-1. R represents the radius of curvature.

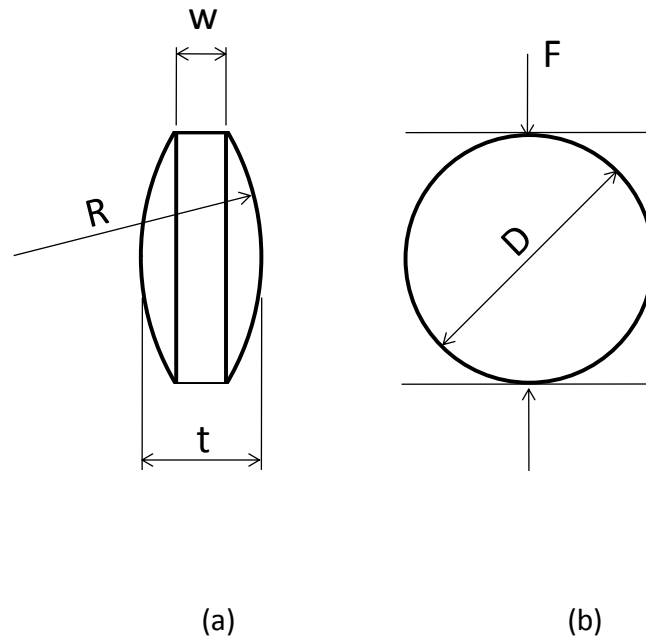


Figure 8-1 Geometry and diagram of diametrical compression test of curved faced tablets (a) side view (b) top view

Equation (8-1) gives the tensile strength of the material as a function of normalised terms (t/D , W/D , t/W) describing the curvature of the face. The numerical values of the coefficients are determined from experiments carried out on disks with different curvature and thickness. Thus, equation (8-1) has significant practical applications relating the break force with a material property. It has been established in the industry and is included in the United States Pharmacopoeia (USP, 2011). Its validity, as stated by the authors is if $0.1 \leq W/D \leq 0.3$ and for $W/D = 0.06$ with $D/R < 0.1$.

The practical use of equation (8-1) was presented by Pitt et al. (1989b) for aspirin tablets and by Hariran and Newton (1999) for microcrystalline cellulose tablets. They discussed the dependence of the material strength on porosity (which is determined by the compaction pressure) and that the results might be influenced by the porosity

and flaw distributions within the tablet. Using break force data the tensile strength of a range of tablets with different curvatures was calculated using equation (8-1) and the geometry which gave maximum strength was identified.

We make the following observations:

- Equation (8-1) has three dimensionless terms, out of which only two are independent. Therefore simplifications may be possible.
- Published experimental data on the break force of curved faced tablets make use of equation (8-1) to determine the tensile strength of the materials, however, these experiments were not designed to provide further validation of equation (8-1).
- Equation (8-1) does not reduce to Hertz's formula for flat faced tablets (equation (4-8)).

In this chapter we perform a comprehensive set of experiments to determine the break force of a range of tablets with different curved faces manufactured at different compaction pressures. The data are processed as in the original paper by Pitt et al. (1988). The fitting parameters and the form of equation (8-1) are discussed in the light of the observations above. A new, simplified equation is proposed and the tablet geometries for which it is applicable are discussed with reference to the failure mode of the tablets.

Microcrystalline cellulose (MCC) powder (see section 4.1.3) is used in this study.

8.2 Curved shaped tablet

The curved shaped tablets are manufactured using the procedure described in Chapter4 (Section 4.2). The die used to prepare convex shape tablets has a diameter of 10.318 mm and 5 sets of different curvature punches (Manufactured by iHolland, UK) having the same diameter are used to press curved faced tablets. The geometry of curved faced tablets is indicated in Table 8-1.

Table 8-1 Tablet shapes (tablet radius R illustrated in Figure 8-1)

Punch shape	R, mm
Shallow	30.12
Standard	13.869
Deep	10.44
Extra deep	7.514
Ball	5.599

Three tablet weights were used: 200, 300, 400mg. The experimental plan indicated in Table 8-2 was designed to produce a range of tablets having a range of densities and a range of curvatures and a range of thicknesses. For a given weight and geometry the band thickness W (illustrated in Figure 8-1) decreases as the compaction pressure is increased. Compaction is executed for pressure levels of: 25, 50, 75, 100, 150, 200 and 250MPa. These represent top punch pressure which is defined as the top punch force divided by the cross-section area of the die.

In order to avoid punch damage during the compaction process, for a given tablet weight the compaction pressure was not increased further once W became less than 1 mm. Three repeat tests were carried out for each individual weight and punch curvature. Tablets manufactured are presented in Table 8-2.

The tablets were then tested by diametrical compression, the testing procedure is also provided in Chapter 4, (Section 4.4).

Table 8-2 Experimental design for curved faced tablets. Tick indicates tablet manufactured, Cross indicates that the tablet was not manufactured because the band thickness (W) became too small.

Weight: 400mg	Compaction pressure, MPa						
Punch shape	25	50	75	100	150	200	250
Shallow	✓	✓	✓	✓	✓	✓	✓
Standard	✓	✓	✓	✓	✓	✓	✓
Deep	✓	✓	✓	✓	✓	✓	✓
Extra deep	✓	✓	✓	✓	✓	✓	✓
Ball	✓	✓	✗	✗	✗	✗	✗

Weight: 300mg	Compaction pressure, MPa						
Punch shape	25	50	75	100	150	200	250
Shallow	✓	✓	✓	✓	✓	✓	✓
Standard	✓	✓	✓	✓	✓	✓	✓
Deep	✓	✓	✓	✓	✓	✗	✗
Extra deep	✓	✓	✗	✗	✗	✗	✗
Ball	✗	✗	✗	✗	✗	✗	✗

Table 8-2 (continued)

Weight: 200mg	Compaction pressure, MPa						
	25	50	75	100	150	200	250
Punch shape	25	50	75	100	150	200	250
Shallow	✓	✓	✓	✓	×	×	×
Standard	✓	✓	×	×	×	×	×
Deep	✓	×	×	×	×	×	×
Extra deep	×	×	×	×	×	×	×
Ball	×	×	×	×	×	×	×

8.3 Results and discussion

Figure 8-2 summarises the experimental plan in terms of the dimensionless terms t/D and W/D which define a curved faced tablet. The data points relate to tablet geometry only as the tablets will have different densities depending on the compaction pressure applied. The area of the validity of Pitt's equation is indicated using dotted line. For flat faced tablet $t=W$ and in this case the experimental data points are omitted for clarity. Tablets with same curvatures will lie on straight lines, which are illustrated in Figure 8-2. The two lines labelled "a" and "b" were selected to illustrate the break force behaviour of tablets having increasing curvatures.

The data are analysed using the same procedures as Pitt et al. (1988). The original equation can be written in the form

$$\sigma_d = \frac{F}{\pi D^2} \left(a \frac{t}{D} + b \frac{t}{W} + c \frac{W}{D} + d \right)^{-1} \quad (8-2)$$

where a, b, c and d are empirical coefficients.

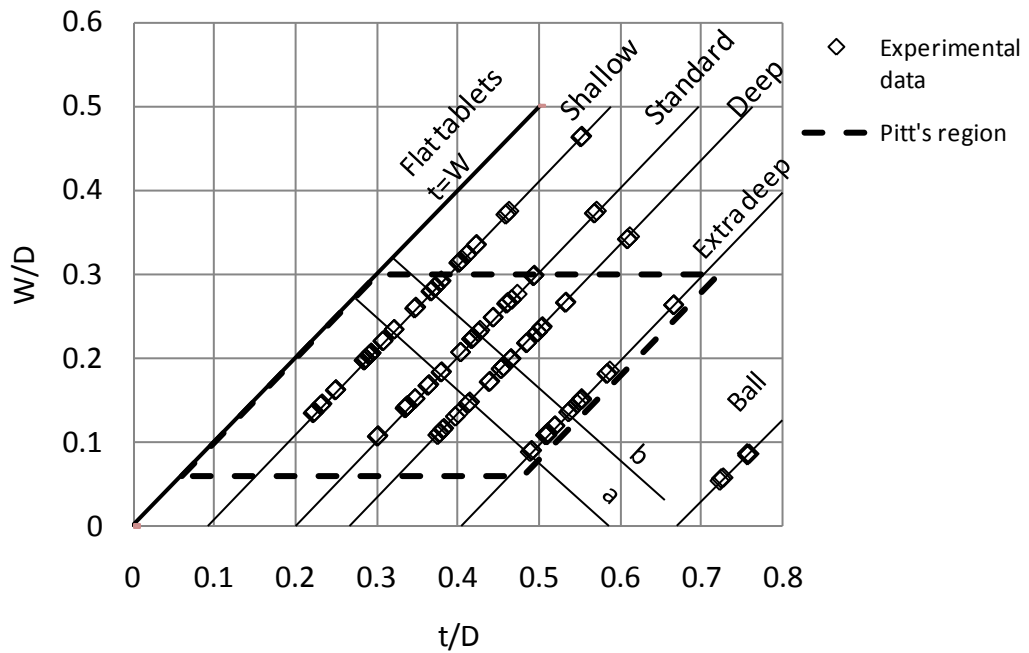


Figure 8-2 Experimental space for curved faced tablet geometry

Equation (8-2) is a relationship between the break force of the tablet, material tensile strength and tablet geometry. A practical measure of tensile strength can be obtained using diametrical compression tests of thin disks as described in Chapter 4 (Section 4.5). The tensile strength obtained for a range of thin flat faced tablets pressed to different compaction pressures is presented in Figure 8-3 as a function of relative density. Relative density is defined as the solid volume fraction of the compact.

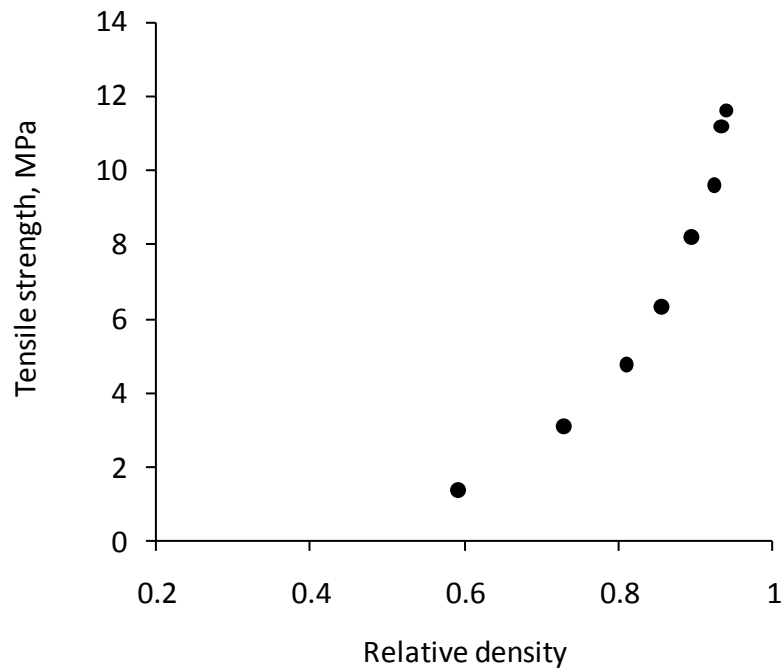


Figure 8-3 Tensile strength – relative density behaviour

The relationship in Figure 8-3 is used to analyse the experimental data for curved faced tablets. For every curved faced tablet the relative density is known and the material tensile strength can be determined using Figure 8-3.

Knowing σ_d , F and the geometric features the experimental data were fitted with equation (8-2) and these coefficients obtained are presented in Table 8-3. It is important to note that these coefficients in Table 8-3 are determined using the results for the curved faced tablets only (Table 8-2). Similar to Pitt's procedure of Pitt et al. (1988), data for flat faced tablets were not included.

Table 8-3 Coefficients for equation (8-2) for curved faced tablets

Compaction pressure, MPa	a	b	c	d
25	0.225	-0.00601	0.079	0.0378
50	0.212	-0.00404	0.119	0.0228
75	0.072	0.0232	0.362	-0.0308
100	0.0975	0.0188	0.316	-0.0233
150	0.0915	0.018	0.419	-0.0377
200	0.184	0.000838	0.238	0.0025
250	0.204	0.00315	0.281	-0.0141
All pressures	0.227	-0.00432	0.117	0.0192

It is important to observe that equation (8-1) or equation (8-2) with the coefficients listed in Table 8-3 does not reduce to the Hertz solution (equation (4-8)) for flat faced tablets. Also it can be observed that the fitting parameters a, b, c, and d in Table 8-3 are different from the equation (8-1). This raises a number of questions regarding the practical application of equation (8-1) or equation (8-2)

- are the coefficients dependent on density (given by compaction pressure)?
- should the equation reduce to the Hertz solution for flat faced tablets?

We will address these issues below. The break force for a tablet compressed to a given density (in other words σ_d is known) normalised with respect to density as follows. A reference force is defined as

$$F_{ref} = \sigma_d * \pi A / 2 \quad (8-3)$$

where A is the cross sectional area of the tablet (the section is from Figure 8-1 (a))

which can be calculated from the geometric features in Figure 8-1

$$A = D^2 \left[2 \left(\frac{t}{D} - \frac{W}{D} \right) \left(\frac{\left(\frac{t}{D} - \frac{W}{D} \right)^2}{16} + \frac{1}{3} \right) + \frac{W}{D} \right] \quad (8-4)$$

The normalised force is then defined as

$$\bar{F} = F / F_{ref} \quad (8-5)$$

The reference force in equation (8-3) is chosen to be a function of material tensile strength and cross section area only. This equation is valid for both flat and curve shaped tablets. For a flat faced tablet, equation (8-3) converges to Hertz solution, in which $A = Dt$ and the normalised force is unity. Essentially the break force of the curved faced tablet is normalised with the break force of a flat faced tablet of the same cross-sectional area and same density. By doing so, the material tensile strength (or density) is eliminated.

Given that out of the three geometric features (t, W and R) only two are independent, a simplified equation is proposed

$$\sigma_d = \frac{F}{\pi D^2} \left(a \frac{t}{D} + b \frac{W}{D} \right)^{-1} \quad (8-6)$$

It is important to note that for the flat faced tablet $t = W$ and if $a+b = 0.5$, equation (8-6) reduces to the Hertz solution equation (4-8).

In fitting the two parameters in equation (8-6) we consider the condition $a+b = 0.5$ in order to ensure that the solution reduces to the Hertz solution for the flat disk.

However, for a better overall fit to the full set of experiments (flat and curved faced tablets) we obtain

$$a=0.167$$

$$b=0.317$$

(8-7)

Here $a+b = 0.484$, implying that there will be a small error for flat faced tablets. The surfaces obtained from equations ((8-1),(8-2) and (8-6)) are plotted in Figure 8-4 in the $t/D - W/D$ space.

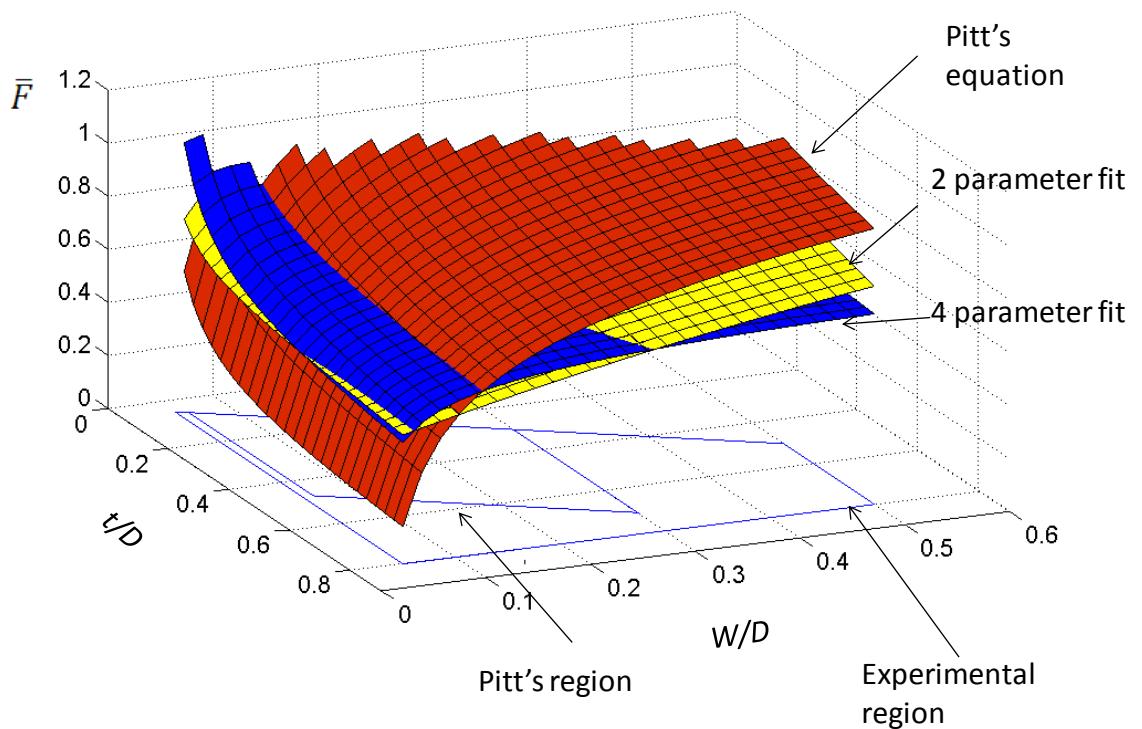


Figure 8-4 Normalised break force calculated using equations ((8-1),(8-2) and (8-6))

For clarity

- The Pitt model represents the break force predicted by the equation of Pitt et al. (1988) normalised using equation (8-5) where the geometry of the tablet is known and σ_d is taken using Figure 8-3 by knowing the density of each tablet.
- The 4 parameter model represents the break force predicted by equation (8-2) normalised using equation (8-5) where the geometry of the tablet is known and σ_d is taken using Figure 8-3 by knowing the density of each tablet. Only curved faced tablets are considered
- The 2 parameter model represents the break force predicted by equation (8-6) normalised using equation (8-5) where the geometry of the tablet is known and σ_d is taken using Figure 8-3 by knowing the density of each tablet. Both flat and curved faced tablets were considered.

Figure 8-4 is convenient to illustrate the normalised break force as a function of the geometric features of the tablets t/D and W/D . In order to compare the three surfaces with the experimental data we return to Figure 8-2 and plot the data along the lines highlighted in Figure 8-2 for shallow, standard, deep, extra deep and ball curvatures as well as along the lines labelled (a) and (b) for a increasing curvatures. These plots are presented in Figure 8-5. The experimental break force data were also normalised using equation (8-5) and σ_d was taken from Figure 8-3.

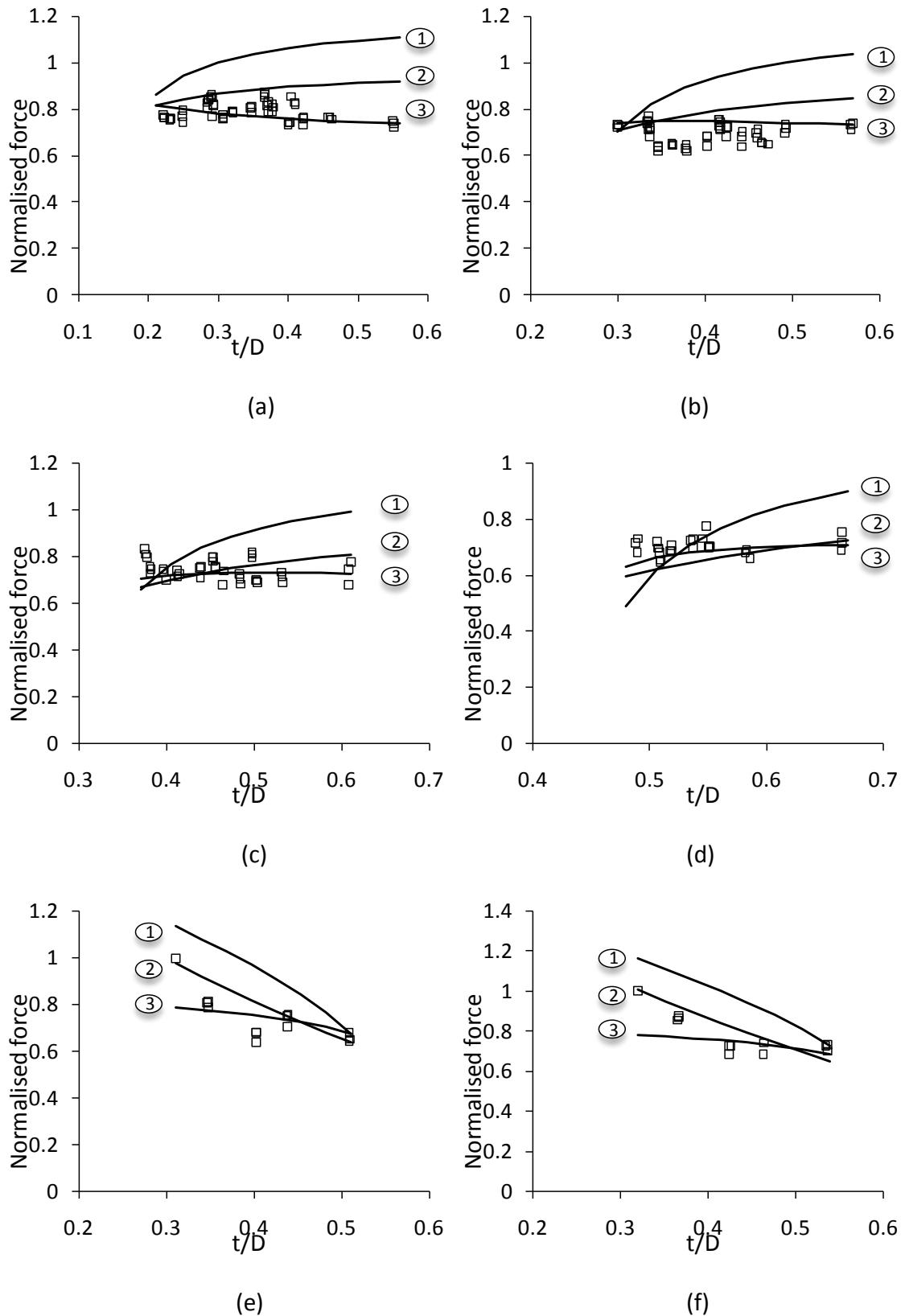


Figure 8-5 Comparison between empirical equations and experimental data : a) Shallow, b) Standard, c) Deep, d) Extra deep concave, e) labelled 'a', f) labelled 'b'. Label 1, 2 and 3 indicates, Pitt's equation, 2 parameter model and 4 parameter model, respectively

It can be observed that Pitt's model generally over-predicts the experimental data. For shallow shaped tablets ((a)), the predicted normalised force curve is well above the experimental data and the maximum error is up to 30%. In Figure 8-5 (b), the force prediction shows an overestimation trend and only gives an accurate value at t/D around 0.3. Similar result can be observed in Figure 8-5 (c) for deep curvature tablets and the precise force prediction occurs at t/D around 0.4. In Figure 8-5 (d), good estimation of force occurs at $t/D=0.55$ for extra deep shaped tablets. In the region of which $t/D < 0.55$, force prediction shows much lower value than experimental results. In the region of which $t/D > 0.55$, the normalised force curve drifts away from experimental results and over-predict the break force.

For all curvatures (Figure 8-5 (a-d)) the 4 parameter model is a better fit to the experimental data than the 2 parameter model; this is because the 4 parameter model does not include data for flat tablets, thus the shape of the surface (Figure 8-4) does not need to pass through the line of unity, which corresponds to flat faced tablets. However, the overall prediction of force by the 2 parameter model gives reasonably good agreement with experimental results.

The break force for flat faced tablets is only visible in Figure 8-5 (e-f) where the two parameter model is consistent with the Hertz solution as $a + b \approx 0.5$. As the Hertz solution is fundamental we propose that the two parameter model (equation (8-6)) is a better representation for both flat and curved tablets.

Finally we examine the breakage behaviour of tablets of different shapes.

Homogeneous thin disks made of linear elastic materials loaded across the diameter

will develop a uniform tensile stress state between the loading points (Hertz solution); thus brittle materials will break as illustrated in Figure 8-6 (picture labelled “a”).

Curved shaped tablets, particularly having “deep” curvatures Figure 8-6b break in a more complex pattern while “extra deep” and “ball” shaped tablets present delamination (Figure 8-6 (c-e)). Tablets which have different failure mechanism are labelled by solid markers. Photos of breakage of those tablets are also provided.

As can be seen in the Figure 8-6, the tablets which fail due to complex mechanism lay on the right hand side of the line $t/D=0.45$. The typical failure pattern of these tablets is illustrated by photos (b)-(e) in Figure 8-6. As shown by photos (b) and (e), primary crack induced by tensile stress and secondary crack appeared on the band width can be observed. Photo (c) shows that the tablet delaminates and a secondary crack appear on the far side of the curve surface which opens the surface. In photo (d) the ball shape tablet totally delaminates.

All the different failure patterns of tablets illustrated are due to a complex mechanism which takes effect during diametrical compression test. The cause for complex failure patterns is multiple and we discuss the following three: stress state, material inhomogeneity, and defects.

First, the stress state in thin flat disks can be determined using the relationships developed by Hertz, which led to equation (4-8). For curved faced tablets analytical solutions do not exist, however, the stress state was examined experimentally by Pitt et al. (1989b) using photoelastic techniques. They observed tensile stresses in the direction of the thickness of the specimen for $D/R = 1$ (which corresponds to “deep” curvatures), however, the stress in this direction was compressive for other curvatures

analysed. The stress state for flat disks was examined using finite element analysis by Procopio et al. (2003) considering not only elastic but also plastically deforming materials and the stress states were found complex even for flat disks.

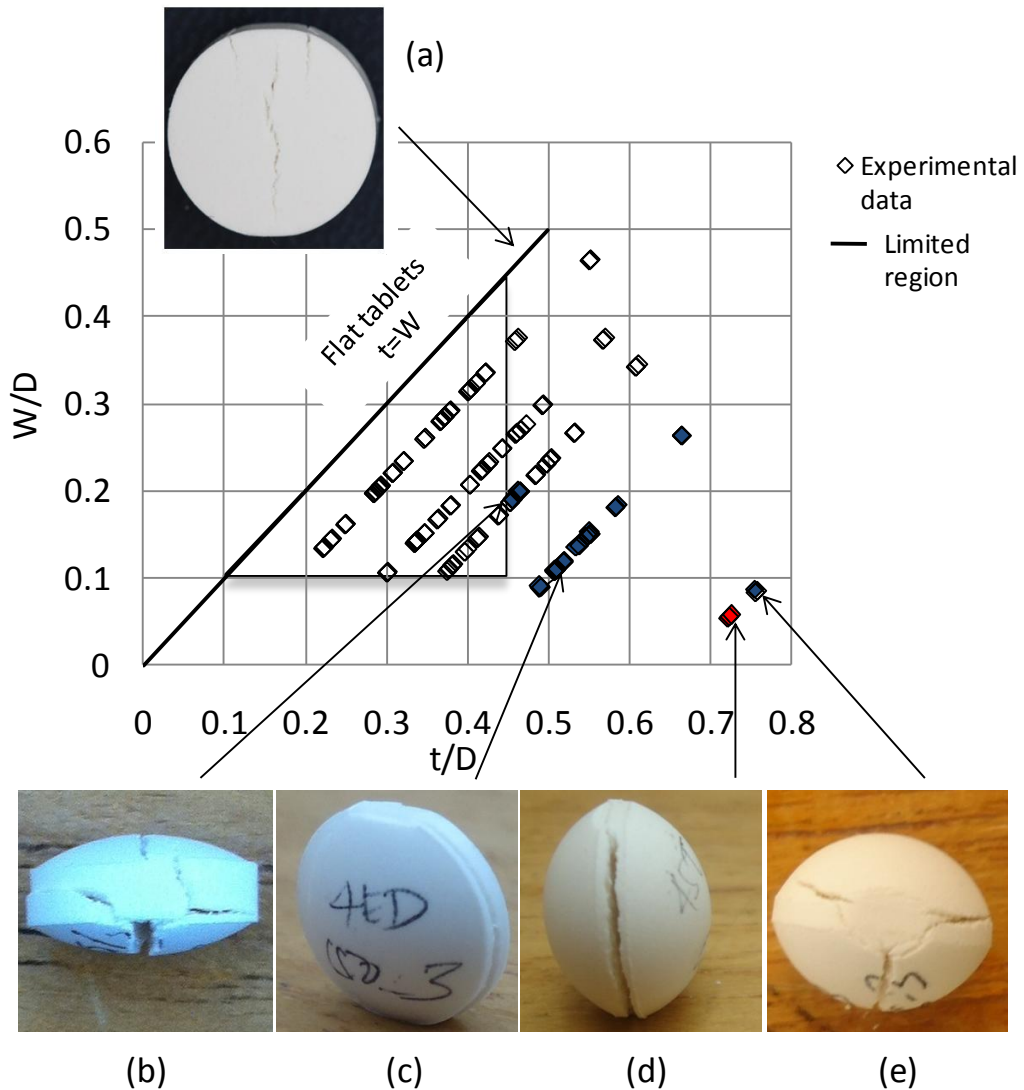


Figure 8-6 Tablets fail due to complex failure mechanism. Red solid marker indicates that the tablets totally laminate. Blue solid marker indicates that tablets fails in a way both delimitation and breaking into halves may be observed. Photos (b)-(e), tablets were compacted under maximum pressure: 250, 150, 50 and 25 MPa using powder weight: 400, 400, 450 and 400 mg.

Second, pharmaceutical tablets are inhomogeneous. Density distributions can be observed using a variety of experimental methods, including indentation hardness mapping (Sinka et al., 2003), X-ray computed tomography (Sinka et al., 2004b), NMR imaging (Djemai and Sinka 2006). Sinka et al. (2004a) showed that identical curved faced tablets (material, shape and density) can be pressed under conditions that produced different internal density distributions and that these seemingly identical tablets fail differently, e.g. delaminate (similar to Figure 7d) or break in two (similar to the flat faced tablet in Figure 8-6a) depending on the internal density distribution. The break force itself is dependent on the internal density distribution (Sinka et al., 2004a).

Third, the potential influence of inherent defects was suggested in early papers (Pitt et al., 1989, Hariran and Newton 1999). Wu et al. (2008) found laminations in tablets using X-ray computed tomography. It can be assumed that these flaws and the distribution of flaws would have a significant effect on tablet strength, however, a comprehensive analysis has not been published to date.

Figure 8-6 illustrates that the failure mode (breakage, delamination) is affected by the geometry of tablets. Given the discussion above, the experimental space was limited. Those tablets which show different breaking behaviour are removed from the geometry map so that a tensile stress induced breakage is ensured similar to flat faced tablets. In addition to failure mode, some of the tablets in the experimental space defined by t/D and W/D in Figure 8-6 have unusual aspect ratio for typical pharmaceutical tablets that are commercialised. For example, t/D is too large (the tablet is too thick) or W is too small (can create manufacturing problems in terms of driving the compression punches together). The reduced triangular area in Figure 8-6

corresponds to tablets of more usual geometry. Using the experimental data in this limited area the two parameter model (equation (8-6)) was re-calibrated

$$a=0.14$$

$$b=0.36 \tag{8-8}$$

In this case $a + b = 0.5$ thus equation (8-6) reduces to Hertz solution for flat disks.

While the surface of normalised break force does not differ significantly from the results in equation Figure 8-7, the parameters are determined for more realistic shapes. The normalised break force surface is illustrated in Figure 8-7 together with experimental data for comparison. Figure 8-7 also illustrates the geometries (t/D and W/D) for which the 2 parameter model (equation (8-6)) could be used.

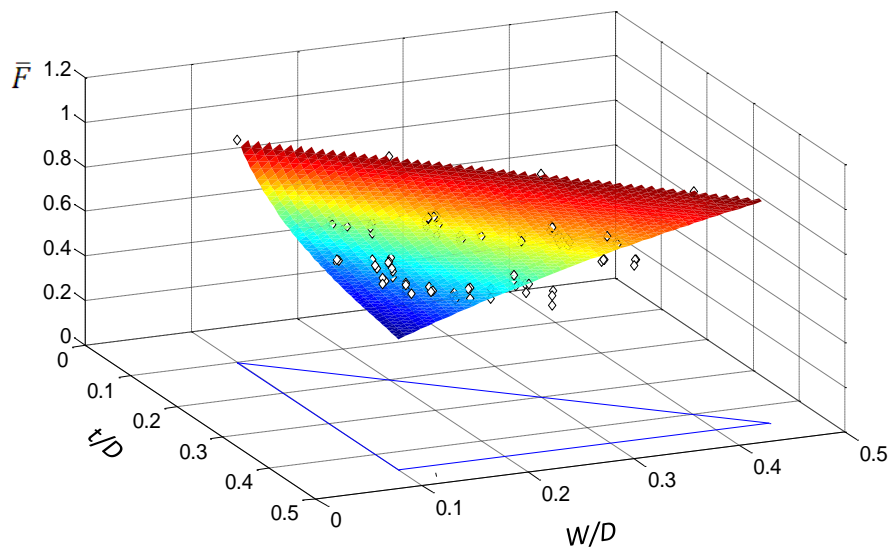


Figure 8-7 Normalized break force surface using two-parameter model fit experimental data in limited region ($0.1 < t/D < 0.45$, $0.1 < W/D < 0.35$).

8.4 Conclusions

This chapter presents an extensive set of diametrical compression experiments on curved faced tablets. The only existing model for the break force of curved faced tablets was re-evaluated and simplified. The application space of the new two parameter model that was proposed was established in terms of failure mode and realistic tablet geometries.

The 2 parameter model (equation (8-6)) with the parameters given in equation (8-8) was proposed to determine the break force of curved faced tablets. Equation (8-6) has the advantages that the break force converges to the solution for flat faced tablets.

Chapter 9. Numerical analysis of tablet breakage

9.1 Introduction

During the diametrical compression test, a tensile stress perpendicular to the compressed diameter is induced, which is constant over a wide region around the centre of the disc. The tensile strength is calculated on the assumption that failure initiates at the point of maximum tensile stress. In this chapter a numerical method to predict the break force of tablets is proposed as an alternative to empirical approaches. A constitutive model and a failure criterion are selected and validated against experimental data from Chapter 8. The conditions for practical applicability are identified. The predictive method presented in this chapter is based on first principles and can be used to assist rational tablet formulation design and process development.

9.1.1 Stress distribution of diametrical compression test

The theoretical basis of a thin flat disc subjected to two concentrated diametrical forces was developed by Hertz (1895). The stress state at a point in the disc (Figure 9-1a) can be calculated using the following equations

$$\sigma_x = \frac{-2F}{\pi t} \left\{ \frac{x^2(R-y)}{\beta_1^4} + \frac{x^2(R+y)}{\beta_2^4} - \frac{1}{2R} \right\} \quad (9-1)$$

$$\sigma_y = \frac{-2F}{\pi t} \left\{ \frac{(R-y)^3}{\beta_1^4} + \frac{(R+y)^3}{\beta_2^4} - \frac{1}{2R} \right\} \quad (9-2)$$

$$\sigma_{xy} = \frac{2F}{\pi t} \left\{ \frac{x(R-y)^2}{\beta_1^4} + \frac{x(R+y)^2}{\beta_2^4} \right\} \quad (9-3)$$

where $\beta_1^2 = (R - y)^2 + x^2$, $\beta_2^2 = (R + y)^2 + x^2$, F is the break force, R is the radius, t is the thickness, σ_x and σ_y are the normal stresses in the directions perpendicular and parallel to the loading direction, respectively, and σ_{xy} is the shear stress, see Figure 9-1 (a).

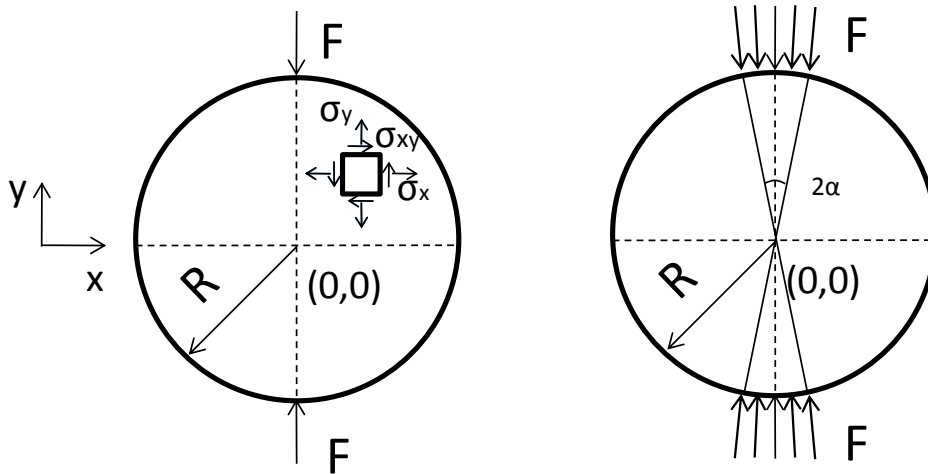


Figure 9-1 The diametrical compression test (a) Point loading condition, (b) Hondros distributed loading condition

Along the diameter ($x=0$), σ_x is reduced to

$$\sigma_x = \frac{2F}{\pi Dt} \tag{9-4}$$

Equation (9-4) is in effect the same as the equation (4-8) given in Chapter 4. The details of the stress analysis that provide equation (4-8) are given in this section.

At the centre of the specimen, equation (9-2) is reduced to

$$\sigma_y = -\frac{6F}{\pi Dt} \tag{9-5}$$

Therefore, the compressive strength must be at least three times the tensile strength to ensure a tensile failure according to equation (9-4) and (9-5).

The Hertz solution was later modified by Hondros (1959). He proposed a theory for a distributed loading condition on the specimen (see Figure 9-1 (b)). The stress of Hondros solution along $x=0$ and $y=0$ respectively is given by

$$\begin{aligned} & \sigma_x(0, y), \sigma_y(0, y) \\ &= \pm \frac{2F}{\alpha\pi Dt} \left\{ \frac{\left(1 - \frac{r^2}{R^2}\right) \sin 2\alpha}{1 \mp \frac{2r^2}{R^2} \cos 2\alpha + \frac{r^4}{R^4}} \right. \\ & \quad \left. \mp \tan^{-1} \left(\frac{1 \pm \frac{r^2}{R^2}}{1 \mp \frac{r^2}{R^2}} \right) \tan \alpha \right\} \end{aligned} \quad (9-6)$$

$$\begin{aligned} & \sigma_x(x, 0), \sigma_y(x, 0) \\ &= \mp \frac{2F}{\alpha\pi Dt} \left\{ \frac{\left(1 - \frac{r^2}{R^2}\right) \sin 2\alpha}{1 \mp \frac{2r^2}{R^2} \cos 2\alpha + \frac{r^4}{R^4}} \right. \\ & \quad \left. \pm \tan^{-1} \left(\frac{1 \pm \frac{r^2}{R^2}}{1 \mp \frac{r^2}{R^2}} \right) \tan \alpha \right\} \end{aligned} \quad (9-7)$$

$$\tau_{xy}(0, y), \tau_{xy}(x, 0) = 0 \quad (9-8)$$

where r is the radial distance of one point to the centre (0,0).

The advantage of Hondros' theory is that the compressive stress at the point of $y=R$ is finite. At the centre of the disc stress in x axis is

$$\sigma_x(0,0) = \frac{2F}{\pi Dt\alpha} (\sin 2\alpha - \alpha) \quad (9-9)$$

for small α , $\sin 2\alpha \approx 2\alpha$

$$\sigma_x(0,0) = \frac{2F}{\pi Dt} \quad (9-10)$$

Equation (9-4) and (9-10) suggest that in the middle of the specimen both theories are in agreement. Significant amount of work related to Hondros loading condition has been carried out. The use of shaped platen (Awaji and Santo, 1979 and Davies et al., 2007) and grinding of the contact surfaces (Farhad, 1996) are the main methods used to study the change of the loading and boundary condition on the tensile strength prediction.

Although the analytical solution for diametrical compression test is available, in practice the loading condition is different from point or finite arc loading. For instance, the thin disk is placed in between two flat platens, as the loading is increased the contact region flattens. Such phenomenon changes the stress distribution within the tablet (Procopio et al., 2003).

For more complex shaped pharmaceutical tablets (e.g. oval or elongated shape), it is proposed that a different approach from Hertz solution must be adopted (Stanley and Newton, 1977). For example, the equation (8-1) developed by Pitt based on experiments of curved faced tablets was extended to elongated shapes using a simple numerical procedure (Pitt and Heasley, 2011). Generally, for a complex shape, the fracture stress is not available analytically. However, the stress analysis can be facilitated with numerical (e.g. FEM) or experimental (e.g. photoelastic technique)

methods (Durelli and Riley, 1965, Stanley and Newton, 1977, Pitt et al., 1989b).

Numerical modelling of tensile strength has been employed in the past twenty years (Farhad, 1996, Procopio et al., 2003, Mates et al., 2008). The FEM was used to analyse the stress distribution of diametrical compression test (Price and Murray, 1973 and Procopio et al., 2003).

9.1.2 X-ray CT characterisation of tablet structure

To observe the breakage of the tablets, the X-ray computed tomography method (X-ray CT) is employed using a X-TEK 225 system (now trading under Nikon, UK). X-ray CT is non-destructive technique that can be used to visualise the internal structure of material. This technique involves collecting radiographs as the sample is rotated 360 degrees in small increments. The two-dimensional images are then reconstructed mathematically to provide structure information in 3D. By using this method, the internal structure of tablets has been observed e.g. density distributions (Sinka et. al., 2004) and cracks (Wu et. al., 2005).

9.2 Numerical procedure

The finite element software ABAQUS/Standard was used to simulate the diametrical compression test. Three-dimensional (3D) static stress analysis is performed for flat faced and curved faced tablets using 8-node linear brick type of elements (C3D8). One quarter of the tablet is modelled for symmetry reasons. Figure 9-2 shows the mesh of the tablets.

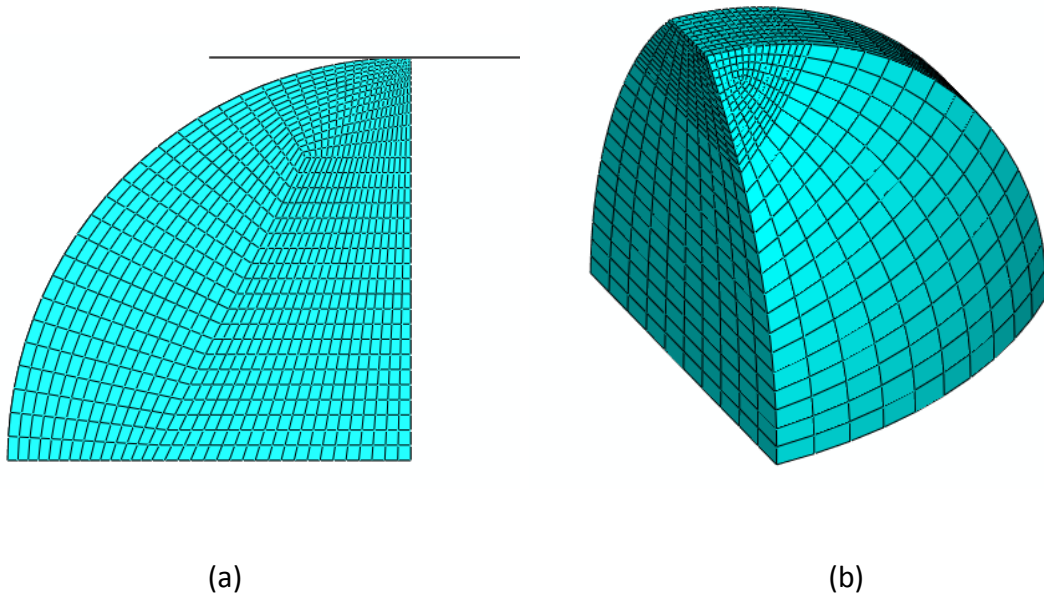


Figure 9-2 Finite element mesh during diametrical compression test simulation a) flat faced and b) curved faced tablets.

The platen is simulated as a rigid body and the interaction between the platen and the tablet is considered frictionless. Compression is simulated by applying displacement boundary conditions to the platen. The analysis of break force is done for the range of tablet shapes presented in Table 9-1.

The discussion in this chapter is performed using microcrystalline cellulose as example powder material. The characteristics of this powder are given in Chapter 4 (Section 4.1.3)

Table 9-1 Geometry and initial density for simulations

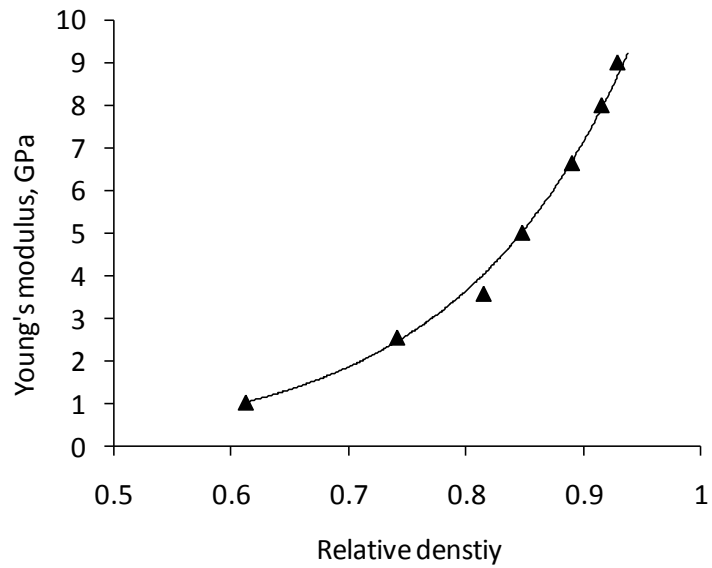
Geometry	Diameter (D), mm	Radius (R), mm	Band width (W), mm	Thickness* (t) mm	Initial RD
Flat	10.5	infinity	2.75	2.75	0.6~0.94
Curve faced	10.5	42	1.575	2.23	0.84
		21		2.91	
		15.67		3.39	
		10.5		4.39	
	10.5	42	2.1	2.76	0.84
		21		3.43	
		15.67za\		3.91	
		13.125		4.29	
	10.5	42	3.15	3.81	0.84
		35		3.94	
		26.25		4.21	
		21		4.48	

* t is calculated from R and W

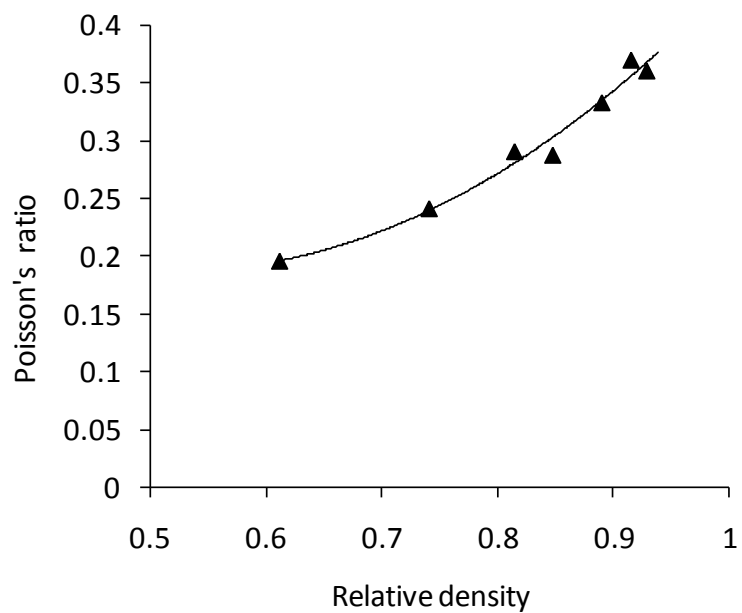
9.2.1 Constitutive model

Two constitutive models are used

1. Linear elastic model. The elastic properties (Young's Modulus E and Poisson's ratio ν) determined experimentally as described in Chapters (Chapter 4 and Chapter 6) are functions of relative density as shown in Figure 9-3. When the linear elastic model is employed, the elastic parameters are constant, corresponding to the relative density that is being analysed.



(a)



(b)

Figure 9-3 Elastic properties as function of relative density, a) Young's modulus, b) Poisson's ratio

2. Drucker-Prager Cap (DPC) model with density dependent parameters. Figure 9-4 presents a family of Drucker-Prager cap surfaces corresponding to different levels of relative density. The material parameters of the DPC model evolve with the

relative density. To describe elastic behaviour, Young's modulus and Poisson's ratio are considered also dependent on relative density as presented in Figure 9-3. The material parameters used in DPC model are listed in Appendix B, Table B.1.

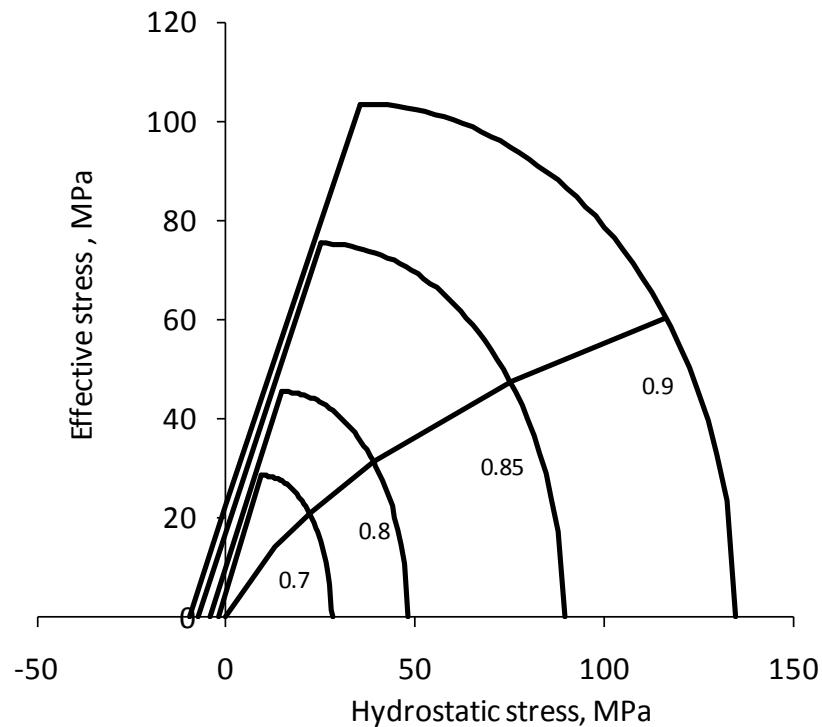


Figure 9-4 Drucker-Prager cap surfaces, the labels indicating relative density

The break force of flat faced tablets is simulated for a range of relative densities $RD=0.6\sim0.94$ (Table 9-1). For curved faced tablets a fixed initial relative density $RD=0.84$ is selected, as the geometry factor is the concern. When the DPC model is used the density distribution in the tablet is assumed uniform, thus the elastic and plastic model parameters are the same at every point in the body. This model however allows densification to take place due to the loading conditions and the material parameters are changing as function of relative density as illustrated in Figures 3-4.

When the linear elastic model is used the elastic properties are fixed according to the density (e.g. when $RD=0.84$, $E=5.2\text{GPa}$ and ratio is $\nu=0.3$). When the DPC model is used all material parameters are defined as functions of relative density as illustrated Table B.1.

9.2.2 Failure criteria

Three failure criteria are considered to predict the break force

1. Criterion 1: Maximum principal stress (used with the linear elastic model).

When the maximum principal stress within an element along the diameter reaches the material tensile strength, the reaction force of the platen is regarded as the break force of the tablet.

2. Criterion 2: Maximum principal stress (used with the variable DPC model).

Similar to criterion 1, when the maximum principal stress within an element along the diameter reaches the material tensile strength the reaction force of the platen is regarded as the break force of the tablet.

3. Criterion 3: Fully developed shear failure zone (used with the variable DPC model). As the load is increased, elements across the diameter start yielding on the shear failure line. The tablet is considered failed when the shear failure zone propagates to the centre of the tablet.

The maximum stress criterion also known as the normal stress, Coulomb, or Rankine criterion is often used to predict the failure of brittle materials. It states that failure occurs when the maximum principal stress reaches a critical stress level (tensile strength). The tensile strength of the material depends on the relative density. For example, for the density range employed in modelling the break force of flat faced

tablets the tensile strength is in the range of 1.35MPa to 10.47 MPa. For RD = 0.84, $\sigma_d = 6.4$ MPa.

9.3 Results and discussion

The analysis of the break force of flat and curved face tablets is presented below.

9.3.1 Flat faced tablet

Figure 9-5 illustrates the application of the three failure criteria for the analysis of flat faced tablets with an initial relative density of 0.84. Figure 9-5 (a) and (b) shows the maximum principal stress state within the tablet using linear elastic model and DPC model. The elements in the grey region suggest that the tensile stress of these elements exceed the tensile strength of the material. Figure 9-5 (c) highlights the area where elements (red region) developed along the centre of the specimen yield on the shear failure line. In Figure 9-5 (a), the first element which reaches the maximum principal stress appears at the centre of the tablet. The effects of local deformation around the contact points are not considered. In Figure 9-5 (b), the distribution of maximum principal stress suggests that the location of the first element which reach the material tensile strength is at somewhere in between the loading point and centre of the specimen. The element where the maximum principal stress exceeds the material tensile strength is considered as the location of the initiation of the crack.

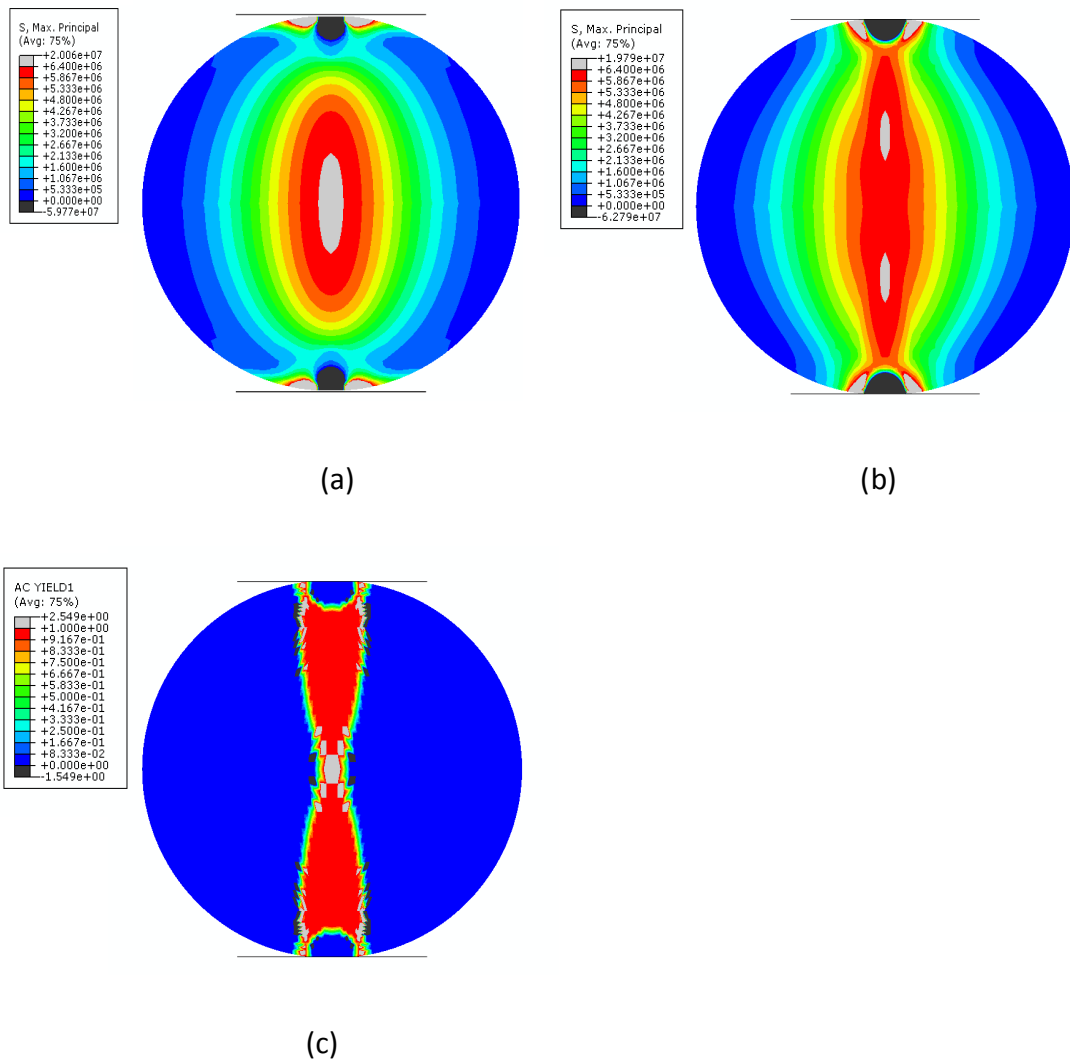


Figure 9-5 Diametrical compression test simulation of flat faced tablet using 3 failure criteria:

(a) criterion 1, (b) criterion 2, (c) criterion 3

Using the above criteria the break force for flat faced tablets is established using the following method. The analysis generates the reaction force at the loading platen which is plotted with respect to the displacement of the platen as shown in Figure 9-6. The maximum principal stress distribution is examined. The break force is taken when criterion 1 is satisfied as the linear elastic constitutive model is used. When the DPC

model is used a different force-displacement curve is generated (Figure 9-6) as the DPC model allows plastic deformation at the contact point, which leads to local densification. During the test, force-displacement curve on the loading platen is constantly recorded. When the failure occurs, corresponding displacement and force on the loading platen are obtained. For instance, as shown in Figure 9-6, the force-displacement of Figure 9-5 is presented and the solid markers indicate the breaking force under the specific displacement of loading punch.

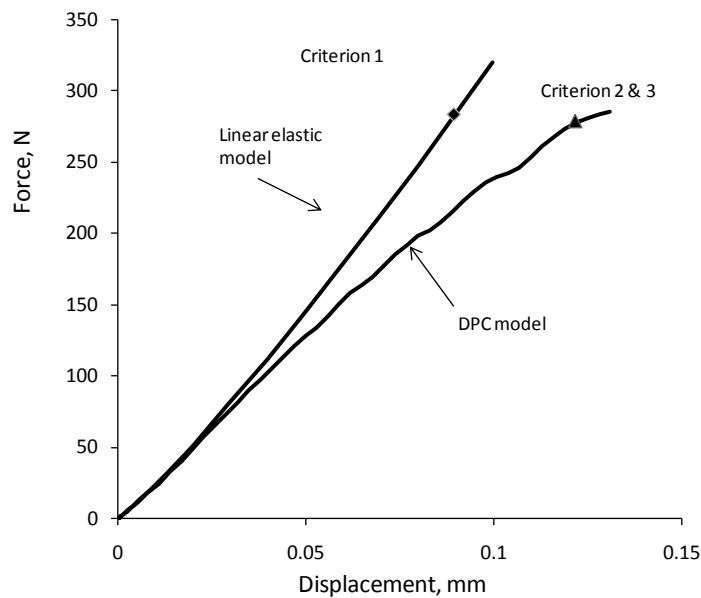


Figure 9-6 Force displacement curve of 3 failure criteria at RD=0.84 of flat faced tablet

The predicted break force using the 3 failure criteria give approximately the same force value. When DPC model is applied the break force prediction using criterion 2 and 3 gives exactly the same result for this particular relative density. The similarity of break force prediction using all three failure criteria is valid for all densities. The tensile

strength, using the Hertz solution (equation (4-8)) is plotted with respect to relative density in Figure 9-7.

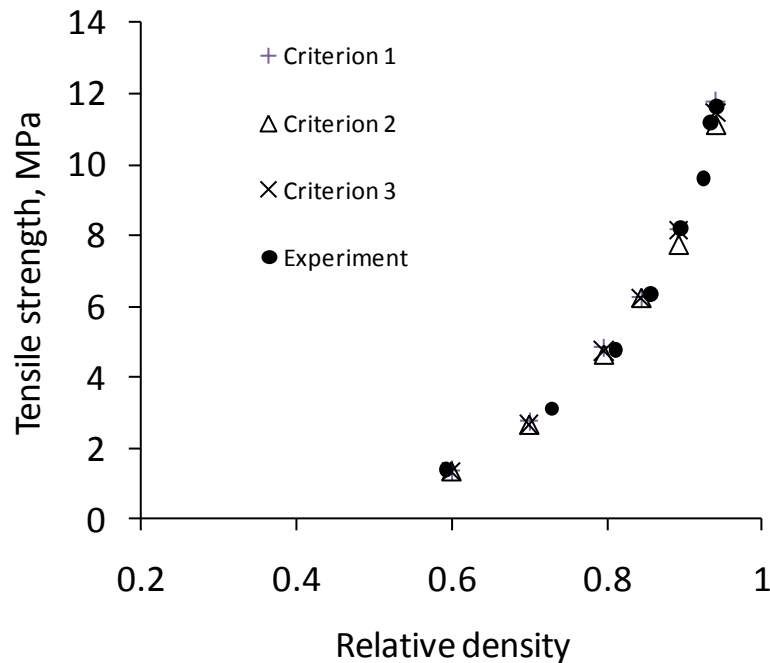


Figure 9-7 Tensile strength of experimental data and prediction of 3 failure criteria

As shown in Figure 9-7, all three failure criteria are in good agreement with each other and with the experimental data. However, finite element analysis provides further insight. Tensile stresses develop not only in the centre of the tablet but also in the region of contact between tablet and platen as shown in Figure 9-5 (a-b). The flattening of the contact area is captured by the DPC model. In this area plastic deformation leads to further densification (Figure 9-8a). Elements in this region reach the material strength before the elements along the diameter where the initial crack initiates. Therefore the stresses near the contact region are not considered when the failure criteria 1-2 are applied.

Along the centre of the tablet where tensile stresses are developed and the material yields along the failure surface, the model predicts dilation because the flow rule is non-associated. These effects are also shown in Figure 9-8a.

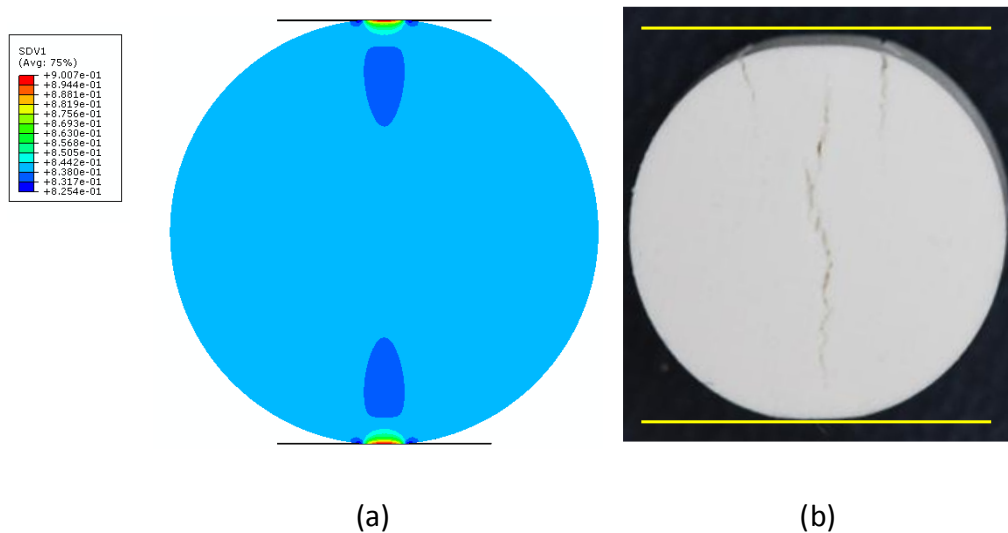


Figure 9-8 a) density at contact point, b) photo

Figure 9-8b shows the contact region for a tablet made of MCC, relative density $RD=0.854$ and thickness 2.285 mm. In addition to contact flattening, one can observe secondary cracks, which are observed experimentally (Rudnick et al., 1963, Jonsen et al., 2007, Mates et al., 2008). Procopio et al. (2003) identified that the crack initiates at a point along the loading direction just under the densified zone. This is consistent with the model prediction Figure 9-5b. Cracks will then propagate to form a continuous diametrical crack.

Although all three failure criteria predict the same break force, the stress states between linear elastic and DPC models are different. In the next section we examine

the applicability of the models and failure criteria to predict the break force of curved faced tablets.

9.3.2 Curved faced tablet

The geometry of curved faced tablets is defined in Figure 8-1. The experimental data used in the development of the empirical equation (8-6) is presented in Figure 9-9 in the $t/D - W/D$ space. Flat faced tablets ($W = t$) lie on the bisector of the plane. Convex faced tablets are located only at the right hand side of this line. The validity of Pitt's empirical relationship equation (8-1) is indicated in Figure 9-9. The geometries considered for numerical analysis (Table 9-1) are presented alongside the experimental data points in Figure 9-9.

Later in this chapter the applicability of numerical modelling will be limited to the area highlighted in Figure 9-9. This limited region is selected by considering realistic tablet shapes and excluding tablets with thin band area (W) which may present complex breakage mechanisms. The details of limiting the modelling space for the purpose of fitting surfaces will be described in Section 9.3.3.

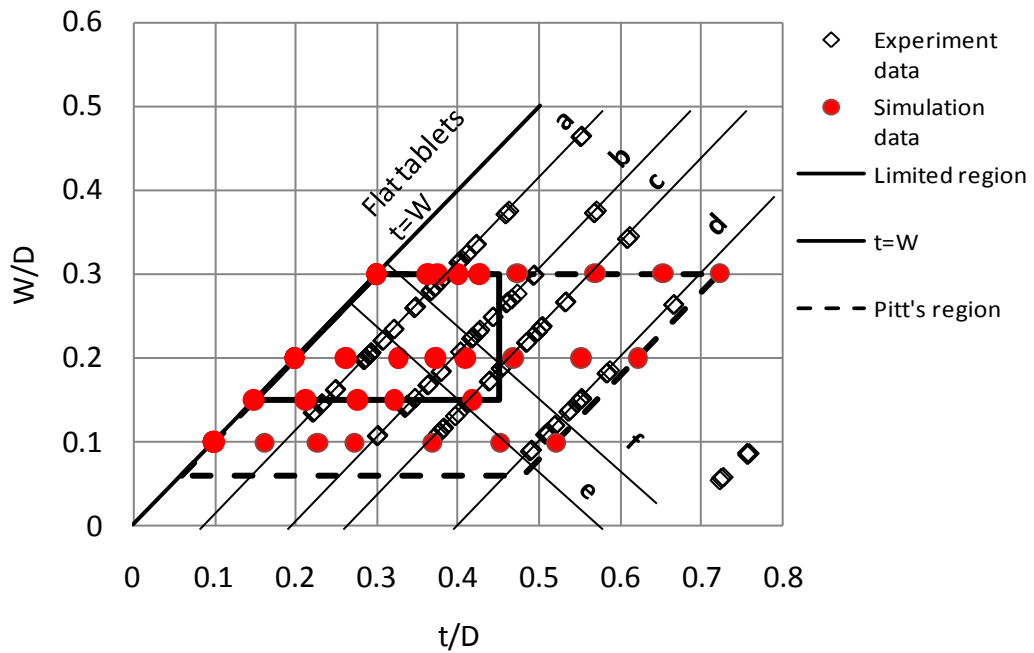


Figure 9-9 Simulation and experimental data

To identify the breaking force, the force-displacement curve needs to be obtained. Take one geometry ($W=1.575\text{mm}$, $t=2.91\text{mm}$) of tablet for example. In order to compare the break force of tablets of various shapes normalization is carried out as described by equations (8-3)-(8-5)).

The break force corresponding to each of the three failure criteria is identified from Figure 9-10. It is interesting to observe that due to the normalisation method the break force for the linear elastic model and Criterion 1 can be higher than unity. For the DPC model the force-displacement curve determined numerically is unique and the application of criterion 2 and 3 will give two different values of the break force:

criterion 2 corresponds to first yield which occurs earlier than a fully developed plastic zone for criterion 3.

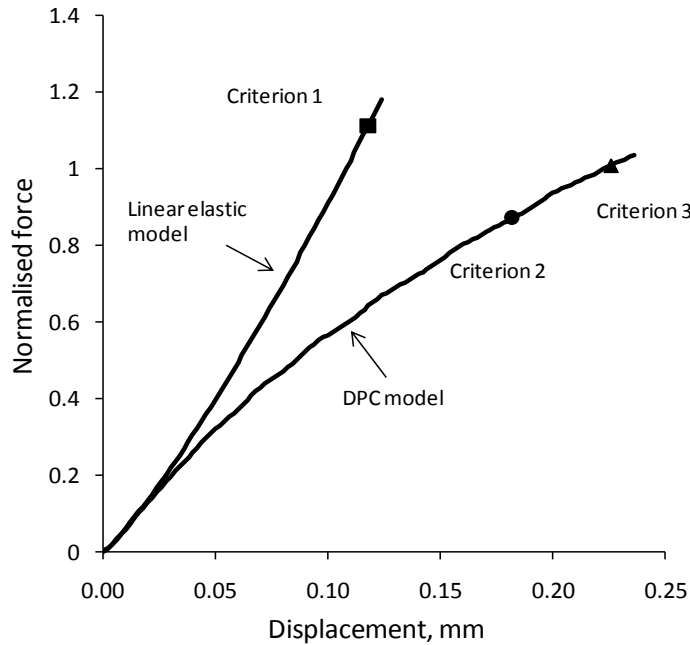


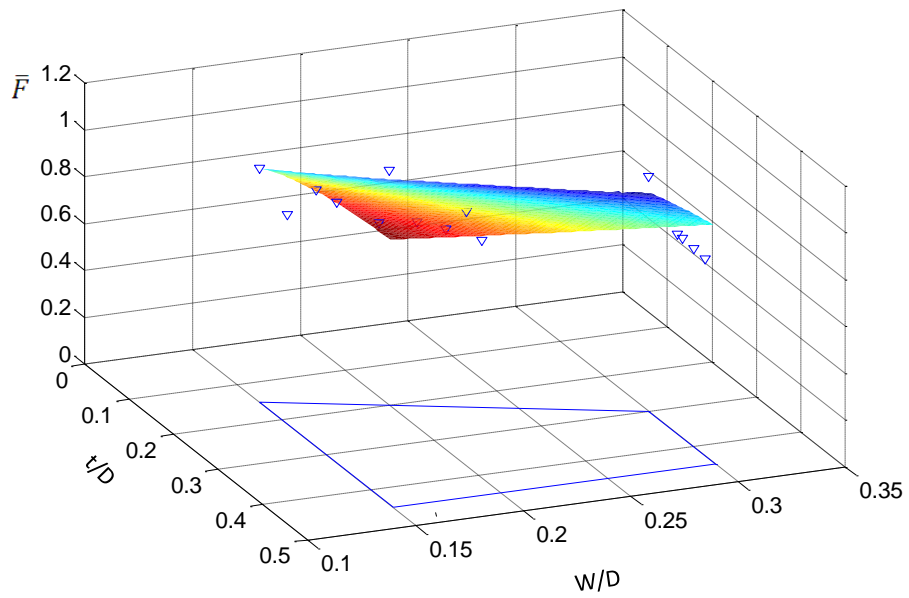
Figure 9-10 Normalised force displacement curve of 3 failure criteria at RD=0.84 for curved faced tablet with a geometry ($W=1.575\text{mm}$, $t=2.91\text{mm}$)

The normalised forces using the 3 failure criteria are plotted as functions of t/D , W/D in Figure 9-11 (a),(b) and (c) for an initial density of RD=0.84. In Figure 9-11 (a) criterion 1 is applied and the normalised force have a range of 0.9~1.2. In Figure 9-11 (b), the predicted force using criteria 2 lies in a range of 0.6~1. In Figure 9-11 (c) an estimated force using criteria 3 gives almost constant force prediction of around 1.

The coefficients are provided in Table 9-2.

Table 9-2. Coefficients using equation (8-6) for experimental data and 3 failure criteria

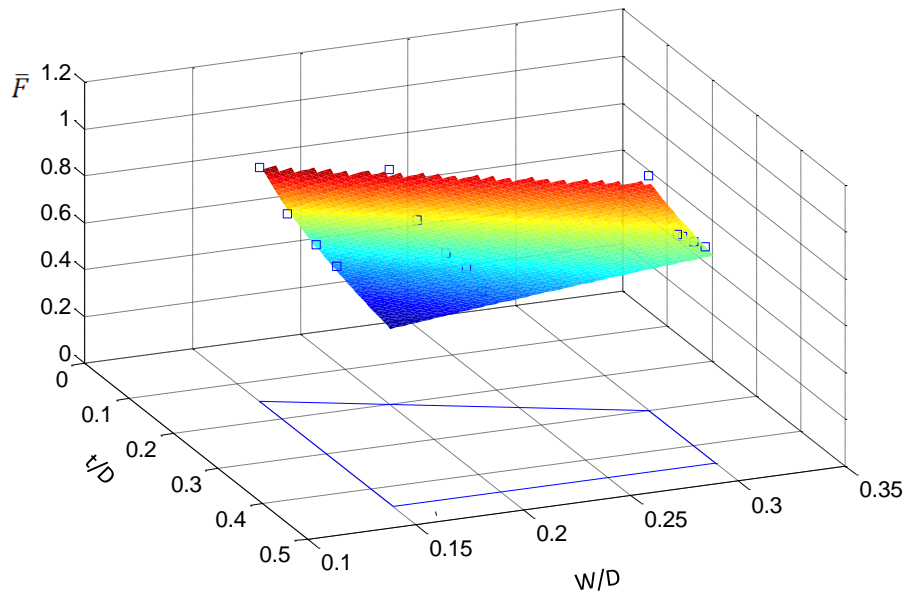
RD084	a	b
Criterion 1	0.419	0.016
Criterion2	0.187	0.284
Criterion 3	0.323	0.162
Experiment (Shang's fit)	0.14	0.36



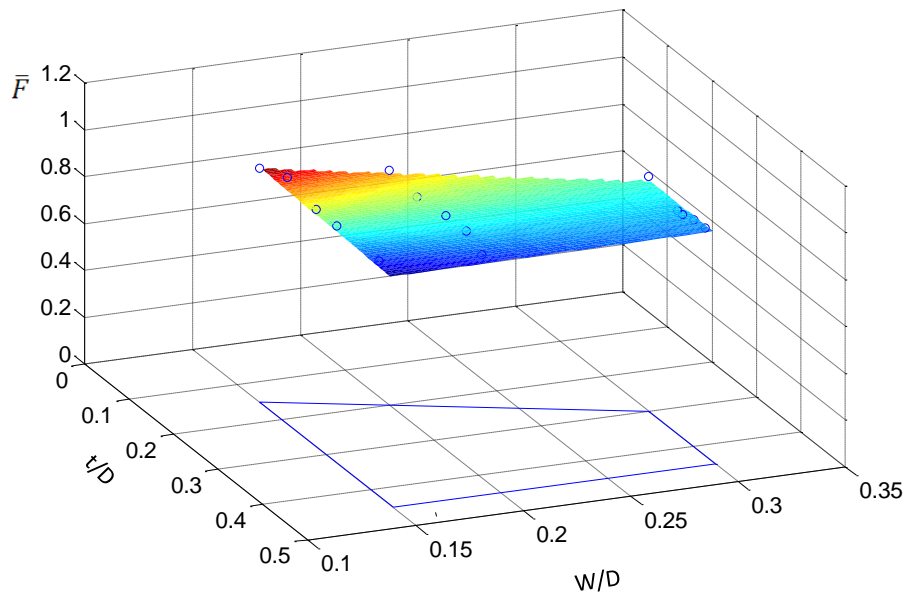
(a)

Figure 9-11 Surface fitted to simulation data points using 3 failure criteria (a) Criterion 1, (b)

Criterion 2, (c) Criterion 3



(b)



(c)

Figure 9-11 (Continued)

In order to compare the force prediction using 3 failure criteria, Pitt's equation and the experimental data are plotted in Figure 9-12.

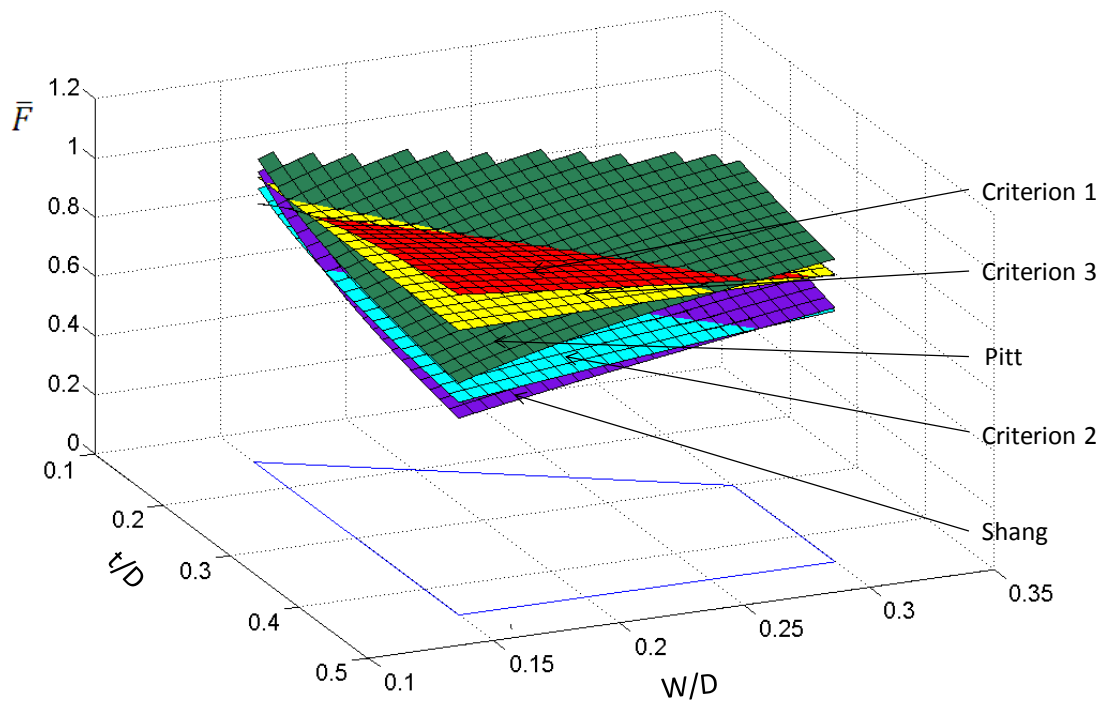


Figure 9-12 Normalized force surfaces in 3D verse the geometry factor t/D , W/D

Figure 9-12 suggests that Criterion 2 is closer to the experimental data than the other two criteria and Pitt's equation. For a more detailed examination the five surfaces are sectioned alongside the lines (a-f) labelled in Figure 9-9 and the curves are plotted in Figure 9-13.

It can be observed that Criterion 2 is a better representation of the experimental data by using equation (8-6). While criterion 1 and criterion 3 over-predict the break force. It

is also important to note that the three failure criteria and the experimental data are fit using equation (8-6) by including flat faced tablets.

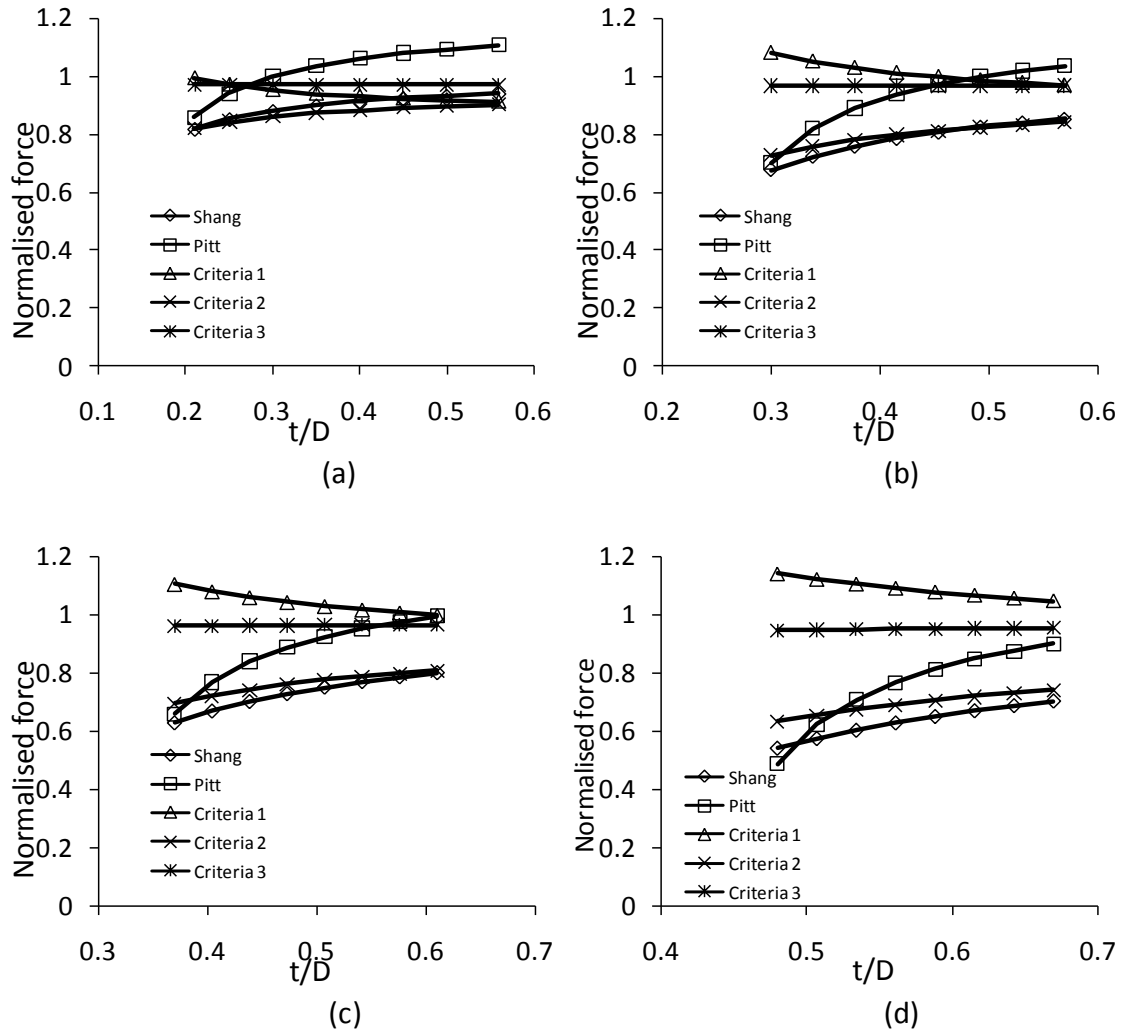


Figure 9-13 Comparison between empirical equations and failure criteria: a) Shallow(labelled 'a'), b) Standard (labelled 'b'), c) Deep (labelled 'c'), d) Extra deep concave (labelled 'd'), e) labelled 'e', f) labelled 'f'.

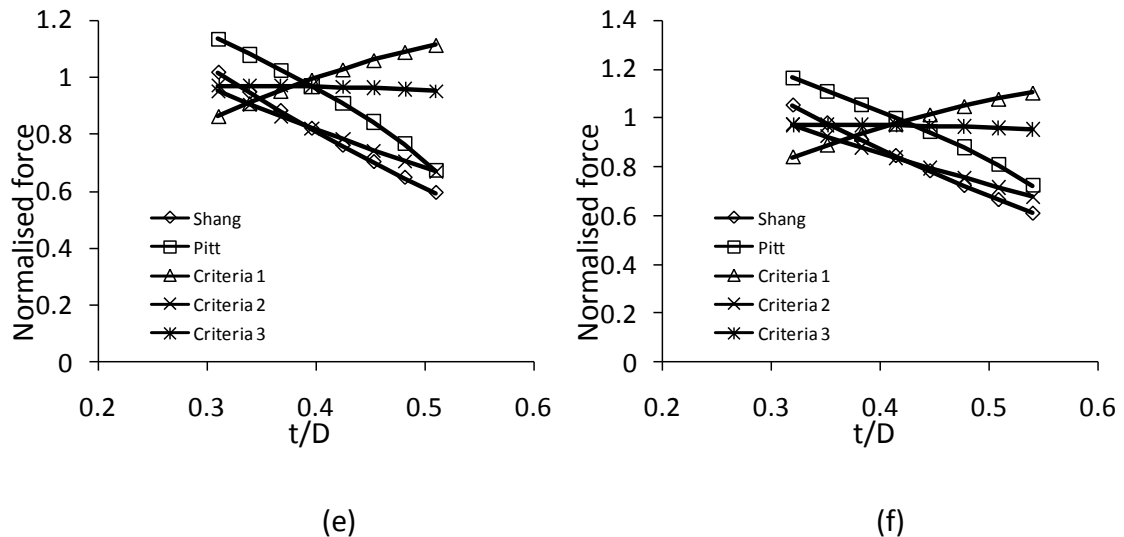


Figure 9-13 (Continued)

9.3.3 Failure mode

A limited region of simulation data is presented in Figure 9-9. This limited region is defined by $0.15 < W/D < 0.3$ and $t/D < 0.45$ using the following considerations

1. For $W/D > 0.3$ the tablet is considered to have a band width which is too wide.
2. For $t/D > 0.45$ the aspect ratio is not consistent with typical pharmaceutical tablets (the thickness is too large). In addition to these geometries the failure patterns observed experimentally are more complex than those of flat disks and can include delimitations as illustrated in Figure 9-14. In Figure 9-14a and b, beside the main failure plane across the diameter, cracks appear in the band width area near the loading platen. Such breakage (Addinall and Hackett, 1964) suggests that tensile stress distributions are different from the Hertz solutions.
3. For $W/D < 0.15$ the numerical model shows stress states are more likely to produce delaminations than breakage of tablets across the loading points as in the case of flat disks. In Figure 9-15, the stress analysis of the sample ($D/R=0.67$, $W/D=0.1$) is provided using DPC model. The elements in the grey region just

under the densification zone near the loading boundary reach the material tensile strength and subject tensile stress in “y” direction (break into layers/laminate). The failure pattern of tablets is examined non-destructively in 3D using X-ray CT. The failure patterns inside shallow and ball shaped tablets are presented in Figure 9-16 and Figure 9-17, respectively. It can be seen in x-y plane (Figure 9-16b) and offset plane (Figure 9-16d) that a crack which is different from the major crack in x-z plane (Figure 9-16a) develops from the loading boundary. This is consistent with the simulation result as shown in Figure 9-15 showing the tensile stresses that lead to crack initiation in this direction.

Therefore, to avoid the breakage due to different mechanism, the applicability region is further restricted to $0.15 \leq W/D \leq 0.3$ and $0.15 \leq t/D \leq 0.45$ whereby tablets fail due to tensile stress in z direction (break into half) according to simulation and experiment results.

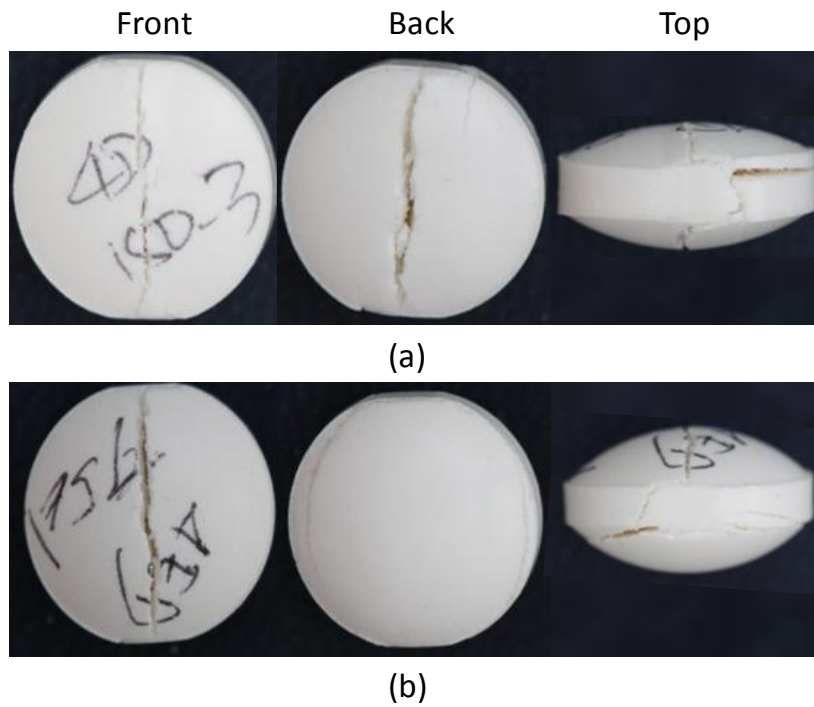


Figure 9-14 Photos of tablet breakage a) Compaction pressure: 150MPa, Mass: 400mg, geometry: $t/D=0.464$, $W/D=0.198$ and $D=10.347\text{mm}$ b) Compaction pressure: 75MPa, Mass: 400mg, geometry: $t/D=0.552$, $W/D=0.151$ and $D=10.387\text{mm}$

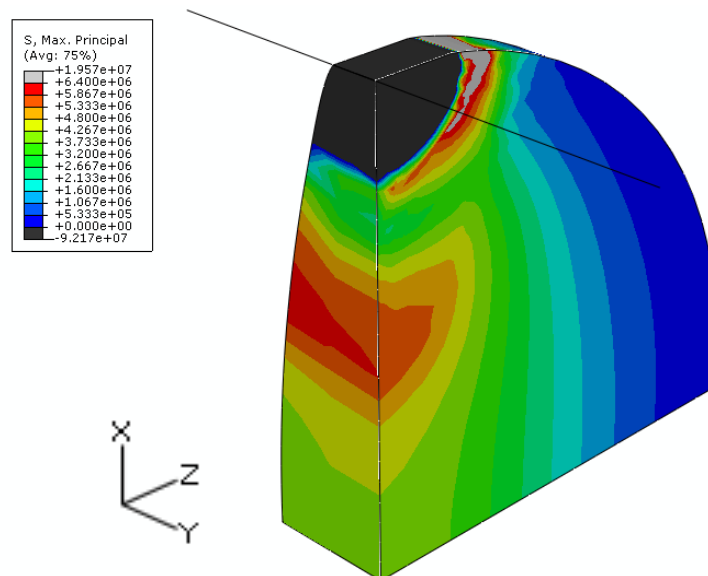


Figure 9-15 Maximum principal stress analysis of $t/D=0.451$, $W/D=0.1$ at $RD=0.84$ using DPC model

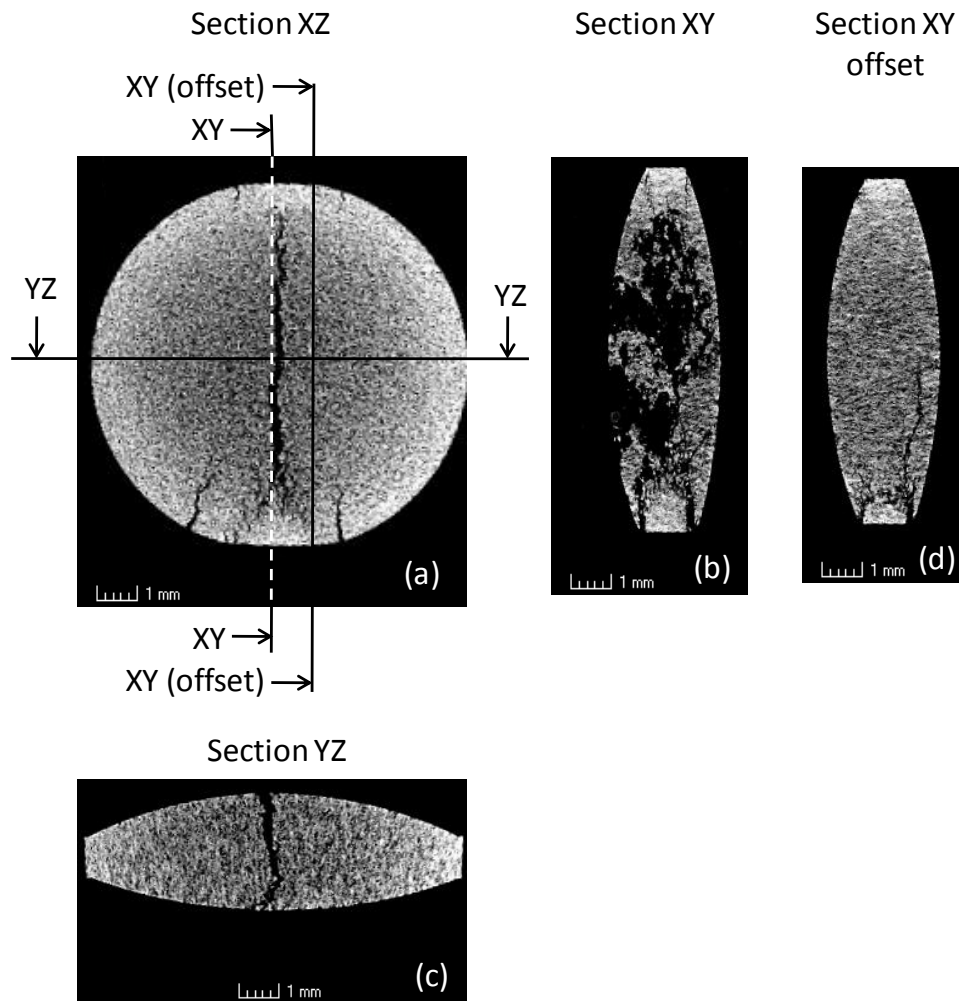


Figure 9-16 X-ray computed tomographic images of shallow shaped tablet ($t/D=0.3$, $W/D=0.1$, $D=10.322\text{mm}$) at different locations: a) X-Z plane; b) X-Y plane; c) Y-Z plane; d) offset plane (0.69mm from XY)

Figure 9-17 presents the breakage photos of ball shaped tablet and X-ray CT images of the failure patterns inside a ball shaped tablet. It can be seen that the tablet delaminates. The local flattening behaviour of the tablet near the loading area and the fracture plane can also be observed in Figure 9-17. This failure mode suggests that the breakage of this shape involves other mechanisms than those found in thin flat disks.

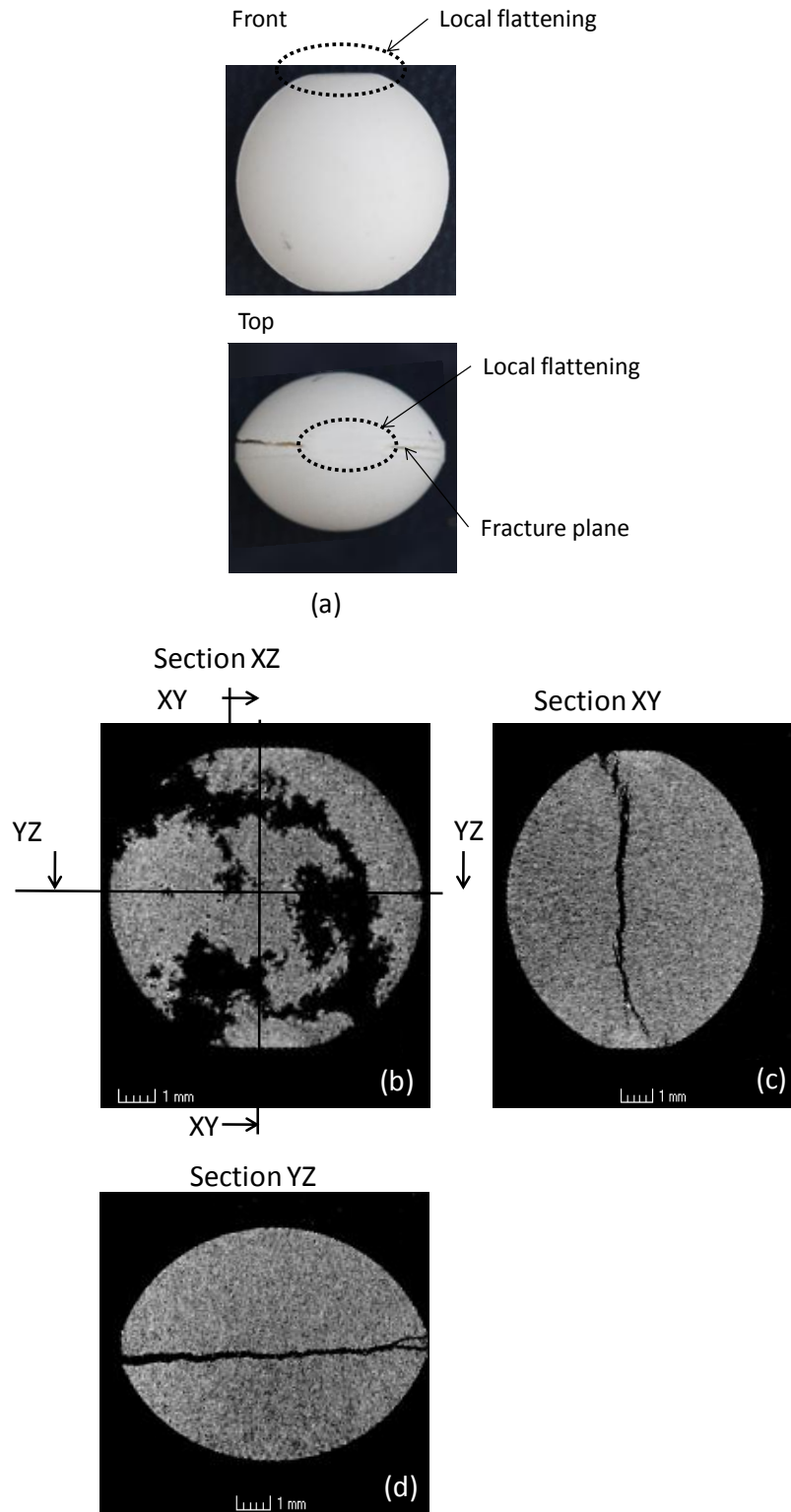


Figure 9-17 a) Photos of breakage of ball shaped tablet and X-ray computed tomographic images of ball shaped tablet ($t/D=0.721$, $W/D=0.0538$, $D=10.344\text{mm}$) at different locations: a) X-Z plane; b) X-Y plane; c) Y-Z plane

9.4 Conclusions

We identify a practical way to estimate the break force of curved faced tablets under diametrical compression loading using finite element analysis but without resorting to fracture mechanics. The analysis can be performed using commercial finite element software provided that the constitutive model of the material and the failure criterion are known.

Linear elastic constitutive models with maximum principal stress based criteria were found to over-predict the break force of tablets due to complex material behaviour around the concentrated loading points. Constitutive models that account for plastic flattening and possible densification around the loading points, such as the Drucker-Prager Cap model with density dependent material parameters are suitable to describe the behaviour of powder compacts. It was found that failure criteria based on a fully developed plastic zone are also over-predicting the break force while maximum principal stress based criteria at the onset of failure are in good agreement with experimental data.

For materials that exhibit brittle behaviour equation (8-6) can be calibrated using “numerical experiments” which can be used in their own right to relate the break force of curved faced tablets under diametrical compression to the tensile strength. This information can be used directly in pharmaceutical formulation design and process development. It is necessary, however, to consider the failure modes to define and restrict the applicability of the model obtained (e.g. for tablets with deep curvatures and tablets with small band thickness). Under these conditions the maximum principal

stress based criterion at the onset of failure gave consistent predictions with the failure modes observed experimentally.

Although validated for round tablets only, it is proposed that the numerical procedures identified above could be used to predict the break force of oval and elongated shaped tablets. Thus numerical analysis can replace empirical equations for more complex shapes.

Chapter 10. Conclusions and future work

10.1 Conclusions

Modelling die compaction requires identifying an accurate constitutive law for the power materials. Numerical models were used to analyse the density distribution in powder compacts, predict pressing forces and examine the effect of friction between powder and die wall. A practical method was developed to calibrate the constitutive model using a die instrumented with radial stress sensors. This apparatus also allows the measurement of the coefficient of friction between powder and die wall. The stress state in the powder compact during pressing is non-homogeneous due to the existence of friction. Thus, a calibration procedure taking friction into account was proposed. An accurate measurement of the stress-strain curve is required for model calibration; for this purpose a detailed analysis of the elastic compliance of the mechanical testing system was undertaken. Correction methods for system compliance were determined; these are important for compression and critical during the unloading stage when the elastic parameters are determined. For loading (compression) a correction method based on a nonlinear compliance curve was sufficient. For the unloading stage method using two load cells was necessary which considers the different stiffness of different parts of the system under different load conditions. Both correction methods were validated by comparing the compaction forces predicted by the fully calibrated model (with frictional input) (Chapter 6) with experimental results. It can be concluded that accurate simulations of powder compaction requires both an accurate constitutive model and an accurate measurement of the friction between powder and die wall. In the fully calibrated

model the material parameters are expressed as functions of relative density. The model is calibrated using practical methods based on uniaxial and diametrical compression tests and instrumented die compression tests. The possibilities and limitations offered by off-the-shelf finite element packages were investigated in terms of die compaction modelling capability. In such cases, a simplified material model (DPC model) can be used to simulating some key qualities of powder compaction (e.g. density distribution). However, the limitations of the simplified model were also identified. For example, the elastic properties (Young's modulus, E) of the material affect punch force prediction.

The breakage behaviour of round tablets with curved faces was studied experimentally (Chapter 8) and numerically (Chapter 9). A simplified equation which relates the break force of tablets under diametrical compression to the tensile strength of the material was proposed as an alternative to the only available empirical equation in the literature. By using this equation, the break force of curved faced tablets can be predicted for practical tablet geometries. The proposed equation reduces to the known analytical solution of Hertz for flat - faced disks.

Finite element analysis of diametrical compression test was carried out on flat and curve faced tablets. Different failure mechanism other than tensile failure was observed consistent with X-ray CT experiments of breakage patterns.

In order to predict the break force of tablets using straight forward finite element analysis three failure criteria were examined.

The failure criterion based on maximum principal stress was established and validated by experiments. The breakage force of different geometries of tablets could be accurately predicted by numerical analysis. The numerical indications were consistent with experimentally observed failure modes. Therefore, we established a suitable methodology to predict the break force of complex shaped tablets (e.g., oval and elongated shape) using relatively simple constitutive model and simple failure criteria.

10.2 Recommendations for Future work

Powder compaction is a complex process where the material transforms from loose powder into a dense compact. To date numerical modelling had been limited to density distribution and prediction of pressing forces and numerical predictions of important attributes such as integrity and breakage under various post-compaction loading configurations was not possible. This thesis has established a complete and rigorous methodology for calibrating constitutive models and initial steps towards predicting breakage behaviour. In order to fully release the potential of numerical analysis for practical powder pressing operations in a range of industrial sectors two important improvements are necessary

1. Simplify the constitutive model for compaction in order to capture large deformation and complex changes in the material in a more efficient manner.
2. Extend the models for compact behaviour by considering a fully anisotropic model whereby the yield surface depends on loading history expressed through more appropriate state variables than density considered in this thesis.

The above developments require long term effort. For immediate impact, however, the following recommendations are made for future work:

- Evaluate the suitability of the methodology to predict breakage forces for other types of powder compacts, particularly which do not exhibit brittle behaviour.
- Numerical simulation can be carried out to check the consistency of empirical equation for tablets at different densities.
- The effect of density distribution on failure mode (e.g. Figure 3-3) and potential crack formation for complex shape components (e.g. Figure 3-5) should be examined.

References

ABAQUS, 2007. ABAQUS 6.7.1 Theory manual. Simulia Inc.

Addinall E. and Hackett P., 1964. The tensile strengths of rock-like material. Civil Engineering Public Works Reviews. Vol. 59, pp. 1250-1253

Akazawa T., 1953. Tension test method for concrete. International Association of Testing and Research Laboratories for Materials and Structures. RILEM Bull. Vol. 13, pp. 13–23.

Akisanya A. R., Cocks A.C.F. and Fleck N.A., 1997. The yield behaviour of metal powders. International Journal of Mechanical Sciences. Vol. 39, iss. 12, pp. 1315-1324.

ASTM E111 - 04 Standard Test Method for Young's Modulus, Tangent Modulus, and Chord Modulus.

Awaji H. and Sato S., 1979. Diametral compressive testing method. Journal of Engineering Material Technology. Vol. 101, pp. 139-147.

Aydin I., Briscoe B. J. and Sanliturk K.Y., 1996. The internal form of compacted ceramic components: a comparison of a finite element modelling with experiment. Powder Technology. Vol. 89, pp. 239-254.

Bier W., Dariel M. P., Frage N., Hartmann S. and Michailov O., 2007. Die compaction of copper powder designed for material parameter identification. International Journal of Mechanical Sciences. Vol. 49, pp. 766-777.

References

Brewin P.R., Coube, O., Doremus, P. and Tweed J.H. (Eds.), 2008. Modelling of Powder Die Compaction. (Engineering Materials and Processes). Springer.

Briscoe B.J. and Rough S.L., 1998. The effect of wall friction on the ejection of pressed ceramic parts. Powder Technology. Vol. 99, pp. 228-233.

Carneiro F. and Barcellos A., 1953. Tensile strength of concrete. International Association of Testing and Research Laboratories for Materials and Structures. RILEM Bull. Vol. 13, pp. 99–125.

Cocks A.C.F. and Sinka I.C., 2007. Constitutive modelling of powder compaction - I. Theoretical concepts. Mechanics of Materials. Vol. 39, pp. 392-403.

Cocks, A.C.F., 2001. Constitutive modelling of powder compaction and sintering. Progress in Materials Science. Vol. 46, pp. 201-229.

Cocolas H.G. and Lordi N.G., 1993. Axial to radial pressure transmission of tablet excipients using a novel instrumented die. Drug Development and Industrial Pharmacy. Vol.19 (17-18), pp. 2473-97.

Coube O. and Riedel H., 2000. Numerical simulation of metal powder die compaction with special consideration of cracking. Powder Metallurgy. Vol. 43 (2), pp. 123-131.

Coube O., 1998. Modelling and numerical simulation of powder die compaction with consideration of Cracking. PhD thesis, University Pierre et Marie Curie, Paris.

Cundall P.A. and Strack O.D.L., 1979. A discrete numerical model for granular assemblies. Geo techniques. Vol. 29, pp. 47-65.

Cunningham J.C., 2004. Experimental studies and modelling of the roller compaction of pharmaceutical powders. PhD thesis, Drexel University, USA.

Cunningham J.C., Sinka I.C. and Zavaliangos A., 2004. Analysis of tablet compaction. Part 1 – Characterisation of mechanical behaviour of powder and powder/tooling friction. *Journal of Pharmaceutical Sciences*. Vol. 93, no. 8, pp. 2022-2039.

Davies P.N., Worthington, H.E.C., Podczek F. and Newton J.M., 2007. The determination of the mechanical strength of tablets of different shapes. *European Journal of Pharmaceutics and Biopharmaceutics*. Vol.67 (1), pp. 268-276.

Dean G.D., Loveday M.S., Cooper P.M., Read B.E., Roebock B. and Morrell R., 1995. Aspects of modulus measurement. Chapter 8 in: *Materials Metrology and Standards for Structural Performance*, Eds. Dyson, B.F., Loveday, M.S., and Gee, M.G. Chapman & Hall., pp. 150-209.

DiMaggio F. L. and Sandler I. S., 1971. Material models for granular soils. *ASCE Journal of Engineering Mechanics*. Vol. 97, pp. 935.

Djemai A. and Sinka I.C. 2006. NMR imaging of density distributions in tablets. *International Journal of Pharmaceutics*. Vol.319, pp. 55-62.

Doelker E and Massuelle D., 2004. Benefits of die-wall instrumentation for research and development in tableting. *European Journal of Pharmaceutics and Biopharmaceutics*. Vol. 58(2), pp. 427-44.

Doremus P., Geindreau C., Martin A., Debove L., Lecot, R. and Dao, M., 1995. High pressure triaxial cell for metal powder. *Powder Metallurgy*. Vol. 38, pp. 284-287.

Doremus P., Toussaint F. and Alvin O., 2001. Simple tests standard procedure for the characterisation of green compacted powder. Recent Developments in Computer Modelling of Powder Metallurgy Processes. NATO Advanced Research Workshop, Series III: Computer and Systems Science. Vol. 176, pp. 29-41.

Drucker D.C. and Prager W., 1952. Soil mechanics and plastic analysis or limit design. Quarterly Applied Mechanics. Vol. 10, pp. 157-165.

Durelli A.J., Riley W., 1965. Introduction to Photomechanics. New Jersey, Prentice-Hall.

Eiliazadeh B., Pitt K. and Briscoe B., 2004. Effects of punch geometry on powder movement during pharmaceutical tableting processes. International Journal of Solids and Structures. Vol. 41, pp. 5967– 5977.

Ernst E., Thummler F., Beiss P., Wahling R. and Arnhold V., 1991. Friction measurements during powder compaction, Powder Metallurgy International. Vol.23, no.2, pp. 77-84.

Fahad M.K., 1996. Stresses and failure in the diametral compression test. Journal of Materials Science. Vol. 31, pp. 3723-3729.

Fell J.T., and Newton J.M., 1970. Determination of tablet strength by the diametral-compression test. Journal of Pharmaceutical Sciences. Vol.59, pp. 688-691.

Fleck N.A., 1995. On the cold compaction of powders. Journal of the Mechanics and Physics of Solids. Vol. 43, no. 9, pp. 1409-1431.

Galen S., 2005. Path dependence and strength anisotropy of mechanical behaviour in cold-compacted powders. PhD thesis, Drexel University, USA.

References

Gethin D.T., Ariffin A.K., Tran D.V. and Lewis R.W., 1994. Compaction and ejection of green powder compacts. *Powder Metallurgy*. Vol.37, no.1, pp. 42-52.

Govindarajan R.M. and Aravas N., 1994. Deformation processing of metal powders: Part 1 - Cold isostatic pressing. *International Journal of Mechanical Sciences*. Vol. 36, pp. 343-357.

Green R.J., 1972. A plasticity theory for porous solids. *International Journal of Mechanical Sciences*. Vol. 14, pp. 215-224.

Gurson A.L., 1977. Continuum theory of ductile rupture by void nucleation and growth: part I, yield criteria and flow rules for porous ductile media. *Journal of Engineering Material and Technology*. Transactions of the ASME. Vol. 99, pp. 2–15.

Guyoncourt D.M.M., Tweed J.H., Gough A., Dawson J. and Pater L., 2001. Constitutive data and friction measurements of powders using instrumented-die. *Powder Metallurgy*. Vol. 44, pp. 25-33.

Han L.H., Elliott J.A., Bentham A.C., Mills A., Amidon G.E., Hancock B.C., 2008. A modified Drucker-Prager Cap model for die compaction simulation of pharmaceutical powders. *International Journal of Solids Structures*. Vol. 45, pp. 3088-3106.

Han, L.H., Laity P.R., Cameron R.E. and Elliott, J. A., 2011. Density and plastic strain evaluations using small-angle X-ray scattering and finite element simulations for powder compacts of complex shape. *Journal of Materials Science*. Vol. 46 (18), pp. 5977-5990.

References

- Hariran I and Newton J M, 1999. Tensile strength of circular flat and convex-faced Avicel PH102 tablets. *DARU Journal of Pharmaceutical Sciences*. Vol. 7, no. 3, pp. 36-40.
- Heckel R.W., 1961. An analysis of powder compaction phenomena. *Transaction of the Metallurgical Society of AIME*. Vol. 221, pp. 1001-1008.
- Hibbitt H.D., Marcal P.V. and Rice J.R., 1970. A finite element formulation for problems of large strain and large displacement. *International Journal of Solids Structure*. Vol. 6, pp. 1069-1086.
- Hibbitt, Karlsson & Sorensen, 1998. *ABAQUS Theory Manual Version 5.8*, Hibbitt, Karlsson & Sorensen, Inc., Pawtucket, RI.
- Hiestand, E.N., 2003. *Mechanics and physical principles for powders and compacts*. SSCI Inc., West Lafayette, USA.
- Hill R., 1950. *The mathematical theory of plasticity*. Oxford University Press, Oxford.
- Hondros G. 1959. The evaluation of Poisson's ratio and modulus of materials of a low tensile resistance by the Brazilian (indirect tensile) test with particular reference to concrete. *Australian Journal of Basic and Applied Sciences*. Vol. 10, pp. 243-268.
- Hong S.T., Hovanski Y., Lavender C.A. and Weil K.S., 2008. Investigation of die stress profiles during powder compaction using instrumented die. *Journal of Materials Engineering and Performance*. Vol. 17, pp.382–386.
- Hudson J.A., Brown E. T. and Rummel F., 1972. The controlled failure of rock discs and rings loaded in diametral compression. *International Journal of Rock Mechanics and Mining Sciences & Geomechanics Abstracts*. Vol.9 (2), pp.241--248.

References

Jaeger J.C. and Cook N.G.W., 1976. Fundamentals of rock mechanics. Chapman & Hall, UK, London, 2nd edition, ISBN 0-412-21410-5.

Jonsen P., Haggblad H. A. and Sommer K., 2007. Tensile strength and fracture energy of pressed metal powder by diametral compression test. Powder Technology. Vol. 176(2-3), pp. 148-155.

Kalidindi S., A. Abusafieh and E. El-Danaf, 1997. Accurate characterization of machine compliance for simple compression testing. Experimental Mechanics. Vol. 37, pp. 210-215.

Kergadallan J., Puente G., Doremus P. and Pavier, E., 1997. Compression of an axisymmetric part with an instrumented press, Proceeding International Workshop on Modelling of metal powder forming processes. Grenoble, France, 21-23 July, pp. 277-285.

Khoei A.R. and Azami A.R., 2005. A single cone-cap plasticity with an isotropic hardening rule for powder materials. International Journal of Mechanical Science. Vol. 47, pp. 94–109.

Khoei A.R. and Azizi S., 2004. Numerical simulation of 3D powder compaction processes using cone-cap plasticity theory. Materials and Design. Vol. 26, pp. 137–147.

Kim H.S., Oh S.T. and Lee J.S., 2002. Constitutive model for cold compaction of ceramic powder. Journal of the American Ceramic Society. Vol. 85, pp. 2137-2138.

References

Kim K.T., Suh, J. and Kwon Y.S., 1990. Plastic yield of cold isostatically pressed and sintered porous iron under tension and torsion. *Powder Metallurgy*. Vol. 33, pp. 321-326.

Koerner R.M., 1971. Triaxial compaction of metal powders. *Powder Metallurgy International*. Vol. 3, no. 4, pp.186-188.

Lee S. C. and Kim K.T., 2007. A study on the Cap model for metal and ceramic powder under cold compaction. *Materials Science and Engineering*. Vol. 445-446, pp. 163-169.

Li F., Pan J. and Sinka I.C., 2009. Contact laws between solid particles. *Journal of the Mechanics and Physics of Solids*. Vol. 57, pp. 1194-1208.

Macleod H.M. and Marshall K., 1977: The determination of density distributions in ceramic compacts using autoradiography. *Powder Technology*. Vol. 16, pp. 107-122.

Mates S. P., Rhorer R., Banovic S., Whitenton E. and Fields R., 2008. Tensile strength measurements of frangible bullets using the diametral compression test. *International Journal of Impact Engineering*. Vol. 35(6), pp. 511-520.

Mauricio B. and Sanchez H.S., 2008. Design of a die for the cold compaction calibration of powdered materials. *Latinoamericana de Metalurgia y Materiales*. Vol.1, pp. 223-234.

Michrafy A., Ringenbacher D. and Tchoreloff P. 2002. Modelling the compaction behaviour of powders: application to pharmaceutical powders. *Powder Technology*. Vol. 127, pp. 257– 266.

References

Neddermann, R.M., 1992. *Statics and Kinematics of Granular Materials*. Cambridge University Press. Cambridge.

Oliver, W. C. and Pharr G. M., 1992. Improved technique for determining hardness and elastic modulus using load and displacement sensing indentation experiments. *Journal of Materials Research*. Vol. 7.

Pavier E. and Doremus P., 1999. Triaxial characterisation of iron powder behaviour. *Powder Metallurgy*. Vol. 42, no. 4, pp. 345-352.

Pitt K.G., Heasley M.G., 2011. Determination of the tensile strength of elongated tablets. *Powder Technology*. Available online.

Pitt K.G., Newton J.M, Richardson R. and Stanley P. 1989b. The material strength of convex faced aspirin tablets. *Journal of Pharmacy and Pharmacology*. Volume 41, iss. 5, pp. 289–292.

Pitt K.G., Newton J.M. and Stanley P., 1991. Effects of compaction variables on porosity and material tensile strength of convex-faced aspirin tablets. *Journal of Pharmacy and Pharmacology*. Vol. 43(4), pp. 219-225.

Pitt K.G., Newton J.M., Stanley P.J., 1988. Tensile fracture of doubly-convex cylindrical discs under diametral loading. *Journal of Materials Science*. Vol. 23, pp. 2723-2728.

Pitt K.G., Newton J.M., Stanley P.J., 1989a. Stress distributions in doubly convex cylindrical disc under diametral loading. *Journal of Physics D: Applied Physics*. Vol. 22, pp. 1114-1127.

References

PM Modnet Computer Modelling Group, 1999. Comparison of computer models representing powder compaction process. *Powder Metallurgy*. Vol. 42, pp. 301-311.

PM Modnet Research Group, 2002. Numerical simulation of powder-compaction for two multilevel ferrous parts, including powder characterisation and experimental validation. *Powder Metallurgy*. Vol. 45, pp. 335-344.

Price H.L. and Murray K.H., 1973. Finite element analysis of the diametral test of polymer mouldings. *Journal of Engineering Material Technology*. Vol. 7, pp. 186–191

Procopio A.T., Zavaliangos A. and Cunningham J. C., 2003. Analysis of the diametrical compression test and the applicability to plastically deforming materials. *Journal of Materials Science*. Vol. 38, pp. 3629-3639.

Randall M.G., 1997. *Powder Metallurgy Science*, 2nd edition, MPIF, pp. 21-22.

Redanz P. and Fleck N.A., 2001. The compaction of a random distribution of metal cylinders by the discrete element method. *Acta Materialia*. Vol. 49, pp. 4325-4335.

Rudnick A., Hunter A. R. & Holden F. C., 1963. An analysis of the diametral compression test. *Material Research Standard*. Vol. 3, pp. 283-289.

Schneider L. and Cocks A.C.F, 2002. An experimental investigation of the yield behaviour of metal powder compacts. *Powder Metallurgy*. Vol. 45, no.3, pp.237-245.

Schneider L.C.R. and Cocks A.C.F., 2002. Experimental investigation of yield behaviour of metal powder compacts. *Powder Metallurgy*. Vol.45, no. 3, pp. 237-244.

Schneider L.C.R., 2003. *Compaction and yield behaviour of particulate materials*. PhD Thesis, University of Leicester, UK.

Schofield A. and Wroth C.P., 1968. *Critical State Soil Mechanics*, McGraw-Hill.

Shetty D.K., Rosenfield A.R. and Duckworth W.H., 1986. Mixed-mode fracture of ceramics in diametral compression. *Journal of the American Ceramic Society*. Vol. (6), pp. 437-443.

Shima S. and Oyane M., 1976. Plasticity theory for porous metals. *International Journal of Mechanical Sciences*. Vol. 18, pp. 285.

Shima, S. and Oyane, M., 1976. Plasticity theory for porous metals, *International Journal of Mechanical Sciences*. Vol. 18, pp. 285-291.

Simo J. C. and Hughes T. J. R., 1998. *Computational Inelasticity*, Springer.

Sinha T., Bharadwaj R., Curtis J.S, Hancock B.C and Wassgren C., 2010. Finite element analysis of pharmaceutical tablet compaction using a density dependent material plasticity model, *Powder Technology*, Vo. 202, iss. 1–3, pp. 46-54.

Sinha T., Curtis J.S., Hancock B.C., Wassgren C., 2010. A study on the sensitivity of Drucker–Prager Cap model parameters during the decompression phase of powder compaction simulations. *Powder Technology*. Vol. 198, pp. 315-324.

Sinka I.C. and Cocks A.C.F., 2007. Constitutive modelling of powder compaction-II. Evaluation of material data. *Mechanics of Materials*. Vol. 39, pp. 404-416.

Sinka I.C., 2007. Modelling powder compaction. *KONA (Hosokawa Powder Technology Foundation, Japan)*. Vol. 25, pp. 4-22.

References

Sinka I.C., Burch S.F., Tweed J.H. and Cunningham J.C., 2004b. Measurement of density variations in tablets using X-ray computed tomography. *International Journal of Pharmaceutics*. Vol.271, iss. 1-2, pp. 215-224.

Sinka I.C., Cunningham J.C. and Zavaliangos A., 2003. The effect of wall friction in the compaction of pharmaceutical tablets with curved faces: a validation study of the Drucker–Prager Cap model. *Powder Technology*. Vol. 133, pp. 33-43.

Sinka I.C., Cunningham J.C. and Zavaliangos A., 2004a. Analysis of tablet compaction. Part 2 – Finite element analysis of density distribution in convex tablets. *Journal of Pharmaceutical Sciences*. Vol. 93, no. 8, pp. 2040-2052.

Sinka, I.C., Cocks, A.C.F., Morrison, C.J. and Lightfoot, A., 2000. High Pressure triaxial facility for powder compaction. *Powder Metallurgy*. Vol. 43, no. 3, pp.253-262.

Sinka, I.C., Pitt K.G. and Cocks, A.C.F., 2007. Chapter 22: The strength of pharmaceutical tablets. In: *Particle Breakage. (Handbook of Powder Technology, Volume 12)* Eds. A.D. Salman, M.J. Hounslow and M. Ghadiri. Elsevier. ISBN-13: 978-0-444-53080-6. pp. 941-970.

Stanley P. and Newton J.M., 1977. Variability in the strength of powder compacts. *Journal of Powder Bulk Solution Technology*. Vol.1, pp. 13–19.

Stasiak M., Tomas J., Molenda M., Rusinek R. and Mueller P., 2010. Uniaxial compaction behaviour and elasticity of cohesive powders. *Powder Technology*. Vol. 203, pp. 482-488.

References

Thornton C. and Zhang L., 2003. Numerical simulations of the direct shear test.

Chemical Engineering & Technology. Vol. 26, pp. 153-156.

Timoshenko S.P. and Goodier J.N., 1970. Theory of elasticity. McGraw-hill, New York.

Trasorras J.R.L, Parameswaran R. and Cocks A.C.F, 1998. Mechanical behavior of metal powders and compaction modeling. ASM Handbook, Powder Metal Technologies and Applications. ASM International. Vol. 7, pp. 326-342.

Tsuji Y., Kawaguchi T. and Tanaka T., 1993. Discrete particle simulation of two-dimensional fluidized bed. Powder Technology. Vol. 77, pp. 79-87.

Turenne S., Godere C., Thomas Y. and Mongeon P.E, 1999. Evaluation of friction conditions in powder-compaction for admixed and die-wall lubrication. Powder Metallurgy. Vol. 42, pp. 263-268.

Tvergaard V., 1981. Influence of voids on shear band instabilities under plane strain condition. International Journal of Fracture Mechanics. Vol. 17, pp. 389-407.

United States Pharmacopoeia (USP, 2011)

Watson T.J. and Wert J.A. 1993. On the development of constitutive relations for metallic powders. Metallurgical Transactions A. Vol. 24A, pp. 2071-2081.

Wikman B., Solimannezhad H., Larsson R., Oldenburg M. and Haggblad H.A., 2000.

Wall friction coefficient estimation through modelling of powder die pressing Experiment. Powder Metallurgy. Vol. 43, pp. 132-138.

Wu B.L, 2005a. Compaction properties of sand-bentonite buffer materials in nuclear waste disposal concept. PhD Thesis, National Central University, Taiwan.

References

Wu C.-Y. and Cocks A.C.F., 2006. Numerical and experimental investigations of the flow of powder into a confined space. *Mechanics of Materials*. Vol. 38, iss. 4, pp. 304-324.

Wu C.-Y., Ruddy O.M., Bentham A.C., Hancock B.C., Best S.M. and Elliott J.A., 2005. Modelling the mechanical behaviour of pharmaceutical powders during compaction. *Powder Technology*. Vol. 152, pp. 107-117.

Wu C.-Y., Ruddy O.M., Bentham A.C., Hancock B.C., Best S.M. and Elliott J.A., 2008. Numerical and experimental investigation of the capping mechanisms during pharmaceutical tablet compaction. *Powder Technology*. Vol. 181, pp. 121-129.

Zavaliangos, A., 2002. Constitutive models for the simulation of P/M processes. *The International Journal of Powder Metallurgy*. Vol. 38 (2), pp. 27-39

Zienkiewicz O.C. and Taylor R.L., 1989. *The finite element method*, McGraw-Hill, London.

Appendices

Publications

Shang C., Sinka I.C. and Pan J., 2011. Material data for modelling density distributions in green parts. *Materials Science Forum*. Vol. 672. pp 207-214.

Shang C., Sinka I.C. and Pan J., 2011. Constitutive model calibration for powder compaction using instrumented die testing. *Experimental Mechanics*. pp. 1-14.

Shang C., Sinka I.C., Jayaraman B. and Pan J., 2012. Break force and tensile strength relationships for curved faced tablets subject to diametrical compression. *International Journal of Pharmaceutics*. To be appeared.

Shang C., Sinka I.C. and Pan J., 2012. Modelling of the break force of tablets under diametrical compression. *Journal of the Mechanics and Physics of Solids*. To be appeared.

Appendix A

Table A.1 Repeat data for diametrical compression test

Weight, g	Height, mm	Relative density	Break force, N	Tensile strength, MPa
1.391	2.986	0.675	68	1.31
1.366	2.934	0.675	61	1.20
1.398	2.982	0.679	69	1.33
1.366	2.922	0.677	65	1.30
1.375	2.976	0.670	63	1.23
1.398	2.739	0.737	144	3.04
1.418	2.778	0.738	144	3.01
1.400	2.743	0.738	148	3.12
1.396	2.729	0.739	136	2.88
1.387	2.708	0.740	136	2.91
1.412	2.598	0.784	244	5.43
1.415	2.600	0.785	246	5.48
1.419	2.610	0.785	229	5.08
1.396	2.584	0.779	236	5.28
1.392	2.557	0.785	223	5.05
1.436	2.423	0.853	431	10.28
1.432	2.409	0.855	421	10.11
1.414	2.385	0.853	431	10.45
1.400	2.353	0.856	427	10.50
1.444	2.423	0.857	442	10.56
1.443	2.294	0.903	651	16.40
1.459	2.343	0.894	687	16.95
1.418	2.249	0.894	656	16.76
1.453	2.331	0.895	652	16.18
1.408	2.238	0.903	658	17.00

Table A.2 Repeat data for uniaxial compression test

Weight, g	Height, mm	Relative density	Break force, N	Compressive strength, MPa
18.124	30.54	0.652	4659	37.72
18.103	30.46	0.653	4787	38.74
18.308	30.84	0.652	4999	40.45
18.330	30.86	0.653	4827	39.08
18.206	30.78	0.650	4840	39.17
19.698	30.78	0.703	8192	66.33
19.287	30.04	0.704	8106	65.57
18.571	28.80	0.707	8157	65.98
17.954	27.92	0.705	8208	66.38
18.404	28.60	0.706	8336	67.42
18.081	26.40	0.750	11869	95.95
18.250	26.78	0.747	11640	94.10
17.828	26.06	0.749	11860	95.81
18.078	26.50	0.747	11608	93.77
17.945	26.24	0.749	11823	95.53
18.029	24.42	0.807	17756	143.43
18.358	24.98	0.803	17061	137.74
18.546	25.16	0.805	17314	139.68
18.656	25.24	0.808	17393	140.40
18.800	25.40	0.809	17706	143.02
18.982	24.44	0.848	23943	193.22
19.236	25.10	0.837	20901	168.66
19.162	25.00	0.837	20854	168.39
19.290	25.24	0.835	20470	165.32
19.662	25.68	0.836	20812	168.03

Appendix B

Table B.1 Material parameters used in DPC model for MCC grade Avicel PH102 powder

Relative density	Young's Modulus, E (Pa)	Poisson's ratio	Cohesion, d	Internal friction angle, β	Cap shape parameter, R	Hardening rule, p_b
0.214	50453823	0.119	2.03E+04	70.30	0.400	1.00E+05
0.4	1.95E+08	0.132	3.73E+05	69.51	0.451	4.63E+06
0.5	4.12E+08	0.154	1.09E+06	69.07	0.496	1.00E+07
0.524	4.91E+08	0.161	1.36E+06	68.97	0.504	1.13E+07
0.548	5.82E+08	0.168	1.67E+06	68.87	0.524	1.30E+07
0.572	6.97E+08	0.176	2.05E+06	68.76	0.539	1.47E+07
0.596	8.27E+08	0.184	2.47E+06	68.65	0.560	1.64E+07
0.62	9.83E+08	0.193	2.97E+06	68.55	0.572	1.83E+07
0.644	1.18E+09	0.203	3.57E+06	68.44	0.588	2.07E+07
0.668	1.41E+09	0.213	4.25E+06	68.33	0.609	2.37E+07
0.692	1.68E+09	0.224	5.02E+06	68.22	0.629	2.69E+07
0.716	2.02E+09	0.235	5.91E+06	68.11	0.645	3.05E+07
0.74	2.39E+09	0.247	6.87E+06	68.00	0.663	3.47E+07
0.764	2.85E+09	0.259	7.98E+06	67.89	0.684	3.94E+07
0.788	3.42E+09	0.272	9.27E+06	67.77	0.708	4.49E+07
0.812	4.08E+09	0.286	1.07E+07	67.66	0.733	5.20E+07
0.836	4.86E+09	0.300	1.22E+07	67.54	0.758	5.97E+07
0.86	5.8E+09	0.314	1.40E+07	67.43	0.786	6.92E+07
0.884	6.92E+09	0.329	1.59E+07	67.31	0.818	8.02E+07
0.908	8.27E+09	0.345	1.81E+07	67.19	0.857	9.53E+07
0.932	9.8E+09	0.360	2.03E+07	67.08	0.905	1.15E+08
0.956	1.18E+10	0.377	2.30E+07	66.95	0.963	1.43E+08